Climatology of polar lows impacting Norway

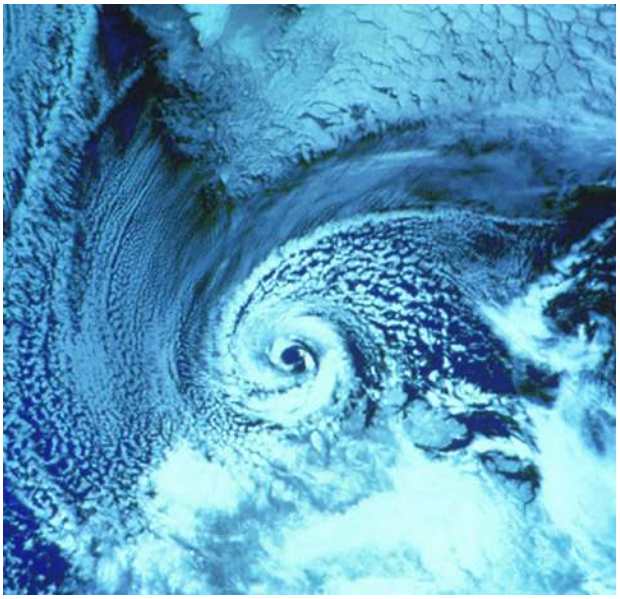

A master thesis in meteorology

Magnus Haukeland

June, 2016

UNIVERSITY OF BERGEN
GEOPHYSICAL INSTITUTE

Image on front page is taken from: J. Comisco. *Polar Oceans from Space*. Atmospheric and Oceanographic Sciences Library 41, Springer, 2010.

Abstract

Polar lows (PLs), mesoscale cyclones in high latitudes, impacting Norway are studied in this thesis. A climatology of PLs in the Nordic seas for the period 1979-2015 is made, by applying a cyclone detection and tracking algorithm to reanalysis data. Western Svalbard, northwestern Russia, Novaya Zemlya and the northern coast of Norway are found to be the areas with the most landfall of PLs. PLs are found to reach areas designated to fishery and oil platforms, the most affected fishery area being south of Svalbard. A higher number of PLs is found to reach Norway compared to previous climatologies, suggesting that other types of cyclones might be included by the algorithm. The temporal distribution of PLs making landfall in Norway shows a rather large annual variability, with December, January and February as the months with the most PL events. A sensitivity analysis shows that more PLs making landfall in Norway is found for a forward shear environment compared to a reversed shear environment, and that a negative phase of the Scandinavian blocking is the most favorable low-frequency atmospheric variability pattern for PLs making landfall in Norway. A climatology of PLs in the Nordic seas for future climate scenarios shows a reduction of PLs in the 21st century, more prominent for a larger anthropogenic climate forcing. The changes are however small compared to previous climatologies on PLs.

Acknowledgements

I would like to thank the dynmet group for great meetings and paper discussions throughout the year, giving me a better understanding of many concepts within the field of dynamical meteorology. I would also like to thank my supervisor, Thomas Spengler, for great ideas for my thesis, as well as vital feedback for my writing. I appreciated that he brought the whole dynmet group to Norwich, where we had a nice workshop in a new environment, as well as nice excursions, where I enjoyed the European Centre for Medium-Range Weather Forecasts the most. A special thanks goes to my co-supervisor Clio Michel, who remained patient in the start of my thesis project, when my programming skills were poor. She spent a lot of time correcting my thesis in the last stages of my writing process, which I am grateful for. I would also like to thank my dad, for checking the grammar of my thesis. I also have to thank the IT-department at UiB, who made me aware of the importance of making backups.

Contents

1 Introduction

This thesis will investigate the impact of polar lows (PLs) in the Nordic seas, focusing on the PLs reaching fisheries, oil platforms and the coast of Norway. A detection and tracking algorithm is utilized to make climatologies for the period 1979-2015 and for future climate scenarios. The results found in the climatology of future climate scenarios will be utilized to uncover the effect that global warming has on PL development. This thesis will also try to distinguish the environment most favorable for PL development by investigating the patterns of low-frequency atmospheric variability and the angle between the mean and thermal wind.

1.1 Polar lows

PLs are strong mesoscale cyclones, where mesoscale is referring to the scale of the PLs, which have a diameter in the order of 200-1000 km. A cyclone is a low-pressure area with counter-clockwise wind flow (in the Northern Hemisphere (NH)), due to the Coriolis force (Holton and Hakim, 2012). PLs are known for causing extreme weather, such as strong winds and precipitation, sometimes heavy snowfall, and generally have a lifespan of between 12 and 36 hours (Rasmussen and Turner, 2003). PLs are a seasonal phenomenon, mainly occurring in the period from September to April, with most events in the winter months.

PLs originate in cold air outbreaks (CAOs) (Rasmussen and Turner, 2003), where CAOs, as termed by Papritz et al. (2015), are "equatorward excursions of cold air masses across the sea ice boundary over the relatively warm, open ocean". CAOs predominantly occur in high latitudes, most often in winter when the temperature difference between polar regions and midlatitudes is at its peak (Papritz et al., 2015). CAOs produce a large temperature difference between the cold air and the warmer ocean, giving rise to heating of

the overlying air through heat transfer and evaporation of water, making the air statically unstable.

The static stability of an air parcel depends on the temperature structure of the atmosphere (Wallace and Hobbs, 2006). The atmosphere is considered to be dry statically unstable when the temperature decreases more rapidly than the dry adiabatic lapse rate, which is 10°C/km. In a statically unstable atmosphere, an air parcel that is perturbed from its initial position will tend to move further away from its initial position because of the fact that warmer air is less dense than cold air. Thus, in a CAO, where relatively warm air is situated close to the ocean surface, with colder air aloft, the rising of air, known in meteorology as convection, is initiated.

Convection is regarded as one of the main driving forces of PLs[1]. The convective nature of PLs can be supported by satellite observations, often showing deep cumulus convective clouds within PLs, and a spiral cloud structure which resembles the structure of a tropical cyclone (Montgomery and Farrell, 1992). This is illustrated in Fig. 1.1a, an Advanced Very High Resolution Radiometer (AVHRR) Infra Red (IR) image taken from the Sea Surface Temperature and Altimeter Synergy for Improved Forecasting of Polar Lows (STARS) database[2].

However, most recent scientific work on PLs, e.g. Montgomery and Farrell (1992) and Bracegirdle and Gray (2008), agree that convection is not the only forcing mechanism of PLs. Another important forcing mechanism is baroclinic instability (Bracegirdle and Gray, 2008) associated with a vertical shear in the mean flow, which is a change of wind speed with height, also known as thermal wind (Holton and Hakim, 2012). The vertical shear is induced by a horizontal temperature gradient, making the slopes of surfaces of constant pressure (isobars) increase with height, as pressure is a function of both density and temperature.

Horizontal temperature gradients, e.g. found at the edge of a CAO, lead to growth of baroclinic instabilities by converting potential energy into kinetic energy when reducing the tilt of potential temperature surfaces. The kinetic energy is released in the form of

[1] http://rammb.cira.colostate.edu/

[2] http://polarlow.met.no/STARS-DAT/

(a)

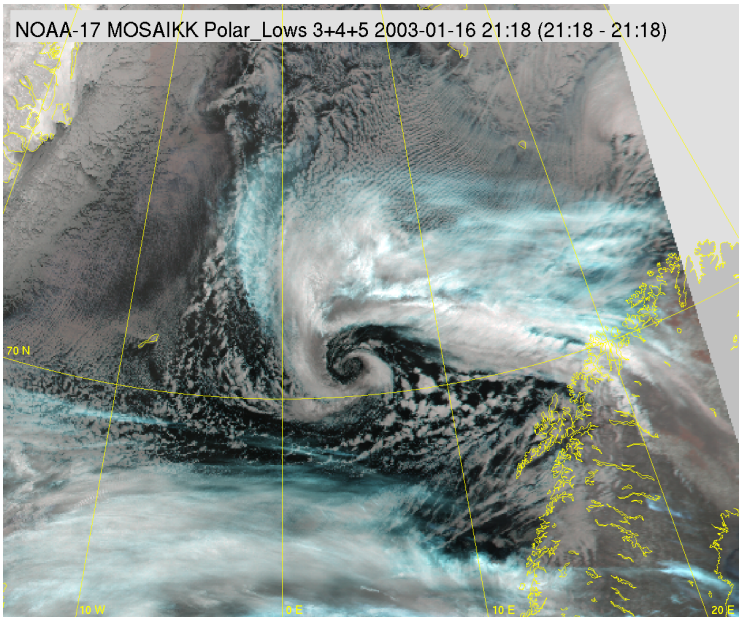

(b)

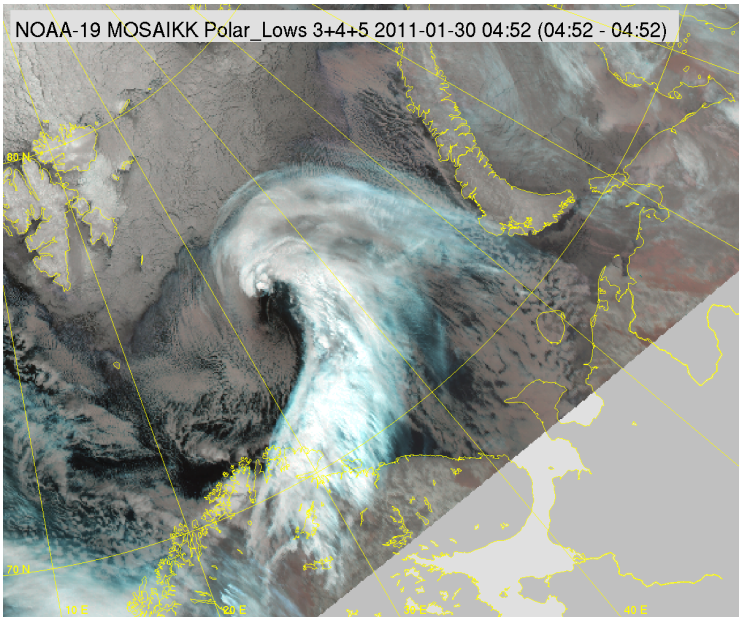

Figure 1.1: AVHRR IR images of a PL (a) with a spiral cloud signature outside the coast of Northern Norway and (b) a comma cloud PL in the Barents sea, north of Norway. Images taken from the STARS database.

vorticity, which is a measure of the local rotation of a fluid (Holton and Hakim, 2012). PLs with high baroclinicity are associated with a comma-shaped cloud (Yanase and Niino, 2007), shown in Fig. 1.1b.

1.2 Environments affecting polar low development

A suitable environment is vital for PLs to develop. PL development can be affected by the environmental angle between the mean and thermal wind (Terpstra et al., 2016), explained in section 1.2.1. Patterns of low-frequency atmospheric variability such as the North Atlantic Oscillation (NAO) and the Scandinavian blocking (SB), explained in section 1.2.2, can also have an effect on PL development (Claud et al., 2007).

1.2.1 Forward and reverse shear conditions

PLs can be subdivided into groups related to the angle between the mean and thermal wind at the genesis time. Climatologies of PLs, such as Terpstra et al. (2016) and Kolstad (2006), distinguish between two environments in which PLs develop; forward shear (FS) and reverse shear (RS) environments. A PL is generated in a FS environment if the thermal wind is parallel with the mean wind (angle between 0° and 45°), whereas a PL is generated in a RS environment if the thermal wind is antiparallel with the mean wind (angle between 135° and 180°) (Kolstad, 2006), illustrated in Fig. 1.2. This means that for a FS (RS) environment, the warm air lies to the right (left) of the mean flow and the mean wind increases (decreases) with height, inducing cold air advection (warm air

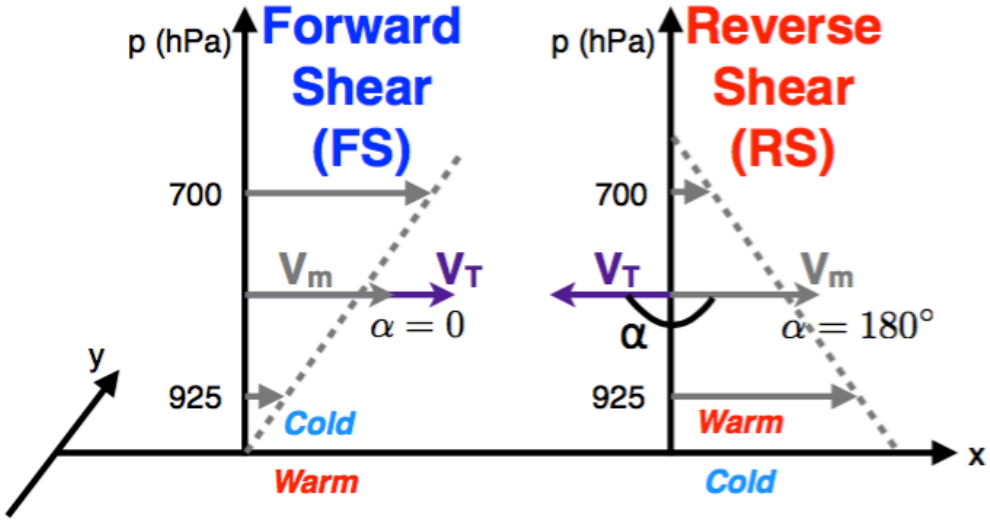

Figure 1.2: (left) FS environment, the thermal wind (V_T) is parallel with the mean wind (V_m), and (right) RS environment, the thermal wind is antiparallel with the mean wind. The vertical wind shear is induced by a horizontal temperature gradient. The thermal wind has warm air on its right hand side. Figure made by Clio Michel.

advection), meaning that cold (warm) air moves into a warmer (cooler) region (Wallace and Hobbs, 2006), behind the polar low and warm air advection (cold air advection) in front of the polar low (Kolstad, 2006). Both cases induce a direct thermal circulation, converting available potential energy into kinetic energy.

1.2.2 North Atlantic Oscillation and Scandinavian blocking

The NAO is a low-frequency atmospheric variability pattern between the Icelandic low and the Azores high, where the positive phase (NAO+) is associated with a strong subtropical high pressure system over the Azores Islands and a strong low pressure system over Iceland, whereas the negative phase (NAO-) is associated with a lower than normal pressure over the Azores Islands and a higher than normal pressure over Iceland (Walker and Bliss, 1932). Climatological composites of 500-hPa geopotential height and 10-m winds for NAO+ and NAO- (Fig. 1.3) show strong low-level winds in the Atlantic and a low geopotential height northwest of Greenland during NAO+ conditions and an anticyclonic low-level circulation centered over Greenland during NAO- conditions.

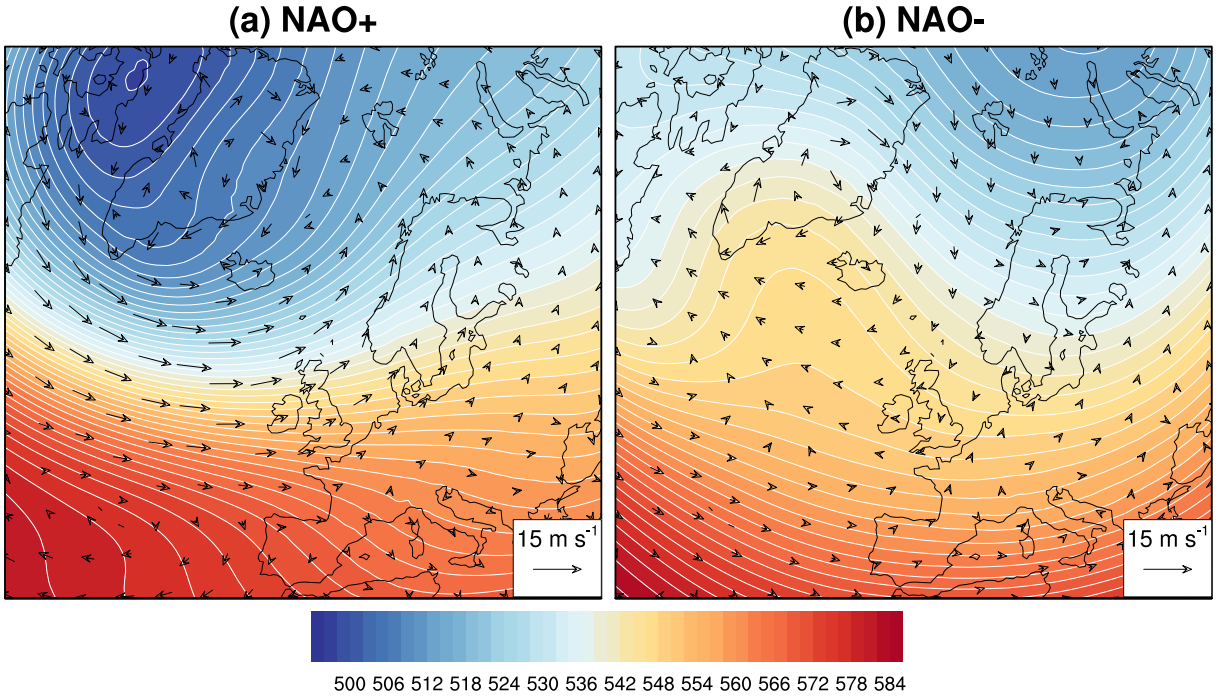

Figure 1.3: Composites of 500-hPa geopotential height (countours and shading, units: dam) and 10-m winds (arrows, units: m s^{-1}) during days of (a) NAO+ and (b) NAO-.

SB is a reversal of the meridional gradient of the geopotential height, centered over Northern Europe. The positive phase (SB+) is associated with positive geopotential height anomalies, often reflected by blocking anticyclones over Scandinavia, leading to the redirecting of cyclones toward Southern Europe or areas north of Scandinavia (Claud et al., 2007) (Fig. 1.4a). The negative phase (SB-) is associated with negative geopotential height anomalies over Scandinavia, which confine the cyclones south over Europe (Fig. 1.4b).

Overall, the negative phases of NAO and SB have a northerly surface flow over the Norwegian sea suggesting more frequent CAOs and thus providing more favorable conditions for PL genesis.

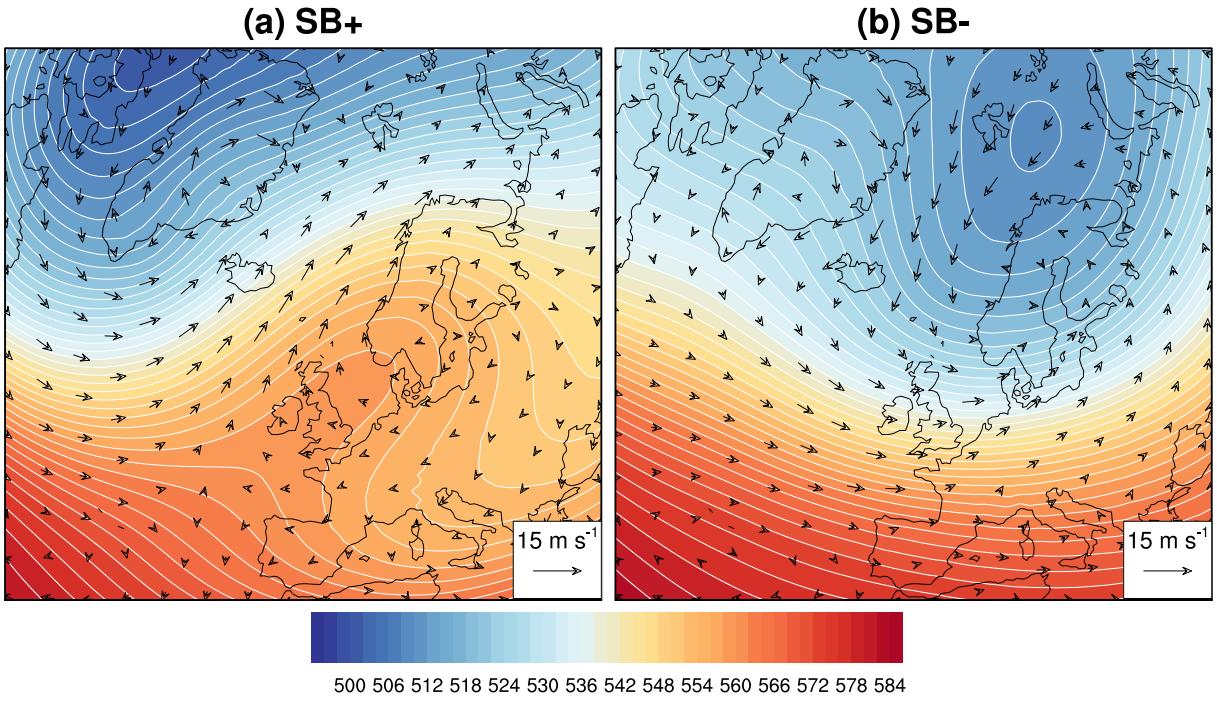

Figure 1.4: Composites of 500-hPa geopotential height (countours and shading, units: dam) and 10-m winds (arrows, units: m s^{-1}) during days of (a) SB+ and (b) SB-.

1.3 Motivation

PLs have throughout history had a vast effect on coastal environments in high latitudes, e.g. Scandinavia[3]. One of the most severe cases was the storm that hit the small village of

[3] http://polarlow.met.no/polar_lows/hamningberg/

Hamningberg in Finmark, the northernmost part of Norway, in 1894. The main industry in Hamningberg was fishing, and there were no islands to protect the village from rough weather coming from the Barents Sea. During the night between 19th and 20th of May 1894 when the whole fishing fleet was at sea, a horrible storm hit. Luckily, all 36 fishermen were rescued from the sea and brought to safety.

When investigating the weather conditions prior to the storm, a rapid change was found. Fig. 1.5 shows the temperature and precipitation measurements from Vardø, May 1894, showing a temperature drop from almost 9°C to 0°C from 15th to 16th of May, which could be due to a CAO. Furthermore, a precipitation value of more than 20 mm was measured on the 20th May, which is a very high value for this area.

NCEP reanalyses charts[4], based on pressure sensors from 1894, were also investigated (Fig. 1.6). It is evident from Fig. 1.6a, showing the 850-hPa temperature on May 19th, that a large area of cold air was situated north and west of Norway. The CAO is less apparent on the next day (Fig. 1.6b). Fig. 1.6c shows the 500-hPa geopotential height and mean sea

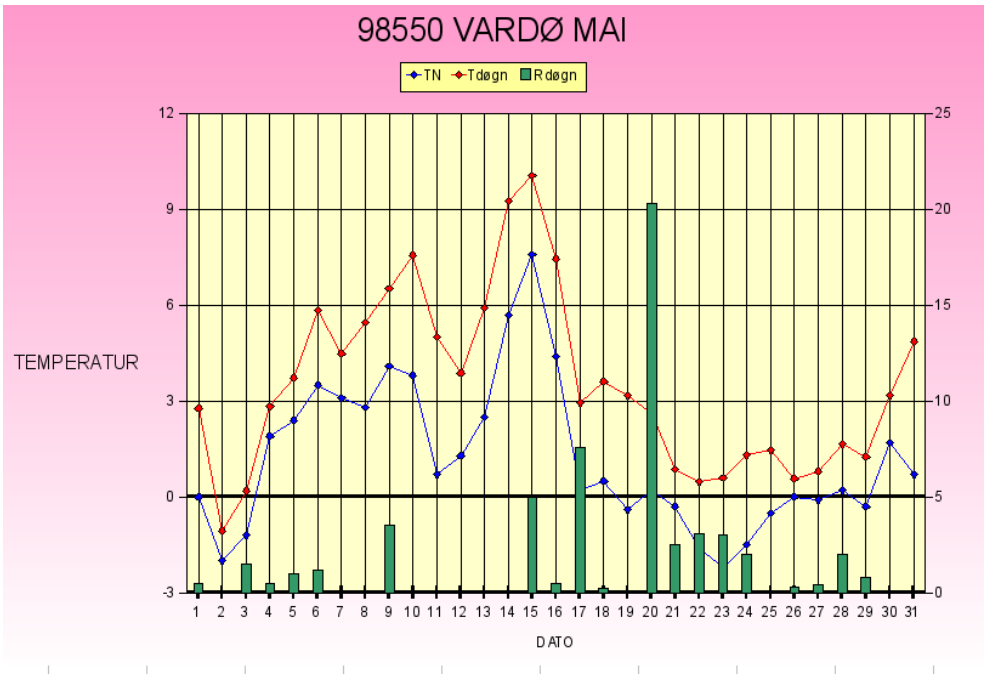

Figure 1.5: Average and minimum temperature profiles (line graphs, units: °C), in red and blue, respectively, and the accumulated daily precipitation (histogram, units: mm) in green, for Vardø, May 1984. Figure taken from `http://polarlow.met.no/polar_lows/hamningberg/`.

[4] `http://www.wetterzentrale.de/topkarten/fsreaeur.html`

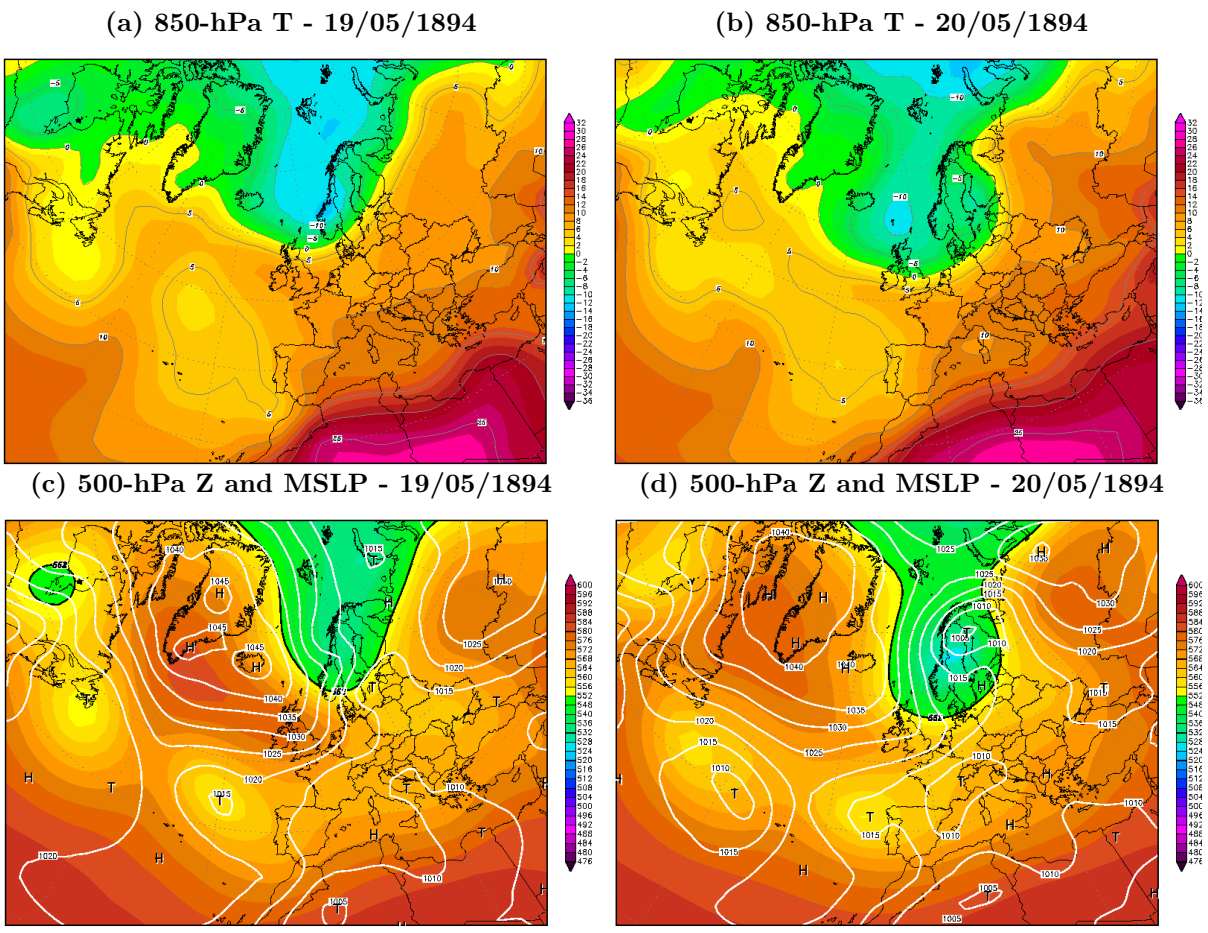

Figure 1.6: NCEP reanalysis of 850-hPa temperature (contours and shading, units: °C) on (a) 19th of May and (b) 20th of May, and 500-hPa geopotential height (shading, unit: dam) and MSLP (contours, unit: hPa) on (c) 19th of May and (d) 20th of May 1894. Figure taken from `http://www.wetterzentrale.de/topkarten/fsreaeur.html`

level pressure (MSLP) contours on May 19th, where a high pressure system located over Greenland and a low pressure system around Novaya Zemlya suggests a northerly low-level wind flow in the Barents Sea. Isobars are situated close to each other at the northern coast of Norway both on May 19th and May 20th (Fig. 1.6c and d), indicating strong winds in the area.

The arguments found above indicates that a CAO region developed in the Barents Sea. Furthermore, strong northerly winds and high precipitation values were present, supporting the conclusion that the event in Hamningberg in 1894 indeed is one of the oldest cases one with some certainty can describe as a PL.

1.4 Outline

An event like the one in Hamningberg emphasizes why it is important to understand PLs, and where they make landfall. This thesis will study the PLs that reach the coast of Norway, as well as PLs that reach locations designated to fishery or oil platforms. Climate runs will be utilized to investigate how the frequency and occurrence of PLs will change due to global warming.

Some interesting questions come to mind when studying these PLs: When and where do they hit? Are there favorable locations? Which synoptic conditions are favorable for PL development? Is there any difference in the conditions for the ones that hit the coast of Norway and the ones that do not? Do the NAO or the SB have an impact? Are there more FS or RS PLs making landfall in Norway? Will there be more or less PLs reaching the Norwegian coast, fisheries and oil platforms in the future? This thesis will try to answer these questions.

Chapter 2 introduces the data and methods utilized in this thesis. Chapter 3 contains the results obtained for the climatology of polar lows in the Nordic seas for the period 1979-2015. Chapter 4 contains the results for the climatology of polar lows in the Nordic seas for future climate scenarios, investigating the effect of global warming on the PL distribution. The summary and conclusions are presented in chapter 5.

2 Data and methods

This chapter introduces the data and methods utilized in this thesis. Section 2.1 describes the data from the ERA-Interim (ERAI) reanalyses and the Geophysical Fluid Dynamics Laboratory (GFDL) High Resolution Atmospheric Models (HiRAM). The procedure of utilizing the Melbourne detection and tracking algorithm to create PL tracks is described in section 2.2. Section 2.3 explains the making of density plots. Section 2.4 deals with the method of FS and RS distinction. Section 2.5 describes the indices of NAO and SB, as well as statistical methods needed when investigating the NAO and SB indices effect on PLs.

2.1 Data

2.1.1 ERA-Interim

One of the datasets utilized in this thesis is the ERA-Interim (ERAI) reanalysis provided by the European Centre for Medium range Weather Forecasts. ERAI is a global atmospheric assimilation system from 1st of January 1979, and still ongoing, which incorporates observations both from instruments and satellites with the purpose of representing the past atmospheric and oceanic state (Dee et al., 2011). ERAI features a horizontal longitude/latitude resolution of $0.75°\times0.75°$, but is downloaded at a resolution of $0.5°\times0.5°$. ERAI has 60 vertical levels from the surface to 0.1-hPa[1].

ERAI utilizes the Integrated Forecasting System, which is a hydrostatic, semi-Lagrangian model making use of the 4D-var data assimilation scheme, which continuously assimilates observations into the model to form a physically realistic analysis[2]. Parameterization

[1] http://www.ecmwf.int/sites/default/files/elibrary/2011/8174-era-interim-archive-version-20.pdf

[2] http://www.ecmwf.int/en/forecasts/documentation-and-support/changes-ecmwf-model/ifs-documentation/

schemes are utilized for the physical mechanisms at smaller scales than the resolved scale of the model grid, including radiative transfer, turbulent mixing, convection, clouds, precipitation, surface exchange, orographic drag, and non-orographic gravity wave drag. The analysis provides access to variables such as pressure, wind components, temperature, geopotential height etc. at different heights, every 6 hours.

2.1.2 GFDL

Various runs of the GFDL HiRAM climate models are utilized in this thesis to investigate the change in PL track density due to global warming. The GFDL HiRAM models are uncoupled atmospheric models using different boundary conditions, such as sea surface temperature (SST) and sea ice, from two different models: The Earth System Model version 2M (ESM2M) and the Coupled Model version 3 (CM3).

Both ESM2M and CM3 are global, coupled models consisting of an atmospheric component, a land component and an oceanic component, representing the global climate and trying to capture anthropogenic climate forcing. CM3 is a physical model focusing on aerosol-cloud interactions[3], whereas ESM2M is an earth system model which simulates the carbon-cycle e.g. through precipitation, evaporation, rivers, streams, and runoff components[4]. The 2M in ESM2M refers to the pressure-based vertical coordinates utilized in the model, based on the GFDL's Modular Ocean Model version 4.1. Both models include SST and sea ice dynamics.

HiRAM is run with two different resolutions, referred to as HiRAM c180 and HiRAM c360, where HiRAM c180 has a horizontal longitude/latitude resolution of $0.625° \times 0.50°$, and HiRAM c360 has a horizontal resolution of $0.3125° \times 0.25°$. HiRAM c180 contains three control runs for the historical period of 1979-2009, and future runs for the periods 2026-2035 and 2086-2095. The period 2026-2035 contains three runs with boundary conditions provided by CM3 and three runs with boundary conditions provided by ESM2M, using the climate scenario called Representative Concentration Pathway (RCP) 4.5, which has a peak of climate forcing around 2060[5] (Fig. 2.1). The period 2086-2095 also contains three runs with boundary conditions provided by both CM3 and ESM2M, but with both RCP4.5

[3] http://www.gfdl.noaa.gov/news-app/story.32

[4] http://www.gfdl.noaa.gov/earth-system-model

[5] http://sedac.ipcc-data.org/ddc/ar5_scenario_process/RCPs.html

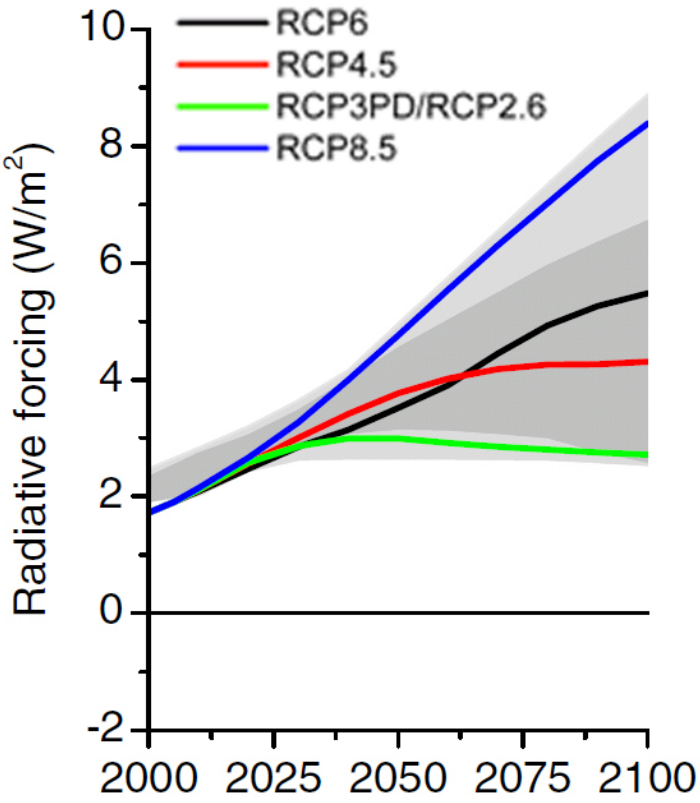

Figure 2.1: Radiative forcing of the different RCPs for the 21st century, with RCP4.5 in red and RCP8.5 in blue. Figure taken from `http://sedac.ipcc-data.org/ddc/ar5_scenario_process/RCPs.html`.

and RCP8.5. The radiative forcing in RCP8.5 rises linearly throughout the 21st century (Fig. 2.1), which will be the case if no action is made to prevent anthropogenic global warming. HiRAM c360 only contains two control runs for the historical period 1979-2009, RCP4.5 is only utilized for the period 2026-2035, and RCP8.5 is only utilized for the period 2086-2095.

2.2 Utilizing the Melbourne cyclone detection and tracking algorithm

2.2.1 Cyclone detection

The climatologies deduced in this thesis are based on the Melbourne cyclone detection and tracking algorithm created by Simmonds and Murray (1991). For the climatology of PLs in the period 1979-2015, the algorithm was applied to ERAI data, whereas for the clima-

tology of PLs for future climates, the algorithm was applied to GFDL data, both being in a longitude-latitude format. The data is interpolated to a polar stereographic array centered on the considered pole, which in this case is the North pole. The stereographic projection means that a sphere is projected onto a plane (Warner, 2011).

The first step in the algorithm is to detect cyclone centers by modeling the MSLP field between grid points analytically, by fitting a bicubic spline function to the entire field. The MSLP is interpolated by using a Taylor expansion:

$$p(x_{\mathrm{i}} + \delta x, y_{\mathrm{j}} + \delta y) = \sum_{m=0}^{3} \sum_{n=0}^{3} p_{x^m y^n}(x_{\mathrm{i}}, y_{\mathrm{j}}) \delta x^m \delta y^m \ , \tag{2.1}$$

where

$$p_{x^m y^n} = \frac{\partial p^{m+n}}{\partial x^m \partial y^n} \ . \tag{2.2}$$

The algorithm searches for possible cyclones by comparing the values of MSLP of neighboring grid points. However, some shallow depressions may not be caught by this method, therefore a less restricted method is implemented, searching for grid points where the Laplacian of the MSLP field,

$$\nabla^2 p(x_{\mathrm{i}}, y_{\mathrm{i}}) = p_{\mathrm{xx}} + p_{\mathrm{yy}} \ , \tag{2.3}$$

has to be larger than all surrounding grid points and larger than a prescribed positive value. The exact position of the cyclone is found by an iterative minimization process of the MSLP, by using the first and second derivatives at one point to define an ellipsoid, which will become the centre in the next iteration. This ellipsoid is illustrated in Fig. 2.2, where the orientation of the axes, θ, is given by

$$\tan 2\theta = \frac{2p_{\mathrm{xy}}}{p_{\mathrm{xx}} - p_{\mathrm{yy}}} \ , \tag{2.4}$$

and the second derivatives in the axial directions by

$$p_{\mathrm{uu}} = \frac{p_{\mathrm{xx}} + p_{\mathrm{yy}}}{2} - \sqrt{\left(\frac{p_{\mathrm{xx}} + p_{\mathrm{yy}}}{2}\right)^2 + {p_{\mathrm{xy}}}^2} \ , \tag{2.5}$$

where u and v are the major and minor axes of the ellipsoid, respectively.

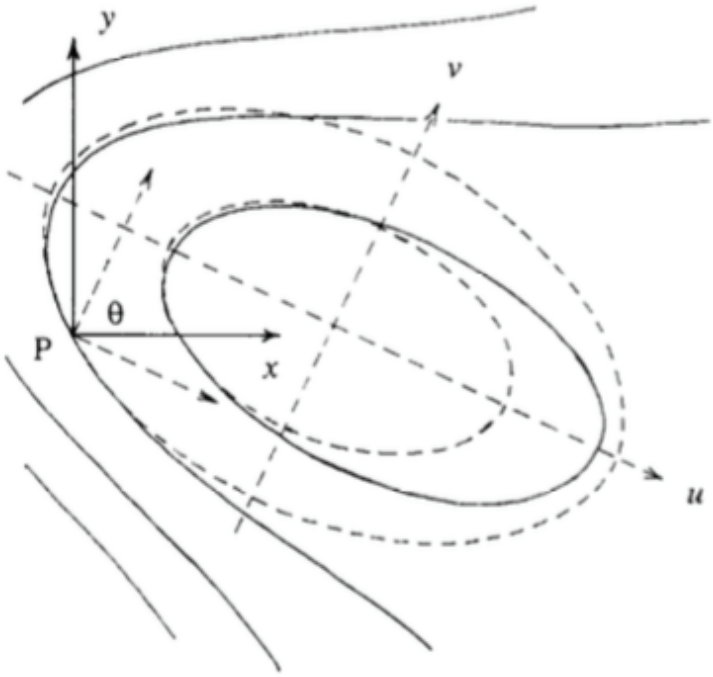

Figure 2.2: An example of a pressure pattern (solid lines) and the contours and axes (u and v) of the ellipsoid of best fit (broken lines) defined by the derivatives at point P. Figure taken from Simmonds and Murray (1991).

The algorithm searches for true pressure minima, that are points where $p_{\mathrm{uu}} > 0$ and $p_{\mathrm{u}} = p_{\mathrm{x}} = 0$. These points can be both open or closed depressions, where open depressions refer to regions with open isobars, and closed depressions refer to regions with closed isobars. If a closed depression is not found when looking for a minimum in the MSLP field and a large value for the Laplacian, the algorithm searches for an open depression by minimizing the magnitude of the pressure gradient, illustrated in Fig. 2.3. An inflection point, a point in which the pressure gradient has a minimum, which is very often associated with a concavity in the pressure field, indicates the most likely position of a closed depression below the resolution limit.

2.2.2 Cyclone tracking

The second part of the detection and tracking algorithm builds tracks using the positions and pressures found in the detection part. The tracking part of the algorithm looks at the detected cyclones at two consecutive time steps. Let us call the cyclones detected at time t with the letter G, and cyclones detected at time $t + \delta t$ with the letter C. The algorithm estimates the position $\mathbf{r}$ of the cyclone G at time $t + \delta t$ by using a weighted average w_{M}

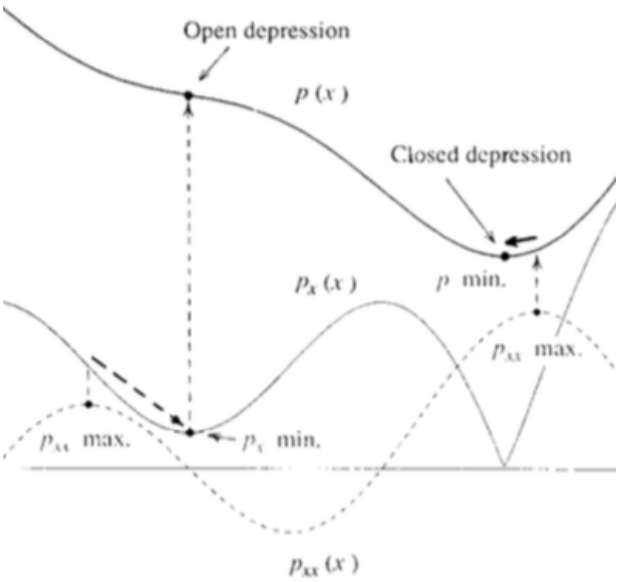

Figure 2.3: Cross-section of MSLP p, the first derivative p_{x}, the second derivative p_{xx} and the positions of an open and a closed depression. Figure taken from Simmonds and Murray (1991).

based on its displacement in the previous time step ($\mathbf{r}(t) - \mathbf{r}(t - \delta t)$) and the climatological cyclone velocity $\mathbf{v}_{\mathrm{av}}(\varphi)$, for the latitude φ:

$$\mathbf{r}_{\mathrm{est}}(t + \delta t) = \mathbf{r}(t) + w_{\mathrm{M}} \left(\mathbf{r}(t) - \mathbf{t}(t - \delta t)\right) + (1 - w_{\mathrm{M}})\mathbf{v}_{\mathrm{av}} \left(\varphi(t)\right) \delta t + \mathbf{r}_{\mathrm{K}} \ , \tag{2.6}$$

where $\mathbf{r}_{\mathrm{k}}$ is a small magnitude term included to replicate the acceleration of climatological cyclone velocities. A schematic of the estimated position is found in Fig. 2.4. The pressure at the centre of the cyclone is calculated based on a weighting of persistence and its previous tendency:

$$p_{\mathrm{est}}(t + \delta t) = p(t) + w_{\mathrm{P}} \left(p(t) - p(t - \delta t)\right) \ . \tag{2.7}$$

Through testing of the scheme, weighting values of $w_{\mathrm{M}} = 1$ and $w_{\mathrm{P}} = 0.8$ were found suitable.

Next, the C cyclones and G cyclones positions are compared to each other. The algorithm searches in a radius r_{c} around cyclone G for a cyclone C, where r_{c} was chosen to be 6 degrees of latitude. Fig. 2.5 illustrates an example of this scenario. Cyclones G1 and G2 both have three C cyclones within their radius. Since cyclone C5 is located in the discs around cyclones G1 and G2, these cyclones form a group. Cyclone G3 has no C cyclones in its radius, meaning that it is the end of a track or a cyclone detected only at one time

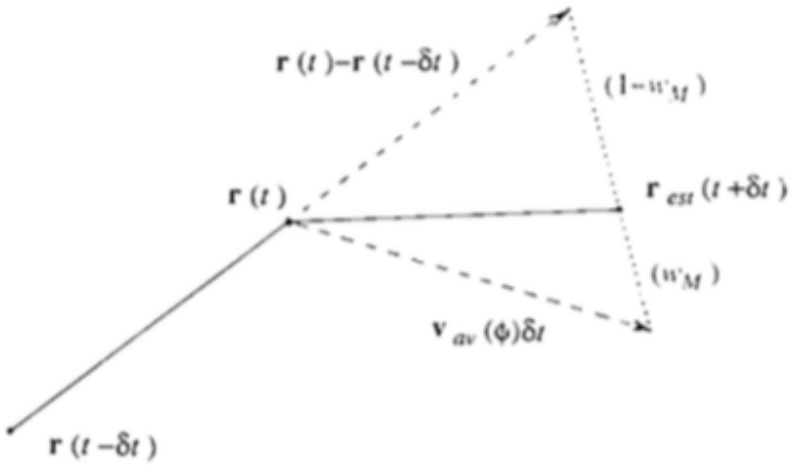

Figure 2.4: Schematic of the estimated position ($\mathbf{r}_{\text{est}}(t+\delta t)$) of a G cyclone based on weighting w_{M} of the previous displacement ($\mathbf{r}(t)-\mathbf{t}(t-\delta t)$), and weighting $1-w_{\text{M}}$ of the climatological cyclone velocity $\mathbf{v}_{\text{av}}(\varphi)$. Figure taken from Simmonds and Murray (1991).

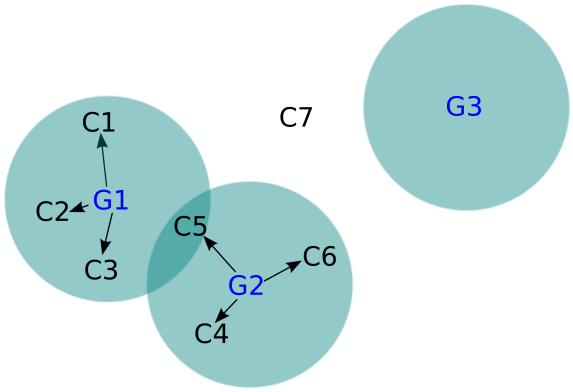

Figure 2.5: Cyclones G at time t, and cyclones C at time $t+\delta t$. The circles are a representation of the radius of 6 degrees of latitude around the G cyclones. Figure taken from Michel and Keay (2014).

step. Cyclone C7 does not lie within the radius of a G cyclone, meaning that it is a start of a new track in the next time step (Michel and Keay, 2014).

In the final stage of the tracking, it has to be decided which C cyclone within the radius of a G cyclone is to be kept. A probability is assigned to each pair of G and C cyclones based on their separation and pressure differences, by including a component of

pressure differential in the radius:

$$r' = \sqrt{r^2 + \left(\frac{\delta p}{k_{\mathrm{rp}}}\right)} \,, \tag{2.8}$$

where k_{rp} is a constant, chosen to be 1.4 hPa/°latitude. Then the most probable combination of G and C cyclones is calculated by:

$$P = P_{\mathrm{max}} - \frac{r'^2}{{r_{\mathrm{c}}}^2} \,, \tag{2.9}$$

where $P_{\mathrm{max}} = P_{\mathrm{new}} P_{\mathrm{open}}$ depends on the age and the strength of the cyclone, and is included to suppress the inclusion of weaker cyclones. $\mathrm{P_{new}}$ has the value 0.6 for a newly detected cyclone and 1 for a cyclone that is in its second or later time step. P_{open} has the value 1 for a strong, closed cyclone, 0.6 for a strong, open cyclone, and 0.6 for a weak cyclone, open or closed. Whether the cyclones are characterized as strong or weak depends on their depth, their maximum of Laplacian of the MSLP, their third derivative at the inflection point and their averaged Laplacian of the MSLP around the maximum location (Michel and Keay, 2014).

After the probability is calculated, the combination with the highest probability is kept. This is illustrated in Fig. 2.6, where combination G1C1 is kept, since it has a higher probability than the combination G1C2. The entire tracking process is repeated for each time step, and this way tracks of cyclones are built.

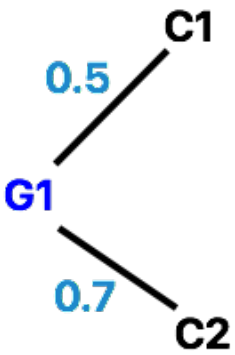

Figure 2.6: Cyclones G1, C1 and C2, and their associated probabilities.

2.2.3 Cyclone selection criteria

When the detection and tracking has been completed by the algorithm, a list of cyclone tracks is made. The next step is to select the ones that resemble PLs. A selection program is utilized to keep tracks that meet various criteria, in order to be assimilated as PLs.

A condition that the length of the track has to be 4 time steps or more has to be met. One time step in ERAI data is 6 hours, meaning that the cyclones lifetime needs to be at least 18 hours. Next, both the first point of the track (genesis point) and the last point of the track (lysis point) need to be in the Nordic seas, which in the selection program is defined as 20°W-60°E / 60°N-85°N. The genesis point must be located in a grid point covered with $\leq 50\%$ of land. The strength of the cyclone must be characterized as strong for at least one of the time steps, and weak, open cyclones are discarded. The time of the pressure minimum needs to be within the period 1st of October - 30th of April (henceforth referred to as the extended winter season), since these are the months during which most PLs develop. The great circle distance, which is the shortest distance between two points on a sphere (Warner, 2011), must be larger than 300 km between the first and the last point of the track to avoid stationary cyclones. No condition regarding a CAO is included, as this is found to reduce the number of matches with the STARS database.

In addition to the selection program, a program which cuts off the tracks reaching land is run. If the time step in which the track reaches land is denoted t, and the next time step is denoted $t + 1$, the cutting of the tracks reaching land can be explained as following: if the distance between track points at t and $t + 1 > 200$ km, the track is cut at time t. If the distance between track points at t and $t+1 \leq 200$ km, the track is cut at time $t+1$.

After the selection and cutting programs have been run, the next step is to select PLs that reach the coast of Norway. This is done with the help of a land-sea mask, which is a file containing values of 0 for grid points over ocean, and 1 for grid points over land. In addition, the coast of the land-sea mask was expanded with a seaward distance of 200 km, meaning that a PL reaching within 200 km of the coast, would in fact be perceived as reaching the coast. This was done because of the fact that PLs usually have a radius of at least 200 km. Thus, a PL with a radius of 200 km would indeed have an effect on the coast. A box of Norway was selected from the expanded mask and is shown in Fig. 2.7a.

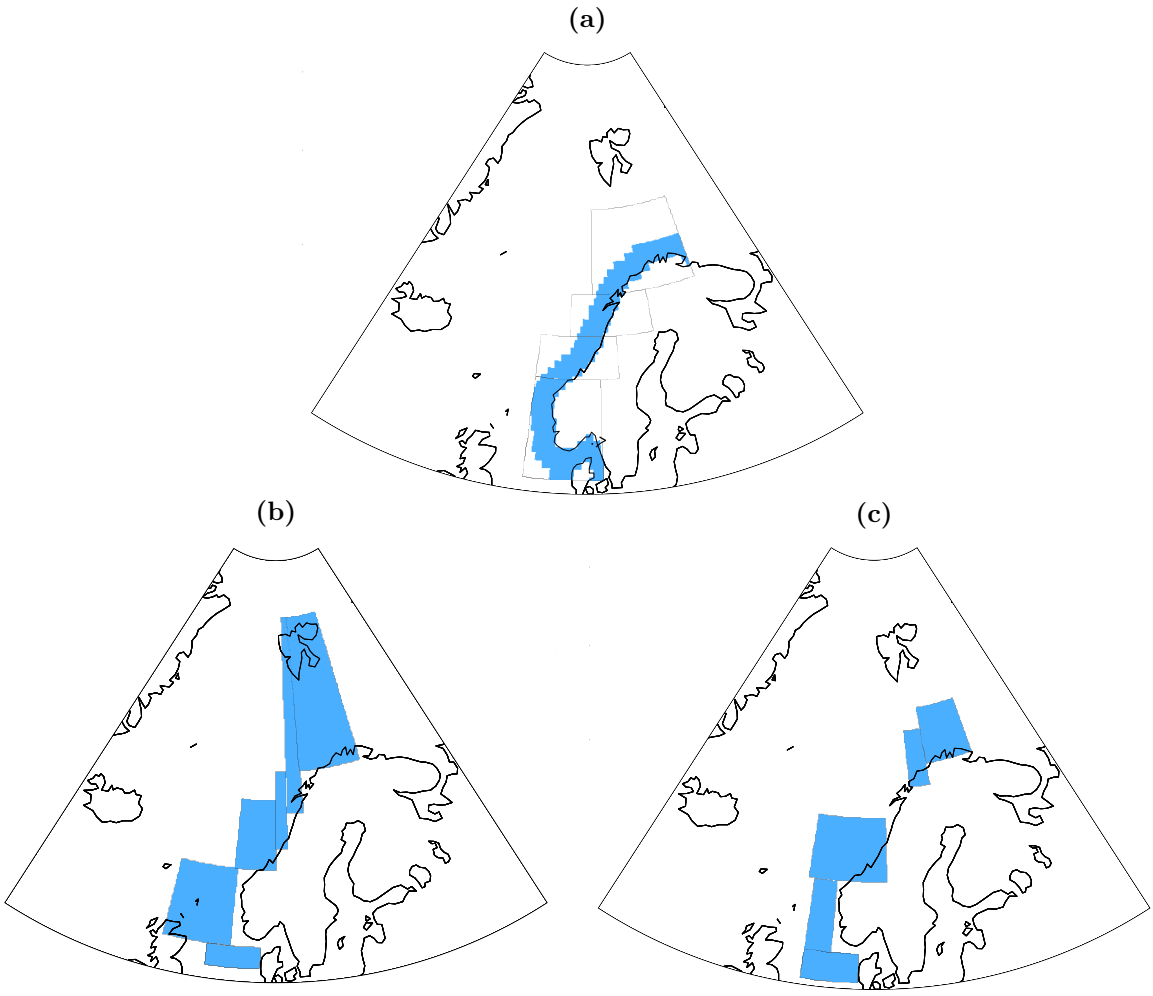

Figure 2.7: A representation of the locations of (a) the expanded coast of Norway, as well as (b) fishery areas and (c) oil platforms, all shaded in blue.

Masks have been created to select PLs that reached areas in the Nordic seas used for fishery and by oil platforms, shown in Fig. 2.7b and Fig. 2.7c, respectively. For the fishery areas, the created mask was based on a map found on the Norwegian Fishery Directorates (NFD) home page [6] (Fig. 2.8a). For the oil platforms, the mask created was based on a map found on the Norwegian Petroleum Directorates (NPD) home page[7] (Fig. 2.8b).

[6] http://kart.fiskeridir.no/

[7] http://gis.npd.no/factmaps/html_20/

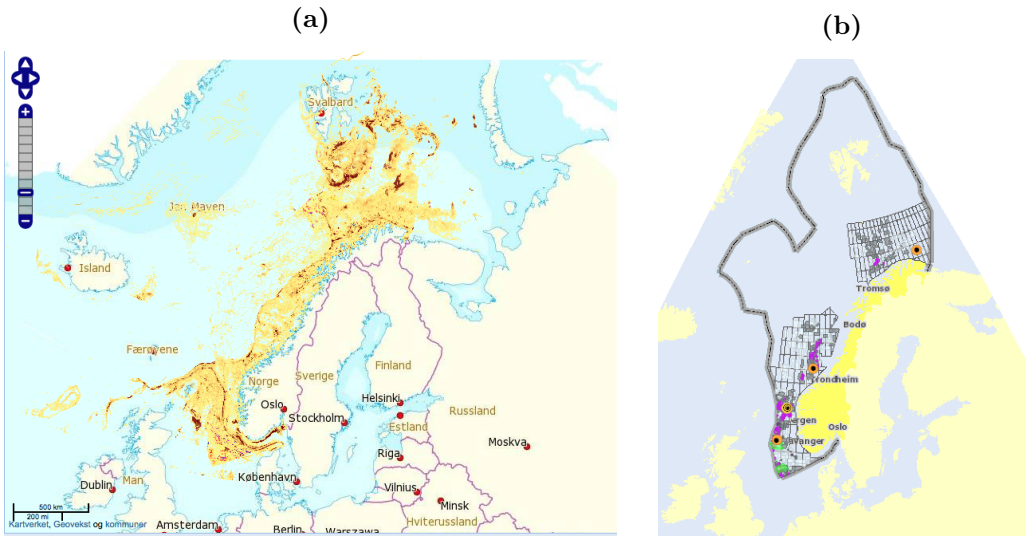

Figure 2.8: Maps of (a) fishery areas and (b) oil platforms in the Nordic seas. Figures taken from `http://kart.fiskeridir.no/` and `http://gis.npd.no/factmaps/html_20/`, respectively.

2.3 Polar low density calculation

To make density plots of the travel paths of PLs (track density), where PLs have their genesis and lysis (cyclogenesis and lysis densities) and where they reach fisheries, oil platforms and the coast of Norway, a program that counted the number of PLs in each grid box was utilized. The number of PLs in each grid box $C(\lambda, \varphi)$ was weighted by the area of the grid box:

$$C(\lambda, \varphi) = \frac{C(\lambda, \varphi)}{a^2 \Delta\lambda \left(\sin(\varphi + \Delta\varphi/2) - \sin(\varphi - \Delta\varphi/2)\right)} , \tag{2.10}$$

where λ and φ are the longitude and latitude, respectively, and a is the radius of the Earth. Next, $C(\lambda, \varphi)$ is weighted with the neighboring grid boxes in a radius b_1 to get a density distribution $d(\lambda, \varphi)$:

$$d(\lambda, \varphi) = \frac{\sum\limits_{\lambda', \varphi', r < b_1} \frac{{b_1}^2 - r^2}{{b_1}^2 + r^2\left(\frac{{b_1}^2}{{b_2}^2} - 1\right)} C(\lambda, \varphi)}{\sum\limits_{\lambda', \varphi', r < b_1} \frac{{b_1}^2 - r^2}{{b_1}^2 + r^2\left(\frac{{b_1}^2}{{b_2}^2} - 1\right)}} , \tag{2.11}$$

where r is the distance between (λ, φ) and (λ', φ'), and the values $b_1 = 250$ km and $b_2 = 100$ km are used. Since the unit of $d(\lambda, \varphi)$ is the number of PLs per km^2, $d(\lambda, \varphi)$ is multiplied by 10000 and divided by the number of extended winters, to make the unit: number of PLs per 10000 km^2 per extended winter season. The NCAR Command Language, designed by the

National Center for Atmospheric Research for scientific visualization and data processing[8], was utilized to plot the density distributions.

2.4 Forward and reverse shear conditions

In this thesis, the method to calculate the angle between the thermal wind and the mean wind is based on Kolstad (2006) and Terpstra et al. (2016). The lower boundary of the thermal and mean wind was chosen to be 925-hPa, since wind at this height is not affected too much by surface friction in the boundary layer. The upper boundary was chosen to be 700-hPa, since increasing the boundary further did not show a significant effect. Therefore, winds between 925-hPa and 700-hPa were considered as representative for the conditions in the troposphere. The thermal wind $\mathbf{v}_\mathrm{t}(u_\mathrm{t}, v_\mathrm{t})$ between 925-hPa and 700-hPa is calculated with:

$$u_\mathrm{T} = -\frac{1}{f}\frac{\partial(\phi_{700} - \phi_{925})}{a\partial\varphi} \ , \tag{2.12}$$

$$v_\mathrm{T} = \frac{1}{f}\frac{\partial(\phi_{700} - \phi_{925})}{a\cos\varphi\partial\lambda} \ , \tag{2.13}$$

where f is the Coriolis parameter, ϕ_{925} and ϕ_{700} are the geopotential height at 925-hPa and 700-hPa, respectively, φ and λ are the latitude and longitude, respectively, and a is the radius of the Earth. The mean wind, $\bar{\mathbf{v}}$=$(\bar{u}, \bar{v})$, is defined as the vertically averaged wind between 925-hPa and 700-hPa. The angle α

$$\alpha = \arccos\left(\frac{\mathbf{v}_\mathrm{t} \cdot \bar{\mathbf{v}}}{|\mathbf{v}_\mathrm{t}||\bar{\mathbf{v}}|}\right) \ , \tag{2.14}$$

between the thermal wind and mean wind, is utilized to distinguish between FS and RS. The angle was averaged over a radius of 200 km around the genesis point of the PLs, since this is a representative size at their early lifetime. This thesis uses the same classification as Kolstad (2006), which classifies PLs with $0° \leq \alpha \leq 45°$ as FS cases, and PLs with $135° \leq \alpha \leq 180°$ as RS cases.

[8] http://www.ncl.ucar.edu

2.5 Indices of the North Atlantic Oscillation and Scandinavian blocking

This thesis investigates the link between the low-frequency variability of the atmosphere and the occurence of PLs. Two large-scale patterns are studied, the NAO and SB. The daily NAO index was found at the website of the National Weather Service, Climate Prediction Center's webpage[9]. The daily SB index was made by Michel (2016), based on a blocking index definition for the NH by Tibaldi and Molteni (1990), and its calculation is described below.

The method for calculating the SB index made use of a climatology of the average 500-hPa geopotential height $\bar{\phi}$ for the extended winter months from 1979 to 2015. Two gradients were calculated, the southern geopotential height gradient $GHGS$ and the northern geopotential height gradient $GHGN$:

$$GHGS = \frac{Z(\varphi_0) - Z(\varphi_\mathrm{s})}{\varphi_0 - \varphi_\mathrm{s}} \ , \tag{2.15}$$

$$GHGS = \frac{Z(\varphi_\mathrm{n}) - Z(\varphi_0)}{\varphi_\mathrm{n} - \varphi_\mathrm{o}} \ , \tag{2.16}$$

where $Z = \frac{\phi}{g}$, where g=9.80665 m s^{-2} is the gravity constant. φ is the latitude with the values: $\varphi_\mathrm{n} = 80°\mathrm{N}{+}\delta$, $\varphi_0 = 60°\mathrm{N}{+}\delta$ and $\varphi_\mathrm{s} = 40°\mathrm{N}{+}\delta$, where $\delta = -5°$, $\delta = 0°$ and $\delta = 5°$ values were utilized. Next, a longitude was defined as "blocked" if the two following conditions were satisfied for at least one of the δ values:

$$(1) \ \ GHGS \ > \ 0 \tag{2.17}$$

$$(2) \ \ GHGN \ < \ -10 \, m/° \ latitude. \tag{2.18}$$

The longitudes between 0° to 30°E were considered to identify a pattern of SB, and a blocking was considered to occur when half of the longitudes where defined as blocked. A composite of the 500-hPa geopotential height anomaly ϕ', defined as:

$$\phi'(\lambda, \varphi, t) = \phi(\lambda, \varphi, t) - \bar{\phi}(\lambda, \varphi) \ , \tag{2.19}$$

[9] http://www.cpc.ncep.noaa.gov

was made for the blocked time steps, and standardized to obtain an SB index I:

$$I(t) = \frac{P(t) - \bar{P}}{\sqrt{\frac{1}{nt}\sum_{t=1}^{nt}\left(P(t) - \bar{P}\right)^2}} , \tag{2.20}$$

where λ is the latitude, t is the time step of the considered period and nt is the total number of time steps. P(t) is the projection of ϕ', projected on the SB 500-hPa geopotential height anomaly ϕ'_{SB}:

$$P(t) = \frac{1}{\sum_{(\lambda,\phi)\epsilon D}\cos\phi}\sum_{(\lambda,\phi)\epsilon D}\phi'(\lambda,\phi,t)\phi'_{\mathrm{SB}}(\lambda,\phi)\cos\phi , \tag{2.21}$$

where D is the domain and $\bar{P}$ is the time mean of the projection.

The indices were averaged for the dates of PL events reaching Norway. The reason for choosing the daily indices of NAO and SB and not the monthly indices, is that both patterns have time scale of 7-10 days, meaning that several phases can occur during one month. Thus, monthly indices do not represent the value at the day of the PL event.

The standard deviation (σ) and the correlation *corr* between the indices and the number of PL events time series were calculated:

$$\sigma_{\mathrm{X}} = \sqrt{\frac{1}{N-1}\sum_{i=1}^{N}\left(X_{\mathrm{i}} - \bar{X}\right)^2} , \tag{2.22}$$

$$corr\,(X,Y) = \frac{cov\,(X,Y)}{\sigma_{\mathrm{x}}\sigma_{\mathrm{y}}} , \tag{2.23}$$

where the covariance *cov*

$$cov(X,Y) = \frac{1}{N-1}\sum_{i=1}^{N}\left(X_{\mathrm{i}} - \bar{X}\right)\left(Y_{\mathrm{i}} - \bar{Y}\right) , \tag{2.24}$$

was needed to calculate *corr*. X refers to the indices, Y refers to the number of PL events and N is the the total number of days considered. *corr* was calculated to investigate the statistical dependence between the indices and the number of PL events, and σ was calculated to investigate the spread of the index values.

3 Climatology of polar lows for the period 1979-2015

As described in the previous chapter, the Melbourne detection and tracking algorithm has been applied to ERAI data. The tracks obtained have then been selected to only retain the PLs reaching Norway, fishery areas, and oil platforms, which are the focus of this chapter. The spatial distribution of these PLs is studied as well as the influence of the large-scale genesis environment on the PL distribution.

3.1 Polar lows in the Nordic seas

Fig. 3.1 shows the track density, genesis and lysis of all of the 6747 tracks selected as PLs in the Nordic seas in the period 1979-2015. The track density in Fig. 3.1a shows the averaged positions of the selected PL tracks, for all time steps. The distribution is quite evenly spread out in the domain, but two maxima west of Svalbard and north of Norway are found, indicating that these are the areas where the highest numbers of PLs reach.

The genesis density in Fig. 3.1b has two local maxima northeast of Iceland and west of Svalbard, likely formed in CAOs from the Greenland ice edge and the Arctic sea ice edge, respectively. Additionally, there is a strong local maximum just north of the coast of Northern Norway, which is likely explained by PLs forming at the southern edge of a CAO coming from the north, generating a suitable PL development area in this region as well. Another possible reason, although less likely, is a CAO off the coast of northern Norway.

The lysis density of the PL tracks is shown in Fig. 3.1c, indicating an evenly distribution throughout the domain with a clear maximum southwest of Svalbard. Since PLs in general do not travel large distances, it is reasonable that the maximum in lysis density is found close to the three maxima in genesis density.

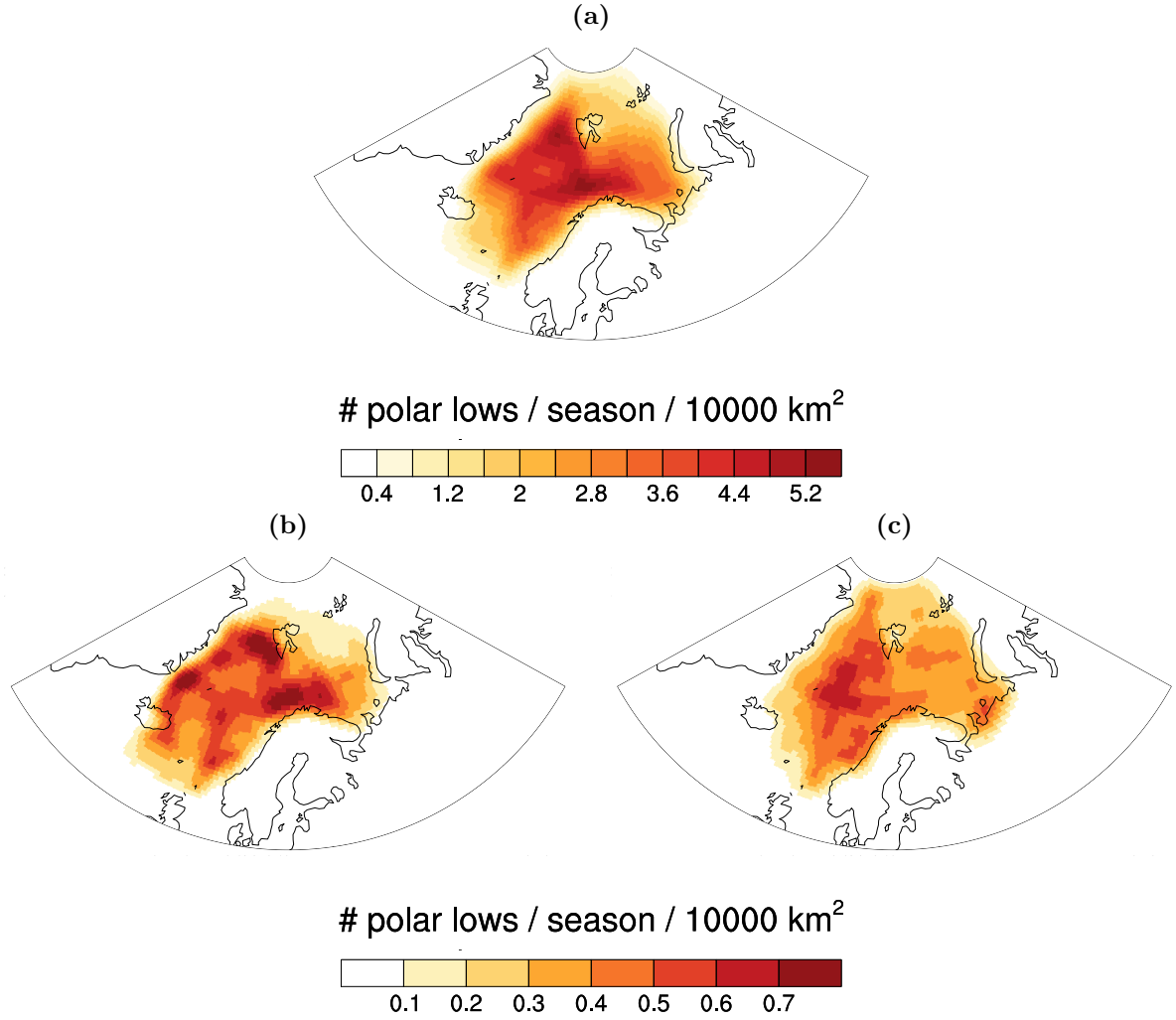

Figure 3.1: (a) Track density, (b) genesis density, and (c) lysis density for PLs in the Nordic seas (shading, units: number of PLs per extended winter season per 10000 km^2).

Figure 3.2 shows the genesis density of the PLs reaching land, and the place where they make landfall. The coastal areas mostly affected by landfall of PLs are the western coast of Svalbard, the coast of Norway, though mostly the northern coast, as well as the northwest of Russia and the island Novaya Zemlya. There is also a well defined maximum in landfall density at the western coast of Svalbard, likely caused by CAO from the Greenland ice edge, or the Arctic sea ice edge. Correspondingly, the largest genesis density is mostly found in the Barents Sea, as it is close to the areas of landfall. The genesis density found in the Greenland and Norwegian seas can most likely be linked to the PLs making landfall at the Norwegian coast and the western coast of Svalbard.

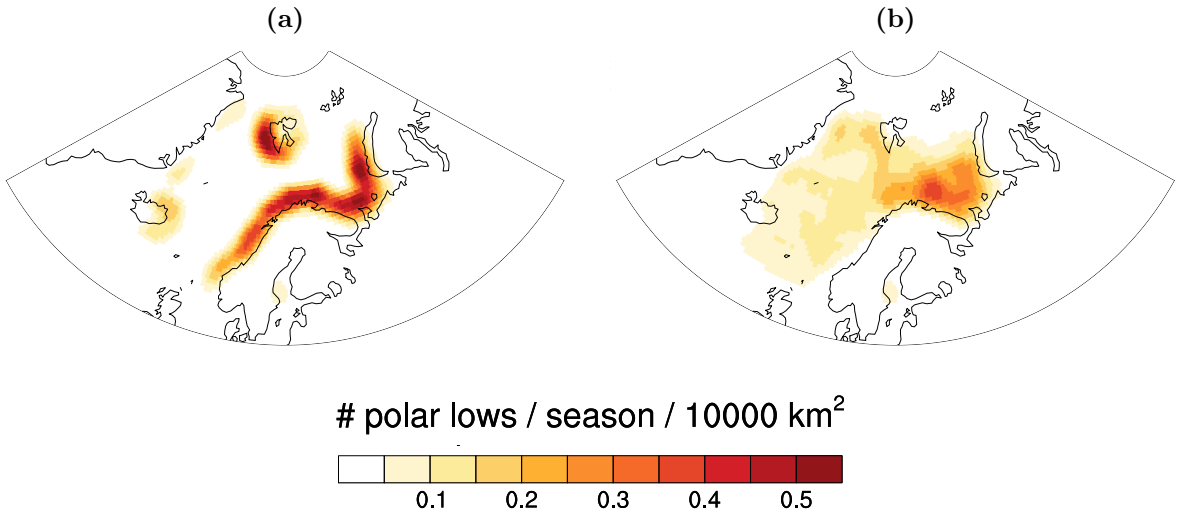

Figure 3.2: Density distribution of (a) PLs making landfall in the Nordic seas and (b) genesis of PLs making landfall in the Nordic seas (shading, units: number of PLs per extended winter season per 10000 km^2).

3.2 Polar lows reaching fisheries and oil platforms

The requirement for reaching a fishery area or an oil platform was that one of the track points was in the domain of the boxes in Fig. 2.7b and c, respectively. The reader should note that the areas based on the boxes from Fig. 2.7b and c are very coarsely defined, and does not give a perfect representation of the areas designated to fishery activity and oil platforms.

3.2.1 Spatial distribution

Figure 3.3 shows the density for the PLs reaching locations designated to fishery, along with the respective genesis areas. A clear maximum in density of PLs reaching fisheries is found south of Svalbard, implying that this area is the most dangerous for sailors to travel during the winter months. The genesis areas are found quite close to the areas where they reach fisheries, partly explained by the fact that some of the PLs are generated in the fishery locations and partly by the fact that the PLs do not travel far.

Figure 3.4 shows the density for the PLs reaching oil platforms, as well as the corresponding genesis areas. The maximum north of the northern coast of Norway is a bit stronger than the maximum northwest of Bergen, due to the higher PL track density in this region (Fig. 3.1a). The oil platforms located outside the coast of southern Norway

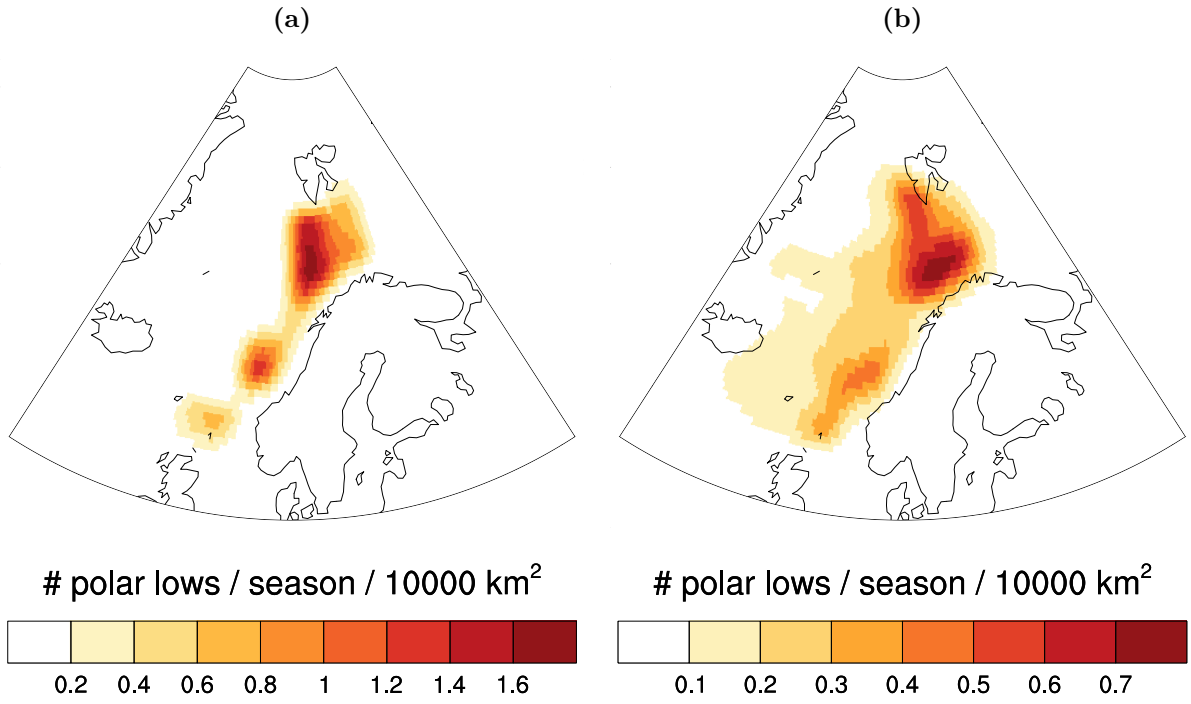

Figure 3.3: (a) PLs reaching fisheries and (b) genesis of PLs reaching fisheries (shading, units: number of PLs per extended winter season per 10000 km^2).

(Fig. 2.7c) are not affected because they are outside of our domain. For the same reasons as for the fisheries case, the genesis is found close to the area where the PLs reach the oil platforms.

3.2.2 Oil platform evacuations

An investigation was made to explore PL cases leading to oil platform evacuations. A list of 35 weather-related oil platform evacuations was provided on our request by the Norwegian Petroleum Safety Authority, revealing the dates and locations of evacuation. 31 evacuations occurred during the extended winter months, and were cross-checked with the tracks in the Nordic seas. PLs occurring in the time period two days before to two days after evacuation were plotted, to investigate if a PL was the cause for evacuation. If a PL was the cause of an evacuation, it would most likely be due to the strong winds associated with it, leading to high waves and danger for the people working there.

Out of the total of 31 evacuations occurring in the extended winter months, only one was regarded as a good match with the PL tracks: the evacuation of the oil platform Vesle-

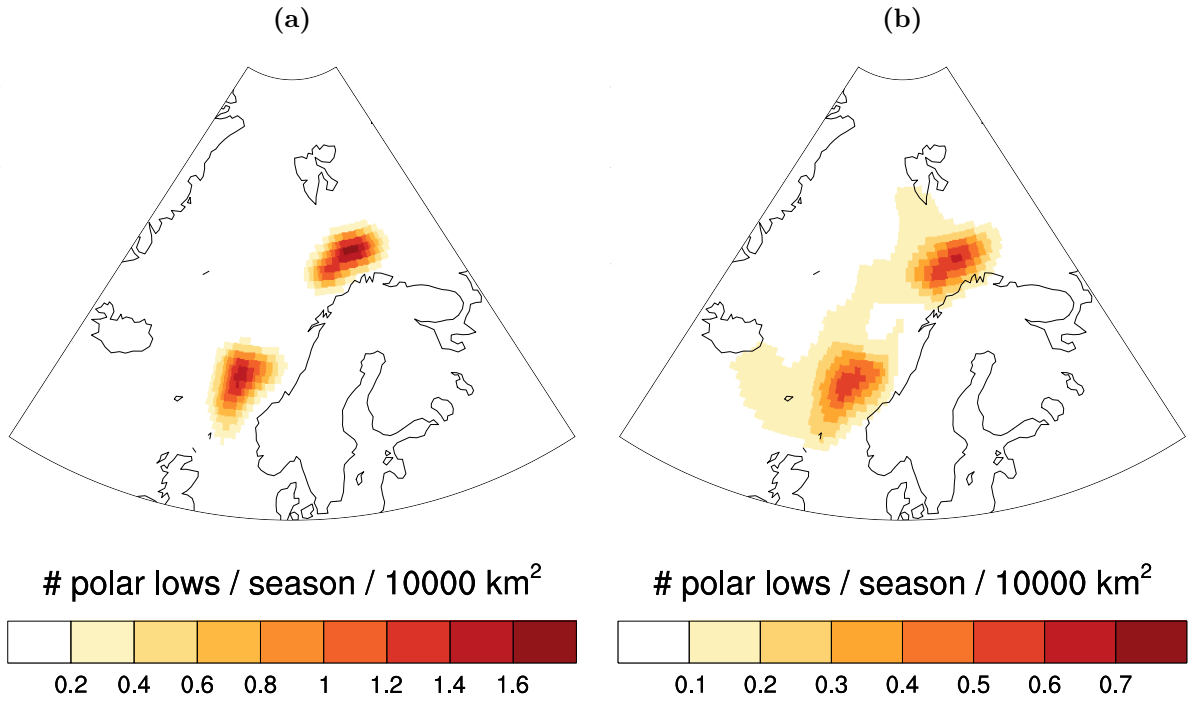

Figure 3.4: (a) PLs reaching oil platforms and (b) genesis of PLs reaching oil platforms (shading, units: number of PLs per extended winter season per 10000 km^2).

frikk outside the coast of Bergen, on the 12$^{\text{th}}$ of January 2012, reported at 11:00 UTC. It is worth to note that most of the evacuations on the list occurred in oil platforms positioned outside the southern and western coast of Norway, decreasing the chance of matching with PL tracks, as the track density has larger values further north and some of the platforms are located outside of our domain. It can be assumed that most of the evacuations outside the southern and western coast of Norway are caused by mid-latitude cyclones, which are discarded in the selection process.

Figure 3.5 shows the PL track occurring around the time of evacuation of Veslefrikk. It is evident that the track reaches the coast of Norway north of the location of Veslefrikk. The strongest winds are usually on the south of the low pressure system, which means that the strongest winds are close to the oil platform.

To investigate if this track was indeed a PL, the ERAI reanalyses of MSLP, and temperature and wind at 850-hPa were plotted. Figure 3.6 shows the evolution of the MSLP field in the hours before evacuation of Veslefrikk. It is evident that a low value of MSLP

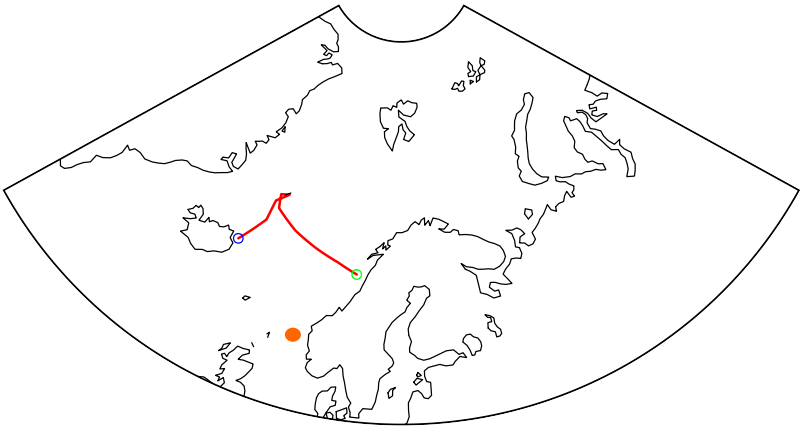

Figure 3.5: The track matching with the date of the evacuation of the oil platform Veslefrikk, with the blue marker indicating the genesis point, the green marker indicating the lysis point and the orange circle indicating the approximate location of Veslefrikk.

is positioned at the southwestern tip of Greenland at 00 UTC 8th of January, which intensifies as time progresses, seemingly due to the orography of Greenland, as the flow over mountainous terrain causes an increase in vorticity (Markowski and Richardson, 2010). The following days the low travels towards Norway and makes landfall around 00 UTC 12th of January.

The ERAI reanalyses of the 850-hPa temperature and wind in the days prior to the evacuation (Fig. 3.7), show no sign of a CAO from Greenland. Thus, it can be concluded that the evacuation of the oil platform Veslefrikk was most likely caused by a cyclone induced by orography, not a PL.

3.3 Polar lows making landfall in Norway

This section deals with the PLs reaching the expanded coast of Norway (Fig. 2.7a).

3.3.1 Spatial distribution

Figure 3.8 shows the density for the PLs making landfall in Norway, along with the respective genesis areas. Evidently, there are no PLs making landfall at the southern coast of Norway, corresponding with Fig. 3.2a. Most of the PLs make landfall north of Trondheim. However, some PLs make landfall along the western coast as well. It is clear from Fig. 3.8b that the main areas of genesis are found west and north of Norway, with the largest densi-

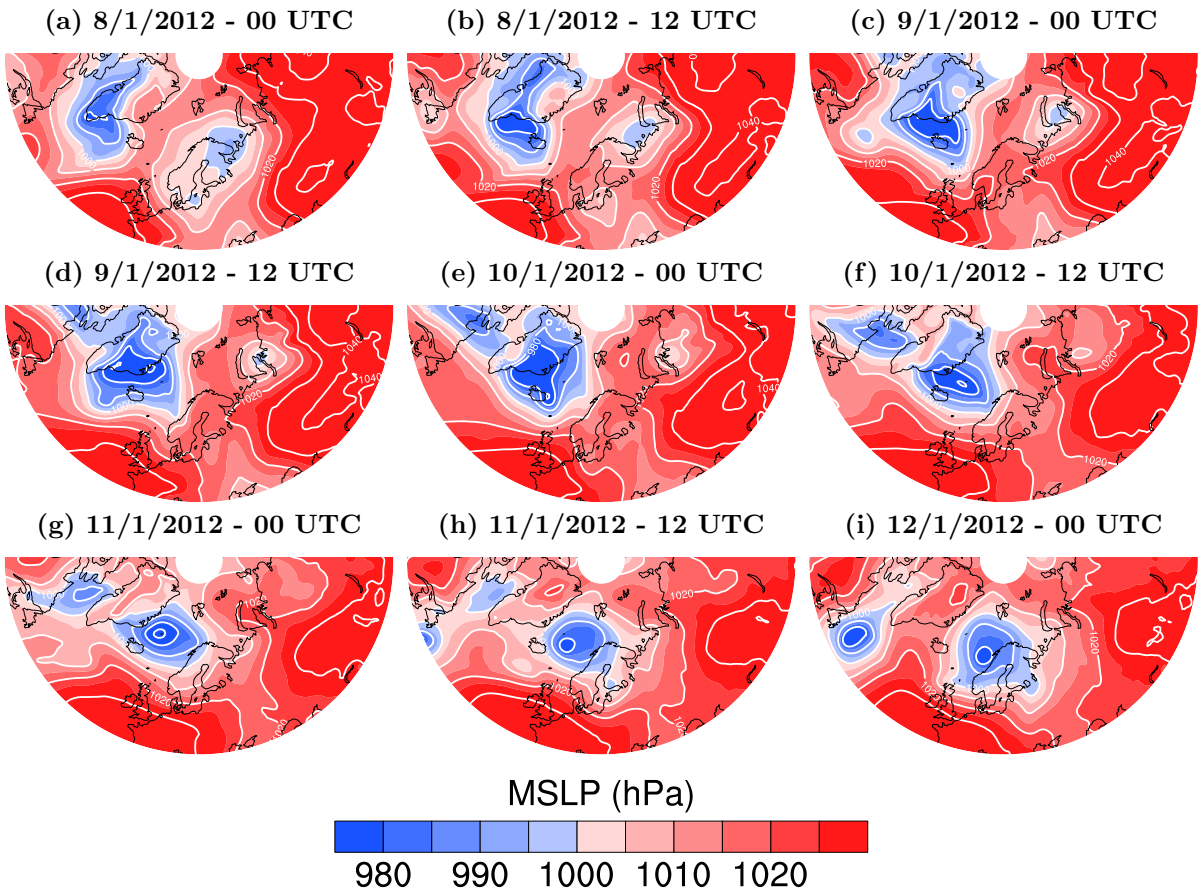

Figure 3.6: MSLP field evolution (shading, units: hPa) in the days prior to the the evacuation of the oil platform Veslefrikk, starting at (a) 00 UTC 8th of January and ending at (i) 00 UTC 12th of January, 12 hours before the evacuation was reported. 12 hour interval are used.

ties quite close to the coast of Norway. Two local maxima are found northwest of Bergen and west-northwest of Tromsø. The latter maximum in genesis density is fairly similar to the results of genesis density found by Zahn and von Storch (2008), who performed a long-term climatology of PLs in the period 1948-2006 by detecting and tracking PLs in several regional climate model simulations to downscale a set of global climate change scenarios, though they found the maximum of genesis to be further off the coast.

A climatology of PLs in the Nordic seas using infrared satellite imagery published by Noer et al. (2011), also has comparable results. Noer et al. (2011) captured a weak, local maximum of PLs in the area around Tromsøflaket, outside the coast of Tromsø, close to the local genesis maximum shown in Fig. 3.8b. The PLs generated in this area can likely be linked to CAOs occurring in the Svalbard region (Noer et al., 2011). The relatively warm

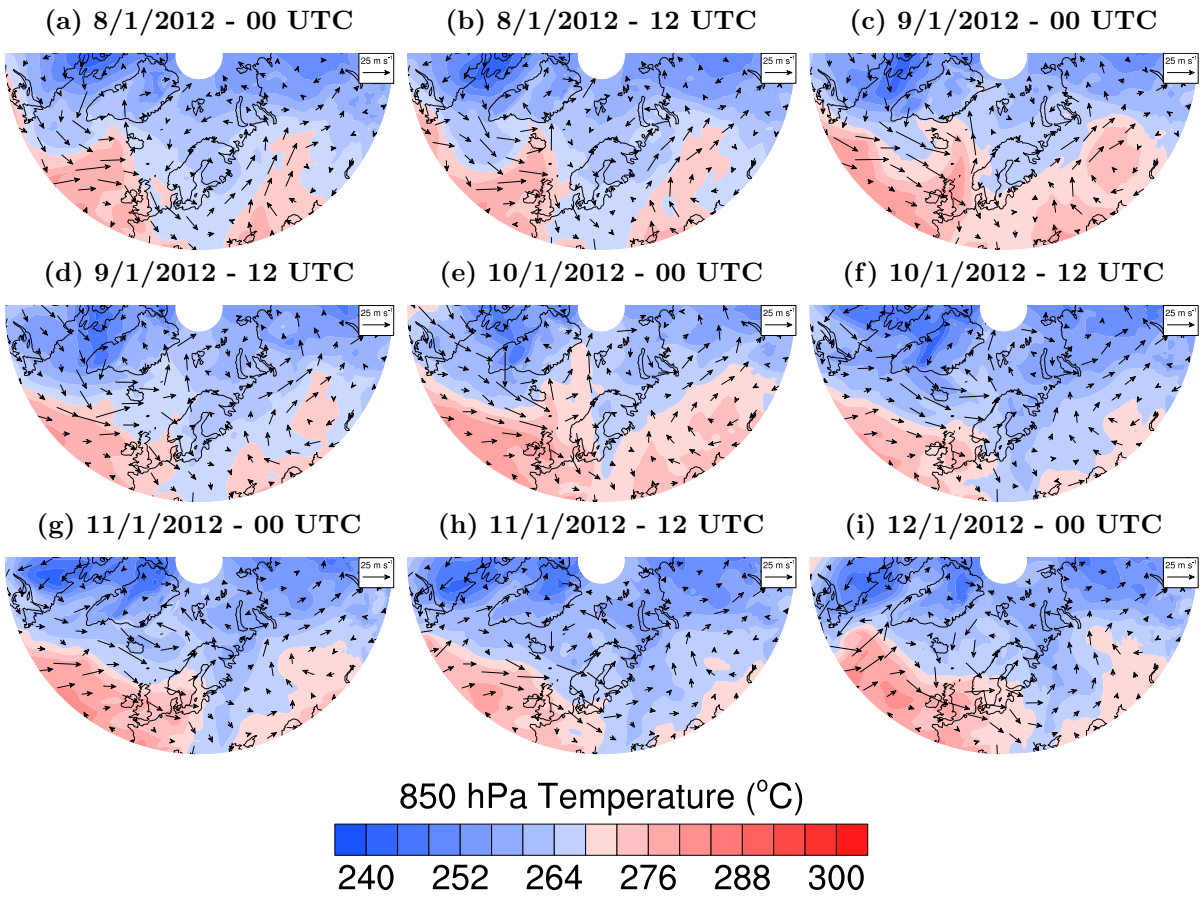

Figure 3.7: 850-hPa temperature (shading, units: °C) and 850-hPa wind field (arrows, units: m s^{-1}) evolution in the days prior to the evacuation of the oil platform Veslefrikk, starting at (a) 00 UTC 8th of January and ending at (i) 00 UTC 12th of January, 12 hours before the evacuation was reported. 12 hour interval are used.

water of the Norwegian Atlantic Current flows northward along the Norwegian coast, and creates favorable conditions for intensification of PLs generated by CAOs in northerly flow from Svalbard. Fig. 3.8a shows that the maximum in density of PLs making landfall is located south of Tromsø, which is reasonable for PLs generated in northerly flow conditions.

3.3.2 Temporal distribution

A total of 560 PLs made landfall in Norway in the period 1979-2015, which gives an average number of 15.6 PLs per extended winter season, meaning that Norway's coastal community is undoubtedly affected by PLs. However, this number may in fact be too high when comparing with Zahn and von Storch (2008), who found an average number of 56 PLs for each season in the whole North Atlantic, whereas the number of PLs in the Nordic seas was

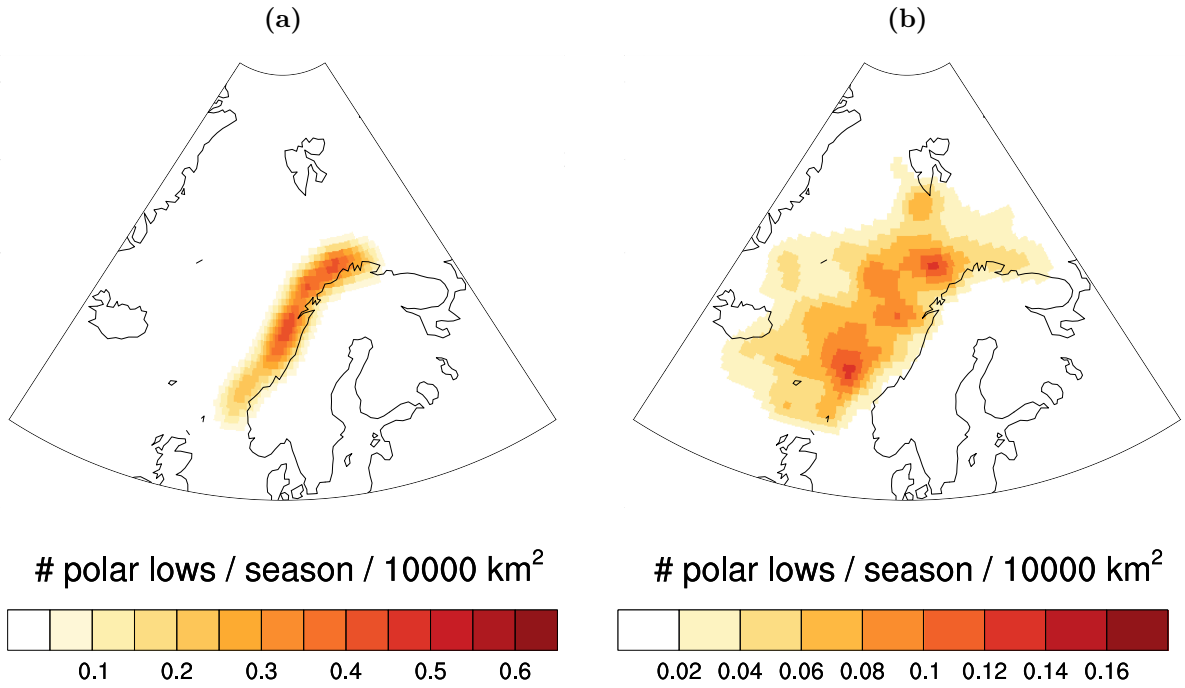

Figure 3.8: (a) PLs making landfall in Norway and (b) genesis of PLs making landfall in Norway (shading, units: number of PLs per extended winter season per 10000 km^2).

found to be 187.4 per extended winter in this thesis. Noer et al. (2011) showed an average of only 12 PLs in the whole area of the Nordic seas per year, for the period 2000-2009. Noer et al. (2011) utilized infrared satellite imagery to develop their climatology, which gives more realistic results than using the automated detection and tracking algorithm, which is quite sensitive to the different input parameters in terms of PL numbers.

This indicates that some of the lows selected by the algorithm could be mesocyclones, cyclones induced by orography or cyclones linked to secondary cyclogenesis, where the latter develops along synoptic fronts enclosed in mature large-scale extratropical cyclones (Rivals et al., 1998). However, some PLs might actually not be detected by the infrared satellite imagery, but caught up by the algorithm, thus explaining that at least a slightly higher number than found by Noer et al. (2011) could be expected.

The annual variability of the PLs making landfall in Norway can be seen in Fig. 3.9. The variability is rather large, with a maximum of 22 PLs/season in winters 91/92 and 13/14, a minimum of 8 PLs/season in winter 00/01, the standard deviation σ being 3.9.

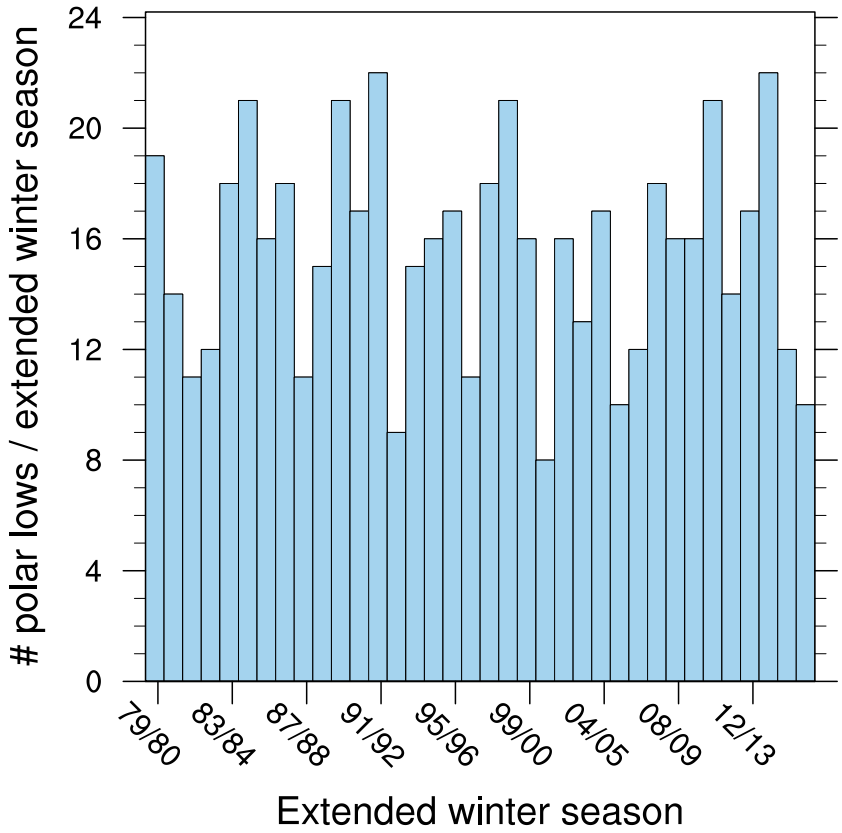

Figure 3.9: Histogram of the number of PLs making landfall in Norway for each extended winter season.

There is a slight decline of PLs making landfall in Norway throughout the whole period, with a negligible trend (-0.025 PLs/season). Thus, there is no clear trend in the annual perspective.

When investigating the months the PLs make landfall in Norway, a more distinctive pattern is found. Figure 3.10 shows the monthly number of PLs making landfall in Norway for the whole period 1979-2015, where the number of PLs in each month has been divided by the number of days in the particular month and multiplied by 30, to make up for the different number of days in each month. Figure 3.10 illustrates that most PLs make landfall in Norway during December, January, and February, when the environment is most suitable for CAOs due to lower atmospheric temperature.

In several PL climatologies, e.g. Wilhelmsen (1985) and Kolstad (2006), a minimum of PLs is found in February, explained by higher frequency of high pressure systems situated

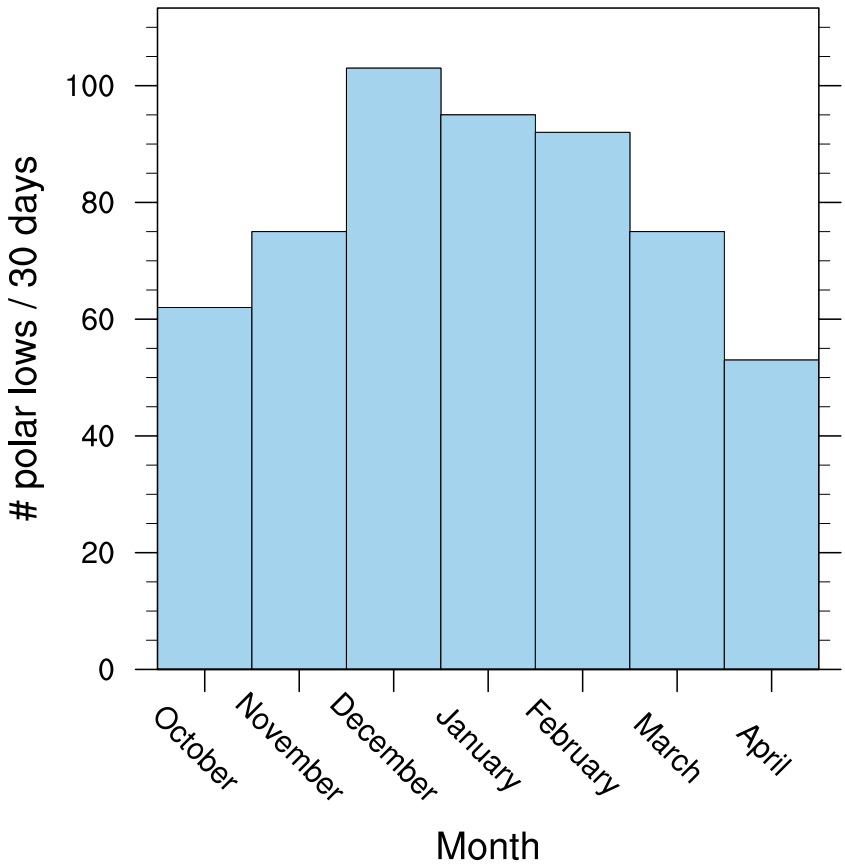

Figure 3.10: Histogram of the number of PLs making landfall in Norway for each extended winter month. The values are weighted to make all of the months 30 days long.

over Scandinavia during this month, thus inducing southerly winds and less favorable conditions for PLs to develop (Kolstad, 2006). As seen from Fig. 3.10, no such minimum in February for the PLs making landfall in Norway is found.

3.4 Sensitivity of the genesis environment on the PL distribution

We have seen in chapter 2 that PLs can form in various environments. Firstly, we look at the influence of the FS and RS conditions on the PLs making landfall in Norway. Secondly, the interaction between PLs making landfall in Norway and the low-frequency atmospheric variability is investigated. Finally, a connection between the two different patterns of low-frequency atmospheric variability and the angle between the thermal and mean wind is sought.

3.4.1 Influence of the forward shear and reverse shear conditions

A distinction of the PLs making landfall in Norway was made based on Terpstra et al. (2016) and Kolstad (2006), classifying PLs depending on the angle between the thermal and mean wind. Conditions with an angle $0° \leq \alpha \leq 45°$ are classified as FS cases, and conditions with $135° \leq \alpha \leq 180°$ as RS cases.

Statistical results

Table 3.1 shows the numbers of PLs classified as FS, RS and the PLs that are classified as neither FS nor RS (NFNR), for both landfall in Norway and for the Nordic seas. Table 3.1 shows that most PLs are classified as NFNR, meaning that the angle between the mean wind and the thermal wind is in the range $45° < \alpha < 135°$. It is also evident from Table 3.1 that PL development occurs more frequently in a FS environment than a RS environment. When comparing the fractions of RS PLs making landfall in Norway and PLs in the Nordic seas, it can be seen that PLs making landfall in Norway occurs more frequently in a RS environment. The fractions of FS and RS PLs in Table 3.1 do not match those in the STARS database, found by Terpstra et al. (2016), where a fraction of 21% (19%) was found to be RS (FS) PLs. This again indicates that some mesocyclones or other cyclone types are included in the selected tracks, which could explain the increased number of FS events.

An investigation was made to see if a RS environment is more favorable for PLs making landfall in Norway than for the Nordic seas, by looking at the distribution of the number of PLs with different angle α between the mean wind and thermal wind, for both PLs mak-

Table 3.1: Numbers and fractions of FS, RS, and NFNR PLs making landfall in Norway and for the Nordic seas.

Area	Shear type	Number	Fraction
Norway	FS	130	23.2 %
	RS	58	10.4 %
	NFNR	372	66.4 %
Nordic seas	FS	1739	25.8 %
	RS	463	6.9 %
	NFNR	4545	67.4 %

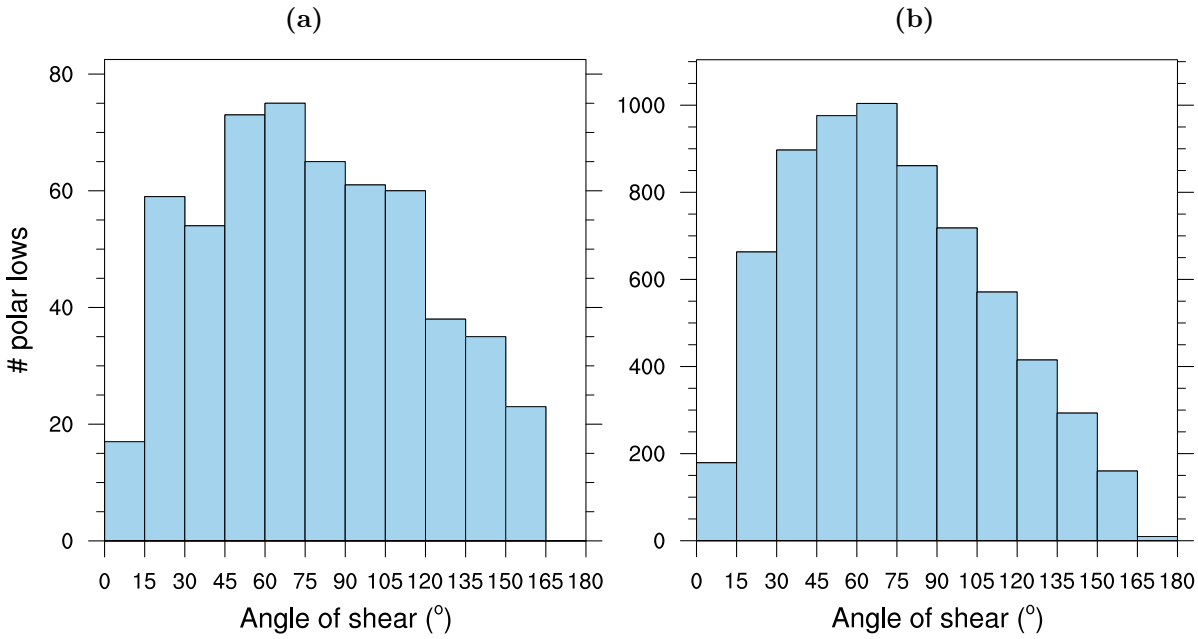

Figure 3.11: Distribution of the angle α between the mean wind and the thermal wind (units: °) for (a) PLs making landfall in Norway and (b) PLs in the Nordic seas, with a 15 ° interval.

ing landfall in Norway and PLs in the Nordic seas (Fig. 3.11). Both environments for PLs making landfall in Norway and PLs in the Nordic seas have a maximum for $45° < \alpha < 75°$, and have a mean angle $\alpha < 90°$. The fraction of PLs with an angle $\alpha > 90°$ is larger for PLs making landfall in Norway than for PLs in the Nordic seas, as well as the fraction of PLs with $\alpha > 135°$.

Composites

Composites of the wind at 925-hPa and 300-hPa at the time of occurrence of FS and RS PLs were made (Fig. 3.12 and 3.13), to better understand their synoptic environment, and to support the explanation for more RS PLs making landfall in Norway. The FS and RS 925-hPa wind patterns show quite contrasting behavior, with generally larger wind speeds for a RS environment (compare Fig. 3.12a and b). The RS environment shows very strong low-level winds in the Atlantic, whereas the winds are less intense and shifted northward over the North Atlantic reaching southern Norway in the FS environment. A cyclonic rotation at the northern coast of Norway is found for the RS environment, whereas the cyclonic rotation is found over the Barents Sea for the FS environment. A stronger zonal upper level jet in the Atlantic is found for RS conditions than for FS conditions (compare

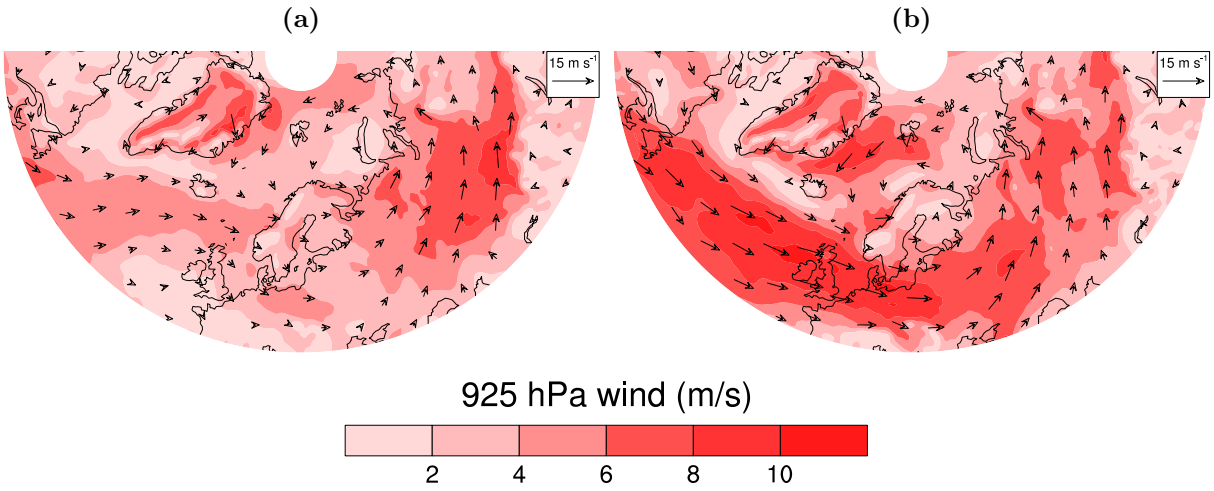

Figure 3.12: Composites of 925-hPa wind (shading and arrows, units: m s^{-1}) for (a) FS and (b) RS conditions for PLs making landfall in Norway. Only the extended winter months are considered.

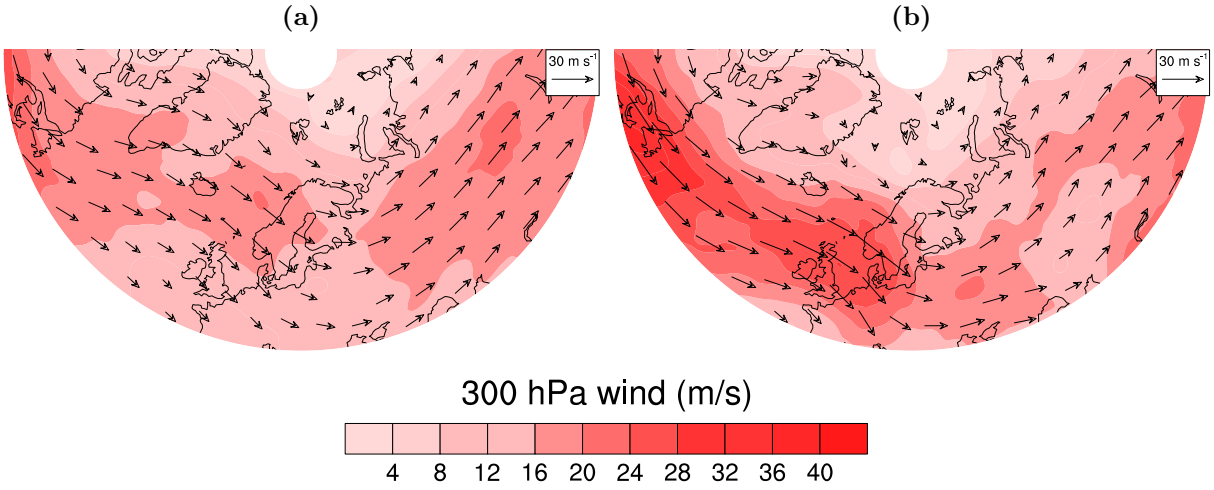

Figure 3.13: Composites of 300-hPa wind (shading and arrows, units: m s^{-1}) for (a) FS and (b) RS conditions for PLs making landfall in Norway. Only the extended winter months are considered.

Fig. 3.13a and b), which suggests more synoptic low pressure systems reaching Scandinavia for a RS environment than for a FS environment.

Figure 3.14 shows the composites of the climatological mean of the 500-hPa geopotential height, and the deviation from the climatological mean for FS and RS environments. There is a higher than normal geopotential height south of Greenland and lower than normal geopotential height northeast of Norway for the FS environment, whereas a lower than normal geopotential height is situated over Scandinavia for RS conditions. However, when comparing the values of deviation with the climatological mean in Fig. 3.14a, it is clear

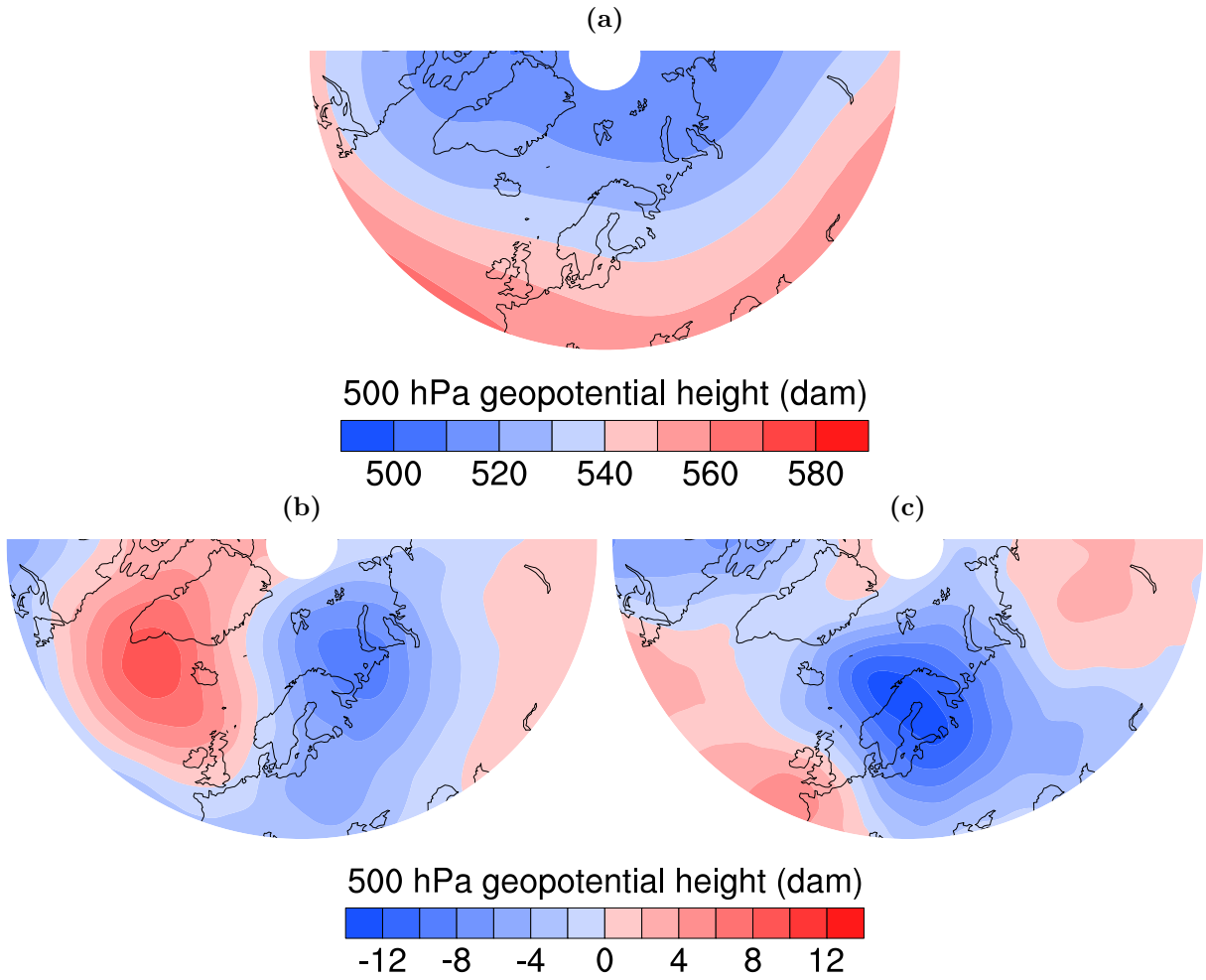

Figure 3.14: Composites of (a) the climatological mean of the 500-hPa geopotential height (shading, units: dam), and the deviation from the climatological mean for (b) FS and (c) RS conditions for PLs making landfall in Norway. Only the extended winter months are considered.

that the deviations are not very large.

Kolstad (2006) states that RS PLs are more likely to develop in the northerly flow following the cold fronts of synoptic-scale cyclones. This is in accordance with the wind patterns found in Fig. 3.12b and 3.13b, and the geopotential height found in Fig. 3.14c. These synoptic-scale storms tend to travel across the Atlantic from the southwest and go as far as the Norwegian and Barents seas (Kolstad, 2006), hence the RS PLs forming behind these storms would be likely to make landfall in Norway. This can explain the higher numbers of RS for PLs making landfall in Norway compared to the Nordic seas. Some of the selected PLs in the RS environment could be secondary cyclones, also developing in

the lee of large-scale cyclones (Rivals et al., 1998).

Spatial distribution

Density plots of the PLs forming in FS and RS environments were made (Fig. 3.15). Fig. 3.15a shows that the largest genesis densities for FS are found south of Svalbard and east of Iceland, corresponding well with the northerly 925-hPa wind flow in these areas found in Fig. 3.12a. The genesis density for RS (Fig. 3.15b) is located closer to Norway, with a small maximum off the coast of northern Norway. This corresponds well with the increase in northerly flow in the area for the RS environment found in Fig. 3.12b and the decrease of geopotential height over Norway in Fig. 3.14c. The resulting areas of landfall (Fig. 3.16) show that FS PLs have a maximum in landfall at the northern coast of Norway, whereas RS PLs have a maximum situated further south, which can be related to the more northward positioned genesis areas for FS PLs.

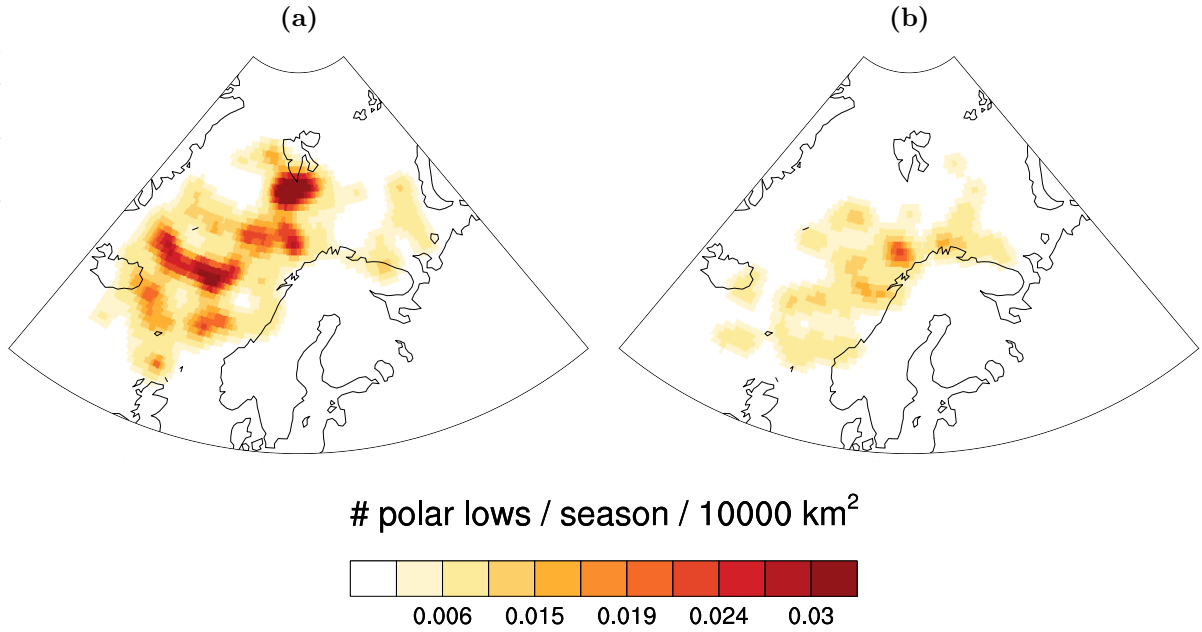

Figure 3.15: Genesis of PLs making landfall in Norway and forming during (a) FS and (b) RS environments (shading, units: number of PLs per extended winter season per 10000 km^2).

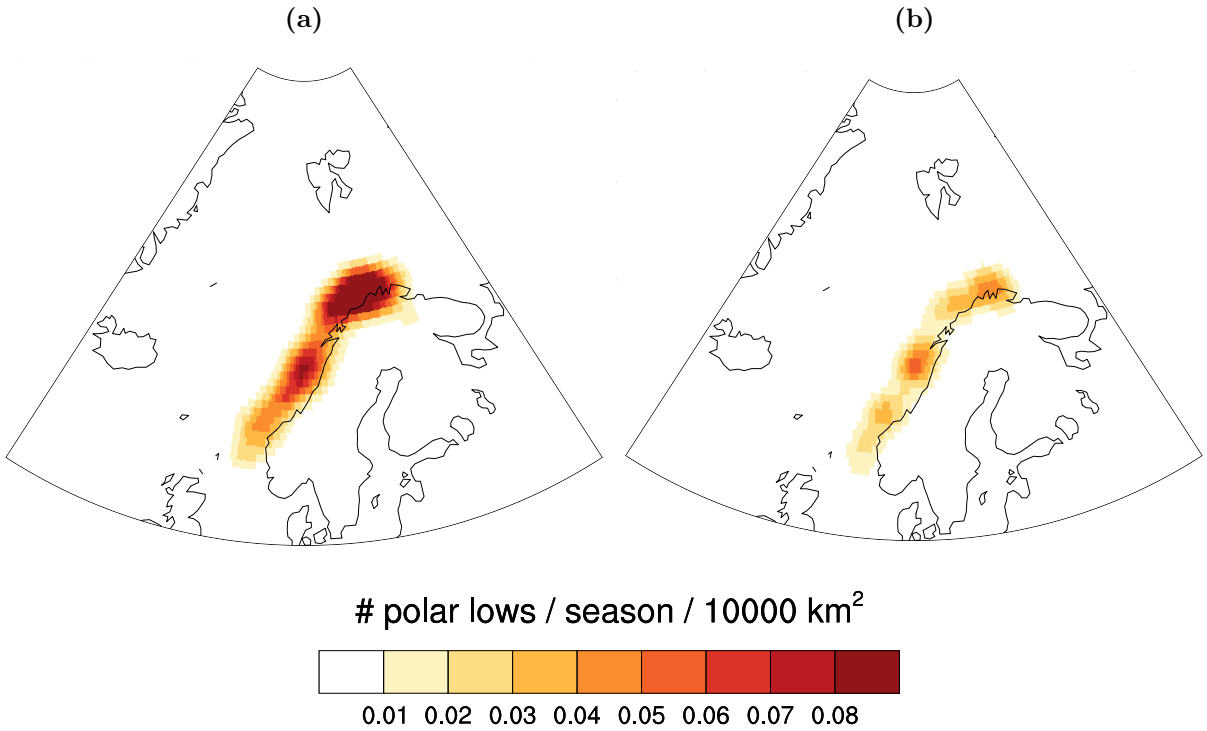

Figure 3.16: PLs making landfall in Norway and forming during (a) FS and (b) RS environments (shading, units: number of PLs per extended winter season per 10000 km^2).

3.4.2 Influence of the North Atlantic Oscillation and Scandinavian blocking

Statistical results

The average indices *avg* for both NAO and SB during PL events making landfall in Norway and for PLs in the Nordic seas were calculated, along with the standard deviation σ and the correlation *corr* between the indices and the number of PLs making landfall in Norway and PLs in the Nordic seas. The results are displayed in Table 3.2. It is clear that the *avg* value of 0.03 for the NAO index when PLs make landfall in Norway is very low, when comparing with typical minima and maxima index values of -3 and 3, respectively. σ is also high, and *corr* is quite low and negative, meaning that no connection between the NAO index and PLs making landfall in Norway is found. For the SB index, on the other hand, the *avg* value of -0.39 is large enough to be considered. The correlation of -0.36 is also high, though the σ value of 1.07 indicates that the spread of the index values is high.

Table 3.2: Showing the *avg*, σ and *corr* values for the NAO and SB indices, for PLs making landfall in Norway and all PLs in the Nordic seas.

Area	Index	*avg*	σ	*corr*
Norway	NAO	0.03	0.83	-0.13
	SB	-0.39	1.07	-0.36
Nordic seas	NAO	0.16	0.83	0.03
	SB	0.01	1.00	0.01

When comparing the index values of NAO and SB for PLs making landfall in Norway and PLs in the Nordic seas in Table 3.2, some clear indications can be found. The *avg* NAO value for the PLs in the Nordic seas is higher than for the PLs making landfall in Norway, but the *corr* value of only 0.03 demonstrates that there is no real connection between the NAO and the PLs forming in the Nordic seas. The *avg* value for SB is much more negative for PLs making landfall in Norway than for PLs in the Nordic seas, meaning that SB- is favorable for PLs making landfall in Norway, but has no significant effect on the PLs in the Nordic seas. SB- is associated with a lower than normal geopotential height centered over Scandinavia and northerly winds in the Barents and Greeland seas (Fig. 1.4), increasing the chance of PLs making their way to the Norwegian coast from CAOs from the north.

Another way of investigating the NAO and SB effects on PLs making landfall in Norway is to count the PLs during negative and positive index values, as shown in Table 3.3, where only the PLs with at least an index higher (lower) than plus (minus) one standard deviation were counted for positive (negative) index value. Table 3.3 shows that the PLs

Table 3.3: Fractions of PLs making landfall in Norway when their genesis or the time at which they reach the coast is during NAO+, NAO-, SB+ and SB-. The fractions are calculated from the total number of 560 PLs making landfall in Norway.

	Genesis	Landfall
NAO+	17.3%	20.7%
NAO-	16.6%	24.6%
SB+	6.2%	4.5%
SB-	23.7%	42.3%

making landfall in Norway have the same probability to have their genesis during both phases of the NAO, whereas at the time they reach the coast, NAO+ conditions are more likely than NAO- conditions. For SB, the difference between the two phases is much more prominent. There is a clear indication that PLs making landfall in Norway occurs more often during SB- conditions than during SB+ conditions, reflected both in the genesis and landfall numbers, though a much higher value for landfall than for genesis is found.

Spatial distribution

Next, the different index signs of the PLs making landfall in Norway are investigated through density plots of their genesis and landfall positions. Figures 3.17 and 3.18 show the genesis and landfall, respectively, of the PLs making landfall in Norway for both NAO+ and NAO-, again selected only when the positive (negative) index value is larger (smaller) than plus (minus) one standard deviation. Figure 3.17 shows that the genesis of PLs making landfall in Norway have greater densities in the southern area of the domain for NAO+, whereas for NAO- the maxima in genesis are found south of Svalbard and west of the northern coast of Norway. The genesis is in general found closer to the coast of

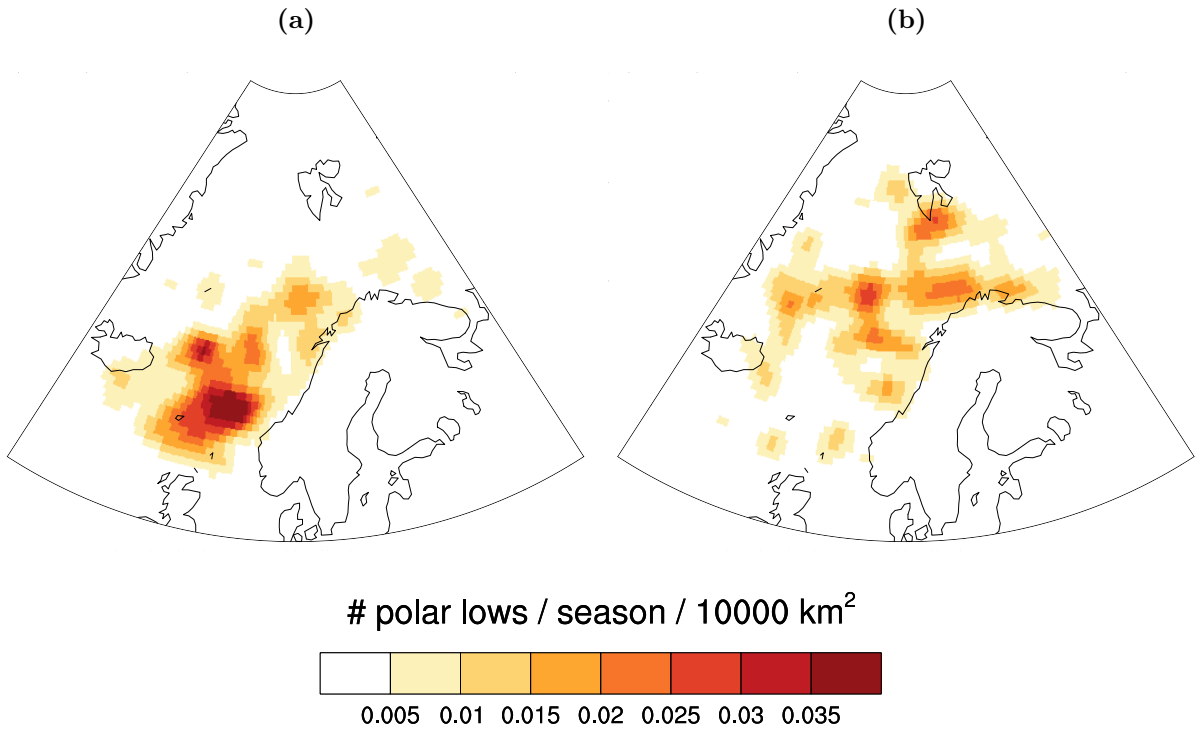

Figure 3.17: Genesis of PLs making landfall in Norway during (a) NAO+ and (b) NAO- (shading, units: number of PLs per extended winter season per 10000 km^2).

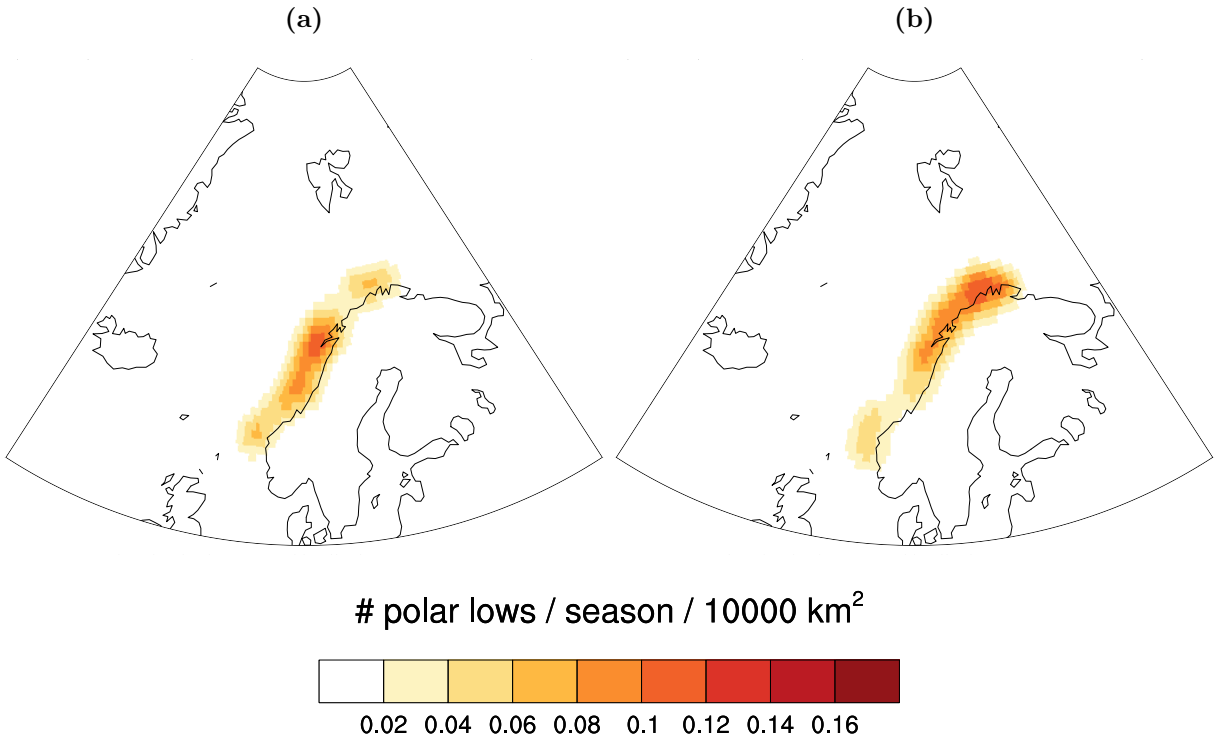

Figure 3.18: PLs making landfall in Norway and forming during (a) NAO+ and (b) NAO- (shading, units: number of PLs per extended winter season per 10000 km^2).

Norway during NAO-. The more southward position of genesis is reflected in Fig. 3.18, with landfall density found mostly around Trondheim and southwards during NAO+, and landfall density found mostly in the northern part of Norway during NAO-.

The reason for the more northward positioned genesis density for NAO- compared to NAO+ can be explained by investigating Fig. 1.3. For NAO-, enhanced anticyclonic low level winds are found over Greenland, due to higher than normal pressure, which means off-ice flow from Greenland, as well as northerly winds in the Svalbard region, thus increasing the chances of CAOs over the Greenland and Norwegian seas. As for the large genesis density found northwest of Bergen for NAO+, this could be explained by secondary cyclogenesis after the decay of mid-latitude cyclones in this area, as strong westerlies are found in the Atlantic for NAO+[1]. Thus, most of the tracks having genesis in this region could actually be other types of cyclones than PLs.

[1] http://www.metoffice.gov.uk/learning/learn-about-the-weather/north-atlantic-oscillation

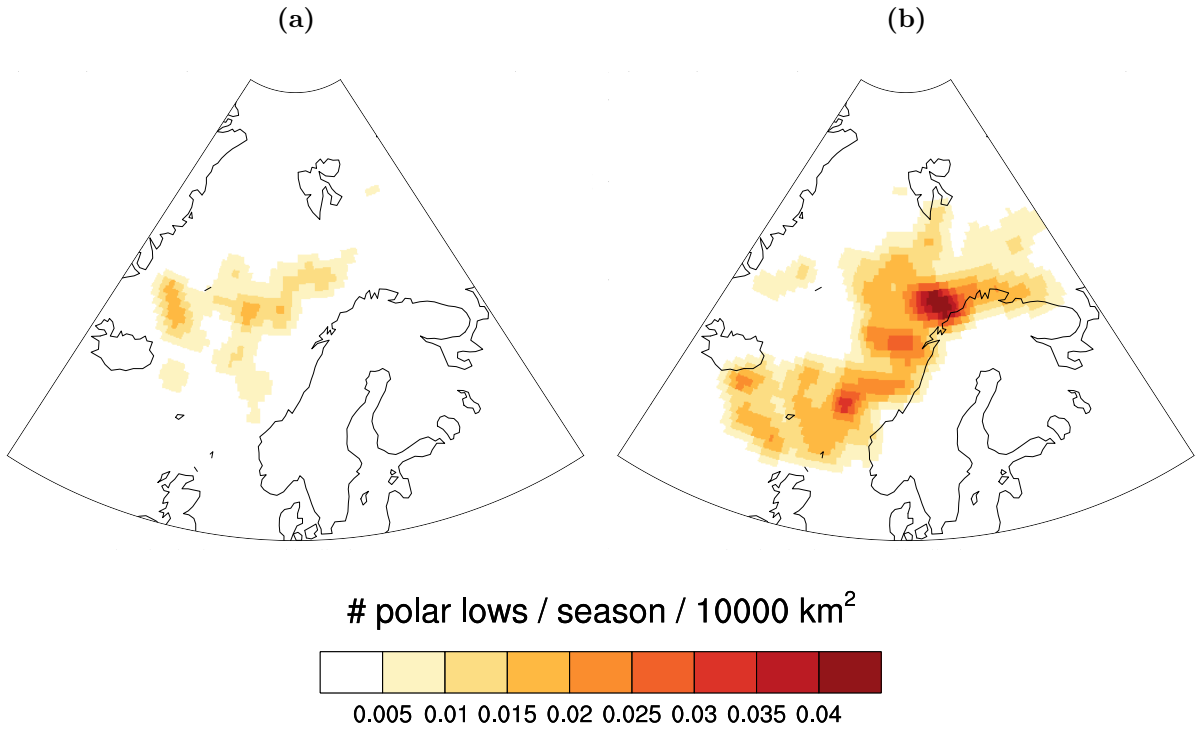

Figure 3.19: Genesis of PLs making landfall in Norway during (a) SB+ and (b) SB- (shading, units: number of PLs per extended winter season per 10000 km^2).

Similarly, Figs. 3.19 and 3.20 display the genesis and landfall, respectively, of the PLs making landfall in Norway for SB+ and SB-. Both Figs. 3.19 and 3.20 reflect the larger numbers for SB- found in Table 3.3 through much larger density than for SB+. The genesis density of the PLs making landfall during SB- is located closer to the coast of Norway than during SB+, which could be explained by less intense anticyclonic circulation over Norway for SB- compared to SB+ (Fig. 1.4), creating a suitable environment for CAOs to reach the coast of Norway. The PLs making landfall in Norway during SB- present a clear maximum around the coast of Trondheim, whereas during SB+, the maximum is located further north, due to the more northerly placement of the genesis density.

Based on the results found above, the atmospheric circulation with the largest impact on PLs reaching Norway is found to be the SB, with the most PL cases during SB- conditions. This is not very surprising, as the SB directly influences the environment at the Norwegian coast through higher or lower pressure than normal, thus inducing more favorable low level winds for CAOs to form during SB-, and less favorable for SB+.

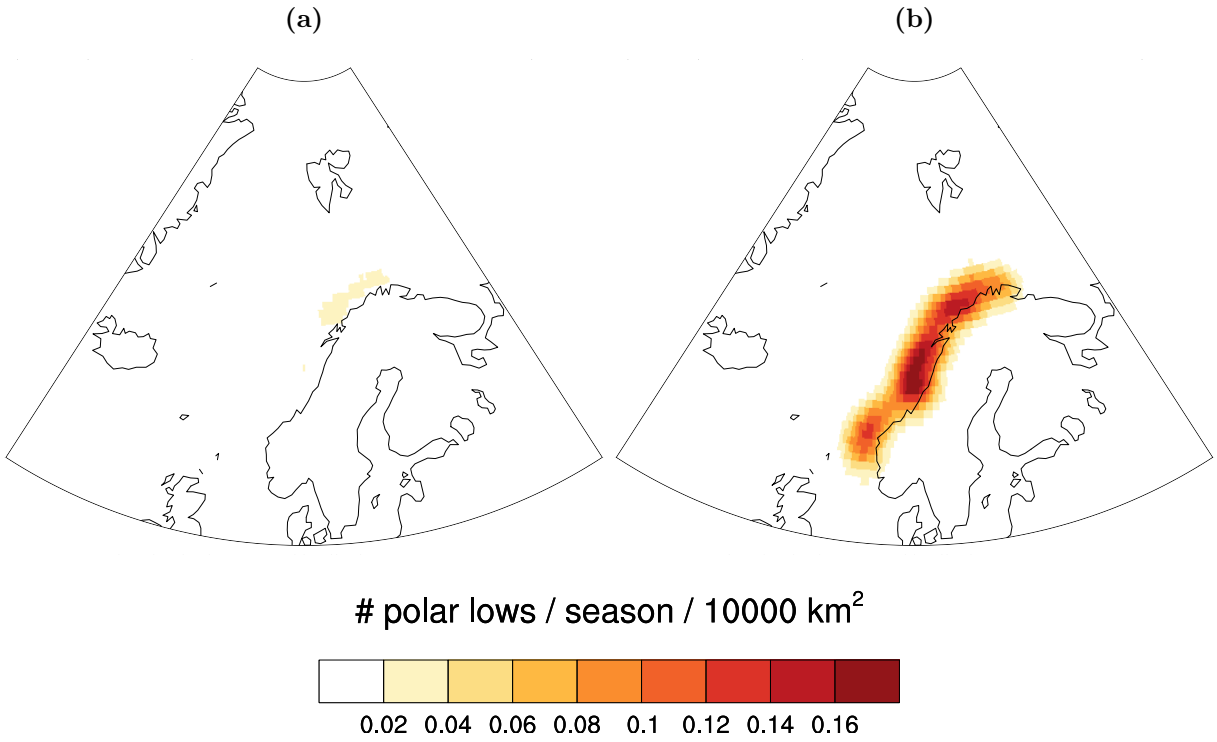

Figure 3.20: PLs making landfall in Norway during (a) SB+ and (b) SB- (shading, units: number of PLs per extended winter season per 10000 km^2).

3.4.3 Correlation between patterns of low-frequency atmospheric variability and shear conditions

As yet, the two patterns of low-frequency atmospheric variability and the two environmental shear conditions have been regarded separately. This section will investigate if there is a correlation between NAO and SB and the angle between the thermal wind and the mean wind for the PLs making landfall in Norway. The *avg*, σ and *corr* values of NAO and SB were again calculated for PLs making landfall in Norway, but this time for the PLs forming in FS and RS environments, with the results shown in Table 3.4.

The averaged NAO index for the PLs forming in a FS (RS) environment is slightly negative (positive). Despite the lack of significance due to the high standard deviations, the values suggest that PL development in FS conditions is more likely during NAO- whereas PL development in RS conditions is more likely during NAO+. These results are in agreement with Fig. 3.14b (c) whose composited anomalies, in FS (RS) conditions, are very similar to the anomaly of NAO- (NAO+) found in Fig. 1.3b (a). The correlation between

Table 3.4: *avg*, σ and *corr* values for the NAO and SB indices, for FS and RS PLs making landfall in Norway.

Index	Shear type	*avg*	σ	*corr*
NAO	FS	-0.23	0.90	-0.41
	RS	0.23	0.84	0.11
SB	FS	-0.19	1.02	-0.19
	RS	-0.65	1.19	-0.53

RS conditions and NAO+ coincides with Kolstad (2006), who stated that RS polar lows occur more often during NAO+ due to more synoptic storm activity in the Norwegian Sea, pulling polar air southward in the region, increasing the chances of polar low development.

Concerning the SB, PLs developing in both FS and RS environments present a negative SB mean index, with a more negative value in the RS case. Again the standard deviations are very high meaning that the results may not be statistically significant. This negative mean index is in agreement with the negative anomalies of 500-hPa geopotential height on Fig 3.14b and c over Scandinavia that correspond to SB- conditions (Fig. 1.4b), with Fig 3.14c being the best fit.

4 Climatology of polar lows for future climate scenarios

An investigation of the change of PL distribution in the future has been made by applying the Melbourne detection and tracking algorithm to data from the GFDL models HiRAM c180 and HiRAM c360. The distribution of PLs in the future can change due to several effects, the most obvious one being that the Arctic sea ice retreats northwards due to global warming, thus making the CAOs shift northwards (Zahn and von Storch, 2008; Kolstad and Bracegirdle, 2008). The North Atlantic ocean is predicted to experience moderate warming compared to the tropospheric air temperature, thus leading to increased vertical stability and less favorable conditions for PL development (Zahn and von Storch, 2008). The results found in this chapter will be compared to Zahn and von Storch (2008), who found a decrease of PLs up to 50% for the period 2070-2099 along with a 2° latitude northward shift in genesis density, and to Kolstad and Bracegirdle (2008) who found a northward shift of CAOs.

4.1 Comparison of ERAI and GFDL HiRAM models

The control runs for the period 1979-2009 were compared to the ERAI runs for the period 1979-2015 (Table 4.1), to see if the models behaved in a similar fashion. Table 4.1 shows that both HiRAM models pick up less PLs than ERAI, which has as much as three times more PLs for the Nordic seas. This could be a result of several effects, one being that ERAI uses data assimilation every 6 hours whereas the HiRAM models run freely without injection of observations via data assimilation and are only fed with boundary conditions.

Table 4.1: Numbers of PLs making landfall in Norway, reaching fisheries, oil platforms and the Nordic seas for ERAI and for the models HiRAM c180 and HiRAM c360, both for the full periods and per extended winter season. The number of PLs for the HiRAM models are not integers because of the averaging over the different runs.

Area	Model	Number of PLs	Pls/season
Nordic seas	ERAI (1979-2015)	6747	187.4
	HiRAM c180 (1979-2009)	1918.3	63.9
	HiRAM c360 (1979-2009)	1921.5	64.0
Norway	ERAI (1979-2015	560	15.6
	HiRAM c180 (1979-2009)	285.0	9.5
	HiRAM c360 (1979-2009)	292.5	9.7
Fisheries	ERAI (1979-2015)	2458	68.3
	HiRAM c180 (1979-2009)	941.3	31.4
	HiRAM c360 (1979-2009)	954.5	31.8
Oil platforms	ERAI (1979-2015)	1515	42.1
	HiRAM c180 (1979-2009)	551.3	18.4
	HiRAM c360 (1979-2009)	551.0	18.4

The areas of PL density for ERAI and the GFDL models are quite similar, which is illustrated in Fig. 4.1 and Fig. 4.2, showing the track density in the Nordic seas and the density of PLs making landfall in Norway, respectively, for HiRAM c180, HiRAM c360 and ERAI. The larger density for ERAI is easily identified, both reflected in the track density in the Nordic seas and the PLs making landfall in Norway. Both the track density and the density of PLs making landfall in Norway are similarly distributed for the three different models, though with slightly different track density patterns for the two HiRAM models compared to ERAI, and less PLs are found to make landfall at the northernmost part of Norway for both HiRAM models. The results for HiRAM c180 and HiRAM c360 are almost identical, indicating that the resolution increase in HiRAM c360 does not appear to have a significant impact on the results.

Similar comparisons are found when investigating Fig. 4.3 and Fig. 4.4, showing the PLs reaching fisheries and oil platforms, respectively, for HiRAM c180, HiRAM c360 and ERAI, with larger density for ERAI, and the densities from the two HiRAM models looking almost identical.

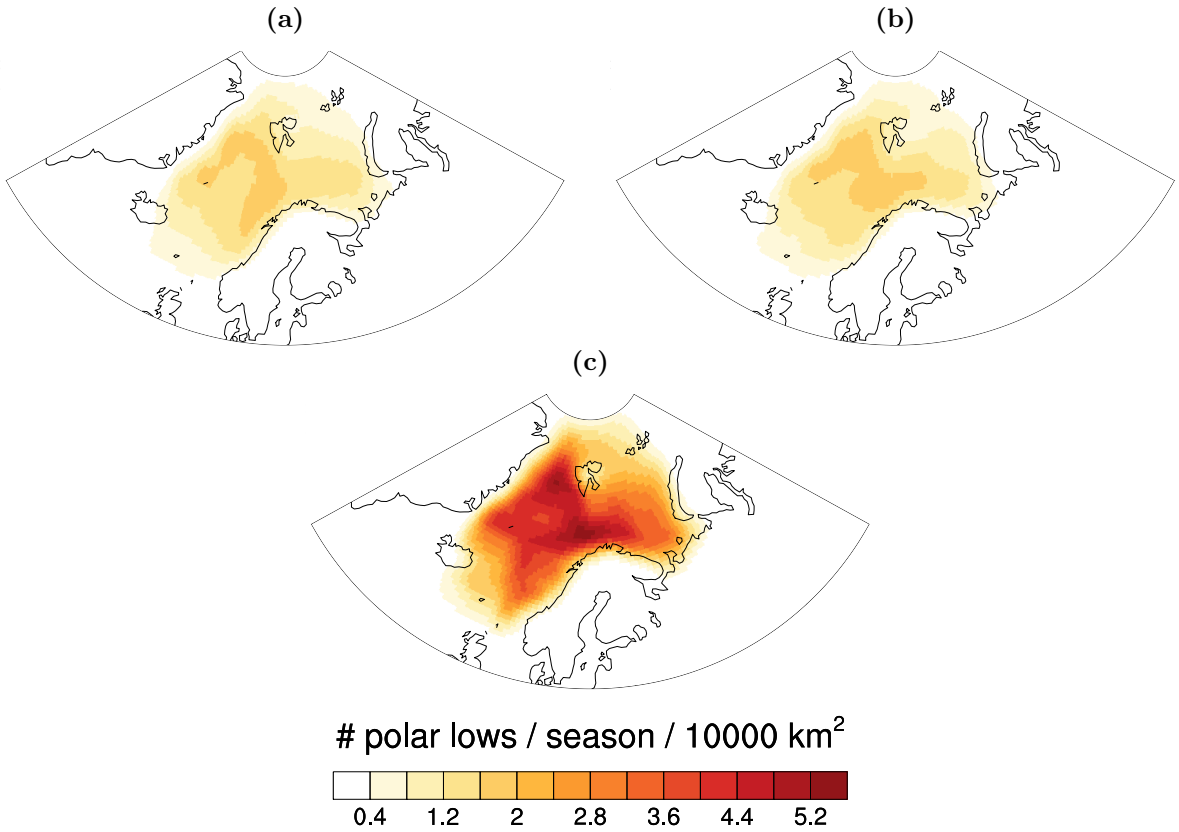

Figure 4.1: Comparison of track density in the Nordic seas for (a) HiRAM c180, (b) HiRAM c360, and (c) ERAI (shading, units: number of PLs per extended winter season per 10000 km^2).

4.2 Future climate analysis

Presented next is a comparison of the numbers and densities of PLs for the different periods for the HiRAM c180 and HiRAM c360 models, both in the RCP4.5 and RCP8.5 future climate scenarios, to see if a change of PL activity in the future is to be expected.

4.2.1 HiRAM c180

The future climate analysis will first be made utilizing HiRAM c180, which has the lowest resolution of the two HiRAM models, but includes runs for RCP4.5 in the period 2026-2035, not included in HiRAM c360.

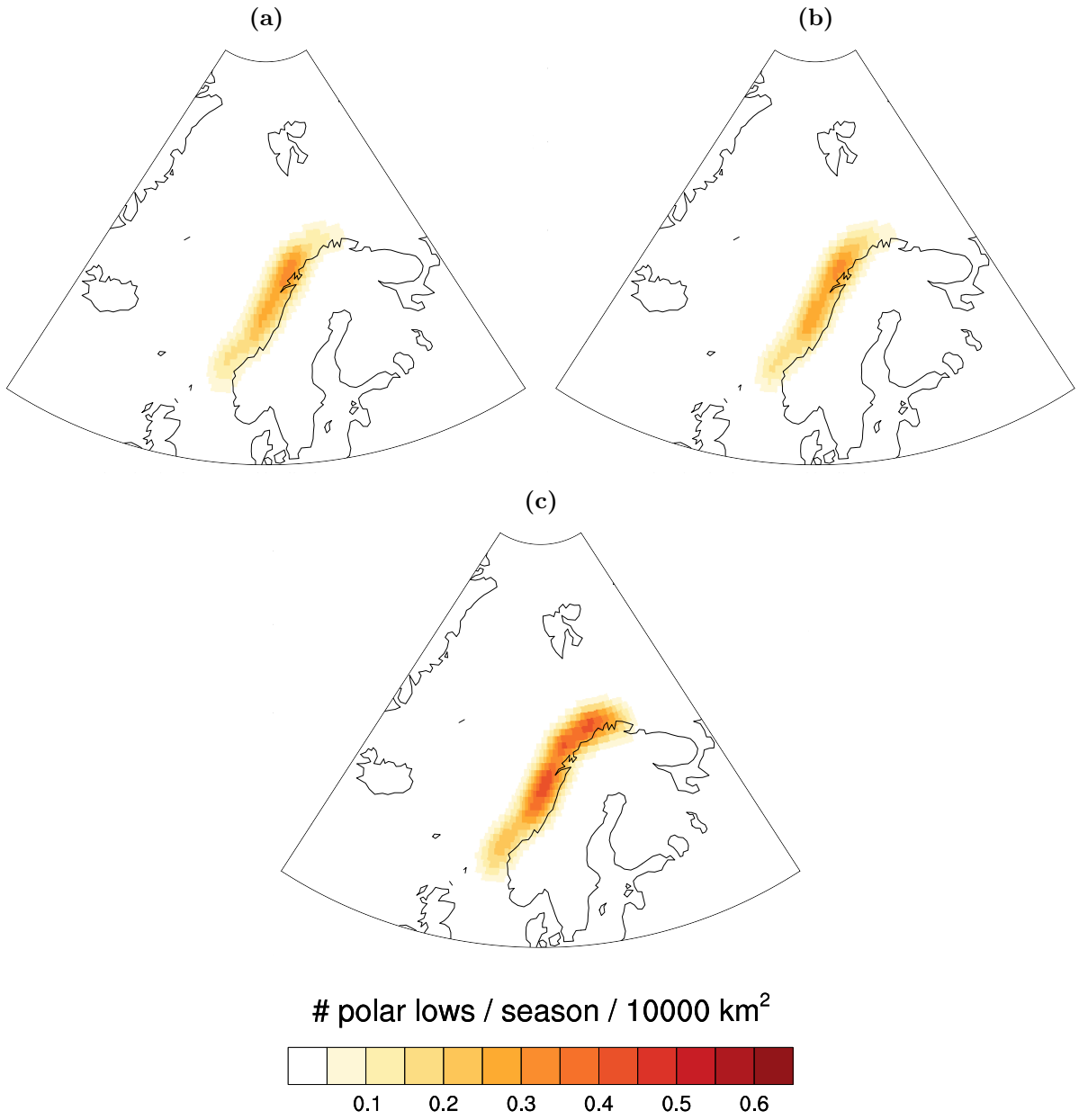

Figure 4.2: Comparison of PLs making landfall in Norway for (a) HiRAM c180, (b) HiRAM c360, and (c) ERAI (shading, units: number of PLs per extended winter season per 10000 km^2).

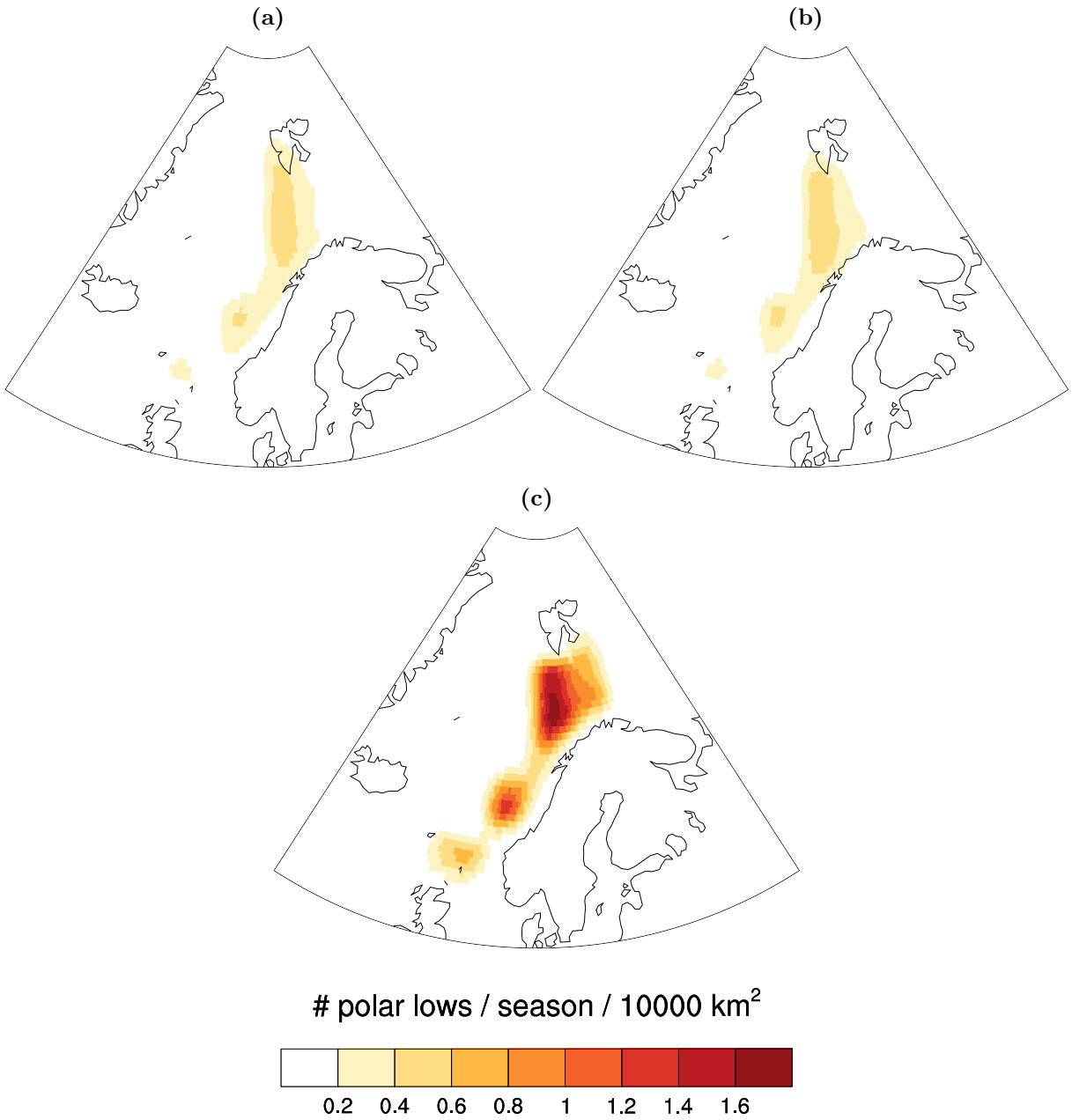

Figure 4.3: Comparison of PLs reaching fisheries for (a) HiRAM c180, (b) HiRAM c360, and (c) ERAI (shading, units: number of PLs per extended winter season per 10000 km^2).

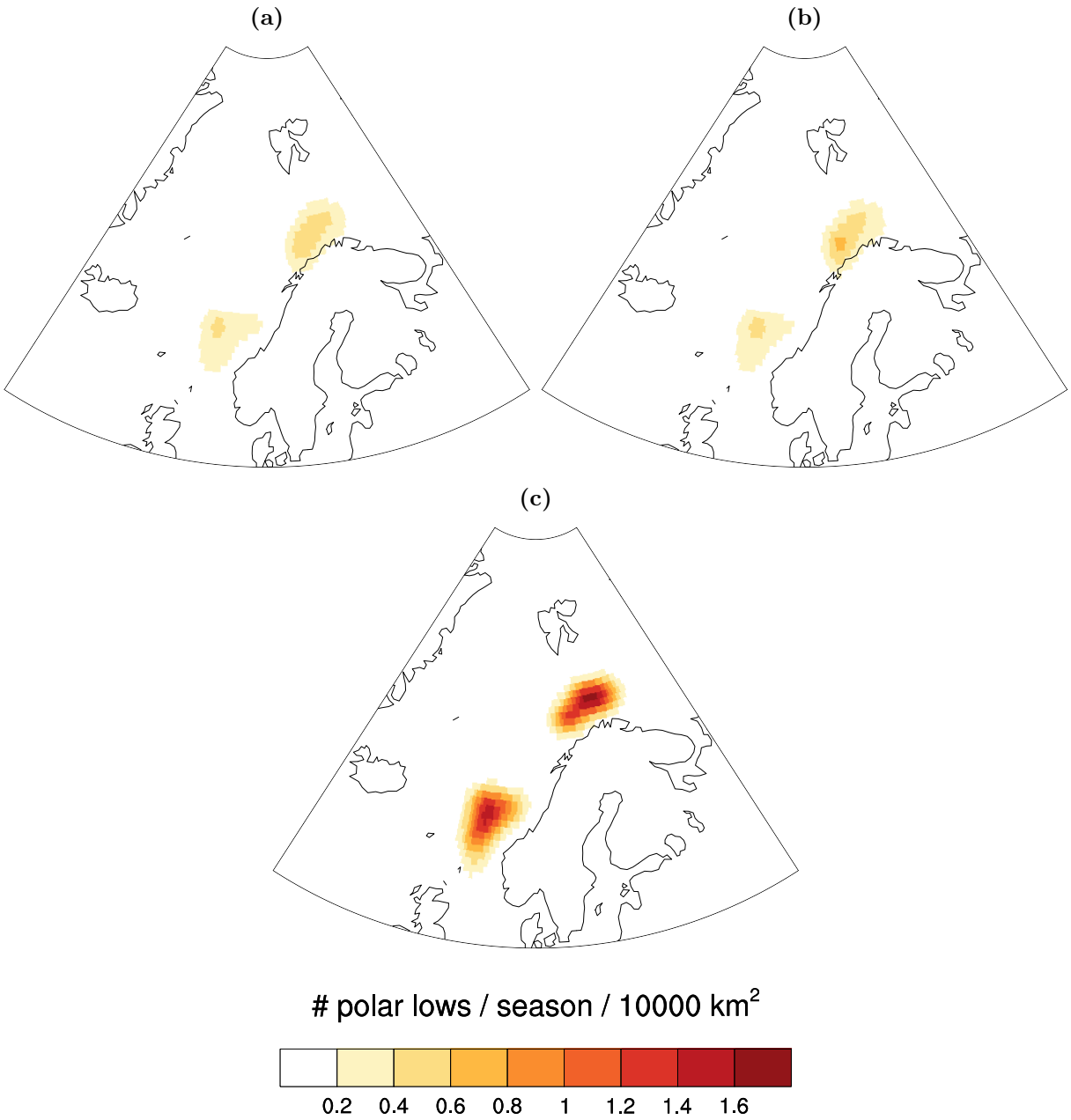

Figure 4.4: Comparison of PLs reaching oil platfomrs for (a) HiRAM c180, (b) HiRAM c360 and (c) ERAI (shading, units: number of PLs per extended winter season per 10000 km^2).

RCP4.5

First, the focus will be on RCP4.5, which is the future climate with the least anthropogenic climate forcing. Table 4.2 shows the numbers of PLs for the different periods, with boundary conditions provided by CM3 and ESM2M, for the HiRAM c180 model in the RCP4.5 future climate scenario. It is evident that the number of PLs per extended winter in the Nordic seas is decreasing for the future periods compared to the historical runs, with a decrease of around 12% for the period 2026-2035 with both CM3 and ESM2M boundary conditions. The decrease from the 2026-2035 period to the 2086-2095 period is quite small, to a value of around 15% with boundary conditions from both CM3 and ESM2M.

Table 4.2: Numbers of PLs per extended winter season making landfall in Norway, and reaching the Nordic seas, fisheries and oil platforms for the model HiRAM c180, for the two different periods, for the future climate scenario RCP4.5 with both CM3 and ESM2M boundary conditions.

Area	Boundary conditions	Period	Pls/season
Nordic seas	HiRAM	1979-2009	63.9
	CM3	2026-2035	55.8
	CM3	2086-2095	54.6
	ESM2M	2026-2035	56.6
	ESM2M	2086-2095	54.5
Norway	HiRAM	1979-2009	9.5
	CM3	2026-2035	10.4
	CM3	2086-2095	9.4
	ESM2M	2026-2035	8.6
	ESM2M	2086-2095	8.7
Fisheries	HiRAM	1979-2009	31.4
	CM3	2026-2035	31.2
	CM3	2086-2095	29.4
	ESM2M	2026-2035	30.4
	ESM2M	2086-2095	29.5
Oil platforms	HiRAM	1979-2009	18.4
	CM3	2026-2035	18.0
	CM3	2086-2095	17.3
	ESM2M	2026-2035	17.0
	ESM2M	2086-2095	17.4

The decrease of PLs making landfall in Norway is less prominent than for the Nordic seas, and there is actually an increase when using CM3 boundary conditions for the period 2026-2035. Similar trends are found for both PLs reaching fisheries and oil platforms, with less decrease of PLs than for the Nordic seas.

Composites of the SST and sea ice for the extended winter months are made, for CM3 and ESM2M for both future periods with the control runs as a reference (Fig. 4.5). Figure 4.5 shows that higher SSTs and a corresponding more northward positioned sea ice edge are found for CM3 compared to ESM2M for both periods, due to different SST and

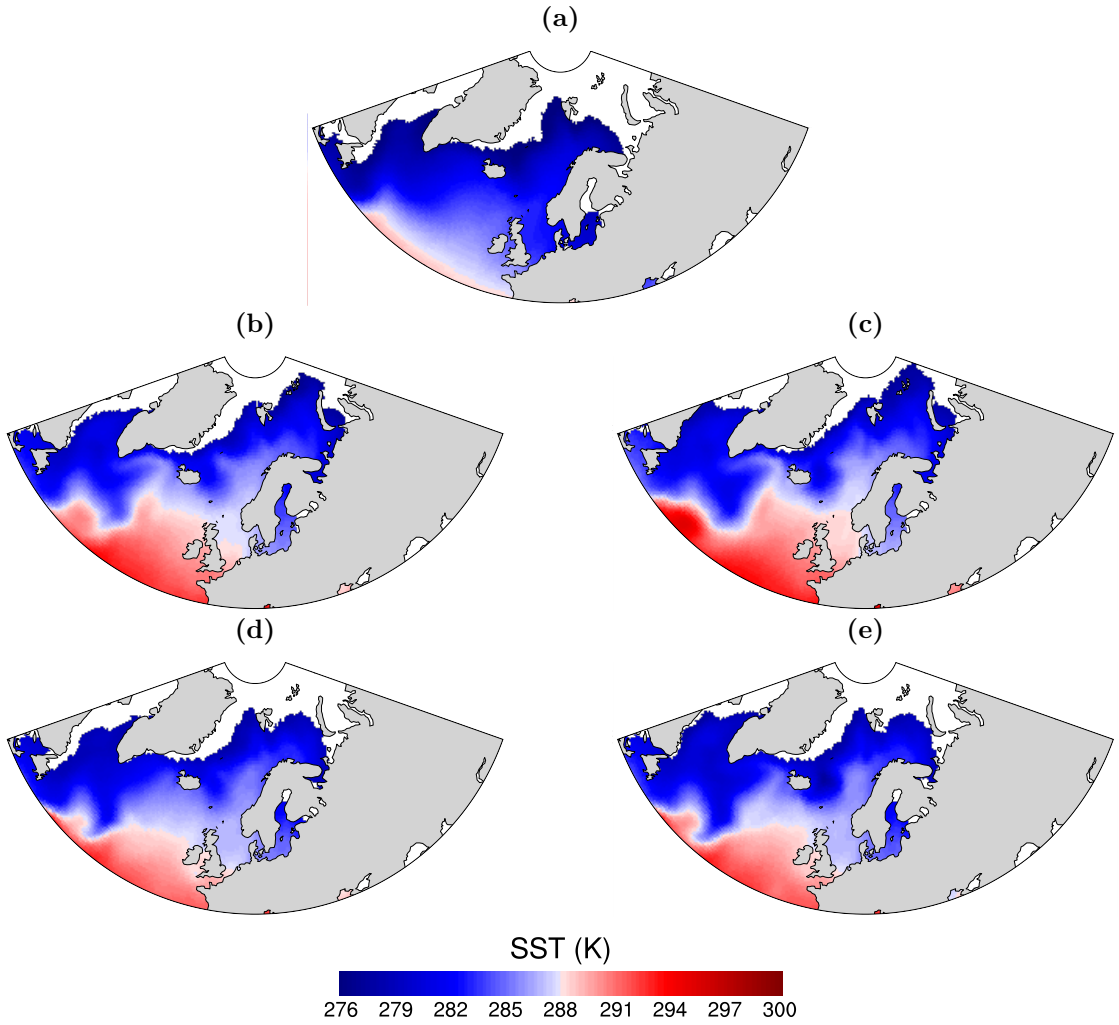

Figure 4.5: Composites of HiRAM c180 SST (shading, units: K) and sea ice (white shading) for (a) control run, and for the climate scenario RCP4.5 for the period and with the boundary conditions (b) 2026-2035 CM3, (c) 2086-2095 CM3, (d) 2026-2035 ESM2M, and (e) 2086-2095 ESM2M.

sea ice dynamics in the two models. The sea ice edge shows no evident northward shift from 2026-2035 to 2086-2095 for ESM2M, as it does for CM3.

Comparisons of the track densities in the Nordic seas are made between the control runs from the period 1979-2009 (Fig. 4.1a), utilized as a reference, and the runs with boundary conditions provided by CM3 and ESM2M for the periods 2026-2035 and 2086-2095. Figure 4.6 shows the deviations from the control runs for the 4 different periods and boundary condition combinations. It is evident that there are some differences in track density between the CM3 and ESM2M runs.

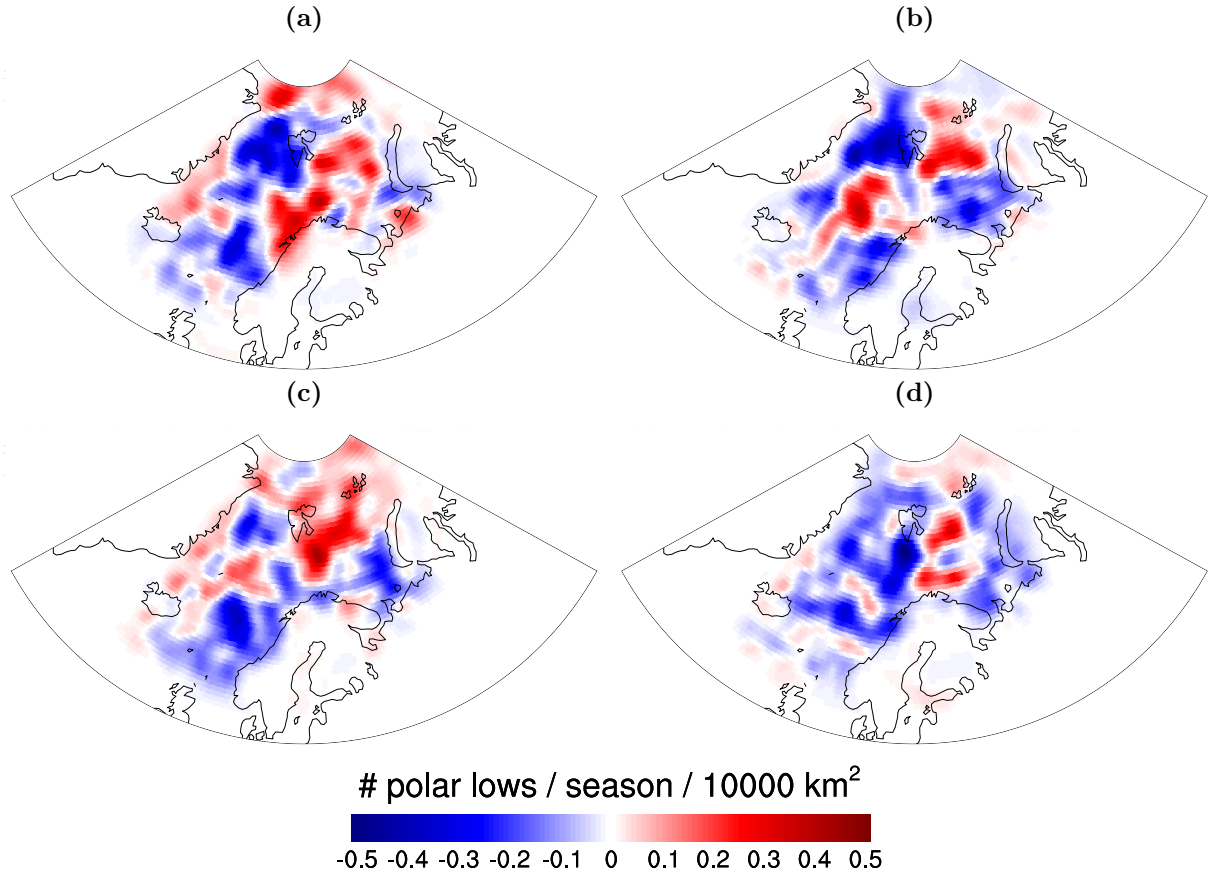

Figure 4.6: Deviation of track density from control runs for HiRAM c180 in the climate scenario RCP4.5 for the period and with the boundary conditions (a) 2026-2035 CM3, (b) 2086-2095 CM3, (c) 2026-2035 ESM2M, and (d) 2086-2095 ESM2M (shading, units: number of PLs per extended winter season per 10000 km^2). Blue colors indicate a decrease in track density and red colors indicate an increase in track density.

Figure 4.6a shows an increase in track density for CM3 for the period 2026-2035 at the northernmost latitudes, around the coast of Norway and in the Barents Sea, whereas a decrease in track density is found in the area extending from Svalbard westwards to Greenland. The decrease in track density in the Svalbard region can be explained by the northward shift of sea ice found in Fig. 4.5b, causing a more northerly positioned CAO region, and a corresponding increase in track density in higher latitudes. The increase in track density in the Barents Sea occurs in spite of a northward shift of the sea ice edge. However, increased SST could lead to more intense CAOs because of a larger temperature gradient between the air and the ocean in the Barents Sea.

When investigating the period 2086-2095 with boundary conditions provided by CM3 (Fig. 4.6b), a decrease in track density is evident west and north of Svalbard, due to a further northward shift of the sea ice edge (Fig. 4.5c). The Barents Sea also shows a reduction in track density, which could be due to the sea ice edge being too far away to produce as many CAOs as before. An increase in track density is found east-northeast of Svalbard instead. An increase in track density is also found southwest of Svalbard, possibly due to higher SST in the area, increasing the number of CAOs from Svalbard and Greenland.

For the runs with boundary conditions provided by ESM2M for the period 2026-2035 (Fig. 4.6c), the most pronounced feature is the increase of track density south and east of Svalbard. This could be explained by higher SST in the area, and just a small northward shift of the sea ice edge (Fig. 4.5d), leading to favorable conditions for PL development. This feature is however less prominent for the period 2086-2095 shown in Fig. 4.6d.

Next, the impact on Norway for the climate scenario RCP4.5 is investigated further by plotting the deviation from the control runs (Fig. 4.2a) of PLs making landfall in Norway for the 4 different periods and boundary condition combinations (Fig. 4.7). For the runs with boundary conditions provided by CM3 for the period 2026-2035 (Fig. 4.7a), there is an increase in the total number of PLs making landfall in Norway (Table 4.2). The maximum increase is found at the coast of middle Norway, possibly due to higher SST in this region (Fig. 4.5). As for CM3 for the period 2086-2095, approximately the same number of PLs reaches Norway as for the control runs. The decrease in PL activity compared to the 2026-2035 period can be explained by a further northward shift of the sea ice edge, and a corresponding decrease in track density found outside the coast of Norway (Fig. 4.6b).

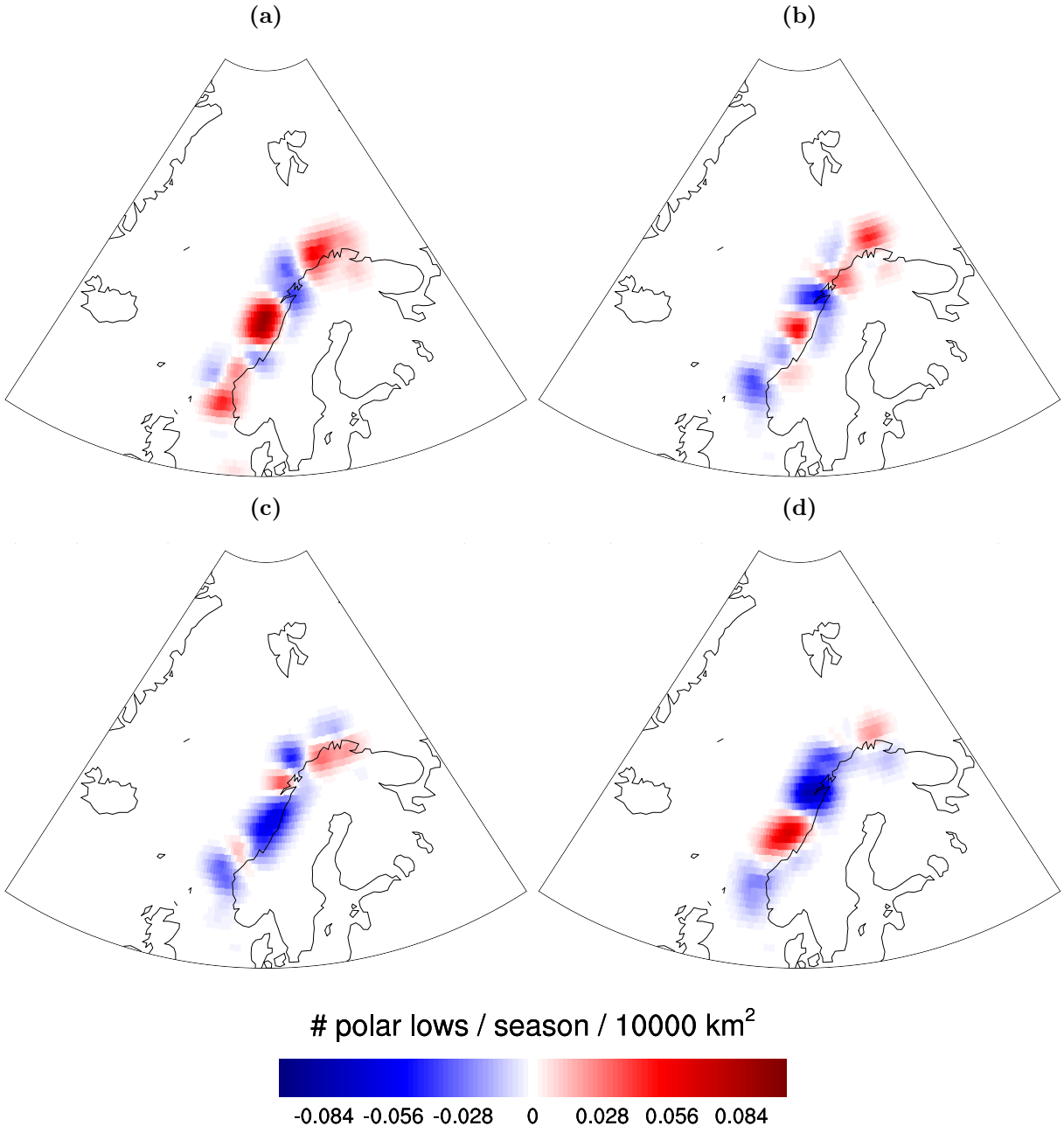

Figure 4.7: Deviation of PLs making landfall in Norway from control runs for HiRAM c180 in the climate scenario RCP4.5 for the period and with the boundary conditions (a) 2026-2035 CM3, (b) 2086-2095 CM3, (c) 2026-2035 ESM2M, and (d) 2086-2095 ESM2M (shading, units: number of PLs per extended winter season per 10000 km^2). Blue colors indicate a decrease in track density and red colors indicate an increase in track density.

Figures 4.7c and d show the deviation of ESM2M from the control runs for the periods 2026-2035 and 2086-2095 of the PLs making landfall in Norway. A more evident decline of PLs making landfall in Norway is found compared to CM3, reflecting the numbers from Table 4.2.

For completeness, the deviation from the control runs of the PLs reaching fisheries and oil platforms were plotted, and are shown in Fig. 4.8 and Fig. 4.9, respectively. It is evident that Fig. 4.8 and Fig. 4.9 reflect the numbers of Table 4.2, with a larger decrease in density of PLs for CM3 compared to ESM2M. The reasons for positive and negative deviations from the control runs in the different locations remain the same as for Fig. 4.6.

RCP 8.5

Next, the focus is on RCP 8.5, where anthropogenic climate forcing rises linearly throughout the 21st century. Table 4.3 shows the numbers of PLs for the period 2086-2095 with boundary conditions provided by CM3 and ESM2M, for the HiRAM c180 model in the RCP8.5 future climate scenario, with the control runs as a reference. The decrease in PLs in the Nordic seas is larger than for RCP4.5 (Table 4.2), with a 20.7% decrease for CM3 and a 17.1% decrease for ESM2M for the period 2086-2095. The decrease is not as large for PLs making landfall in Norway and PLs reaching fisheries and oil platforms.

Table 4.3: Numbers of PLs per season making landfall in Norway, and reaching the Nordic seas, fisheries and oil platforms for the model HiRAM c180 for the period 2086-2095, for the future climate scenario RCP8.5 with both CM3 and ESM2M boundary conditions, with the control runs as a reference.

Area	Boundary conditions	Period	Pls/season
Nordic seas	HiRAM	1979-2009	63.9
	CM3	2086-2095	50.7
	ESM2M	2086-2095	53.0
Norway	HiRAM	1979-2009	9.5
	CM3	2086-2095	8.7
	ESM2M	2086-2095	8.0
Fisheries	HiRAM	1979-2009	31.4
	CM3	2086-2095	27.7
	ESM2M	2086-2095	29.4
Oil platforms	HiRAM	1979-2009	18.4
	CM3	2086-2095	16.0
	ESM2M	2086-2095	16.8

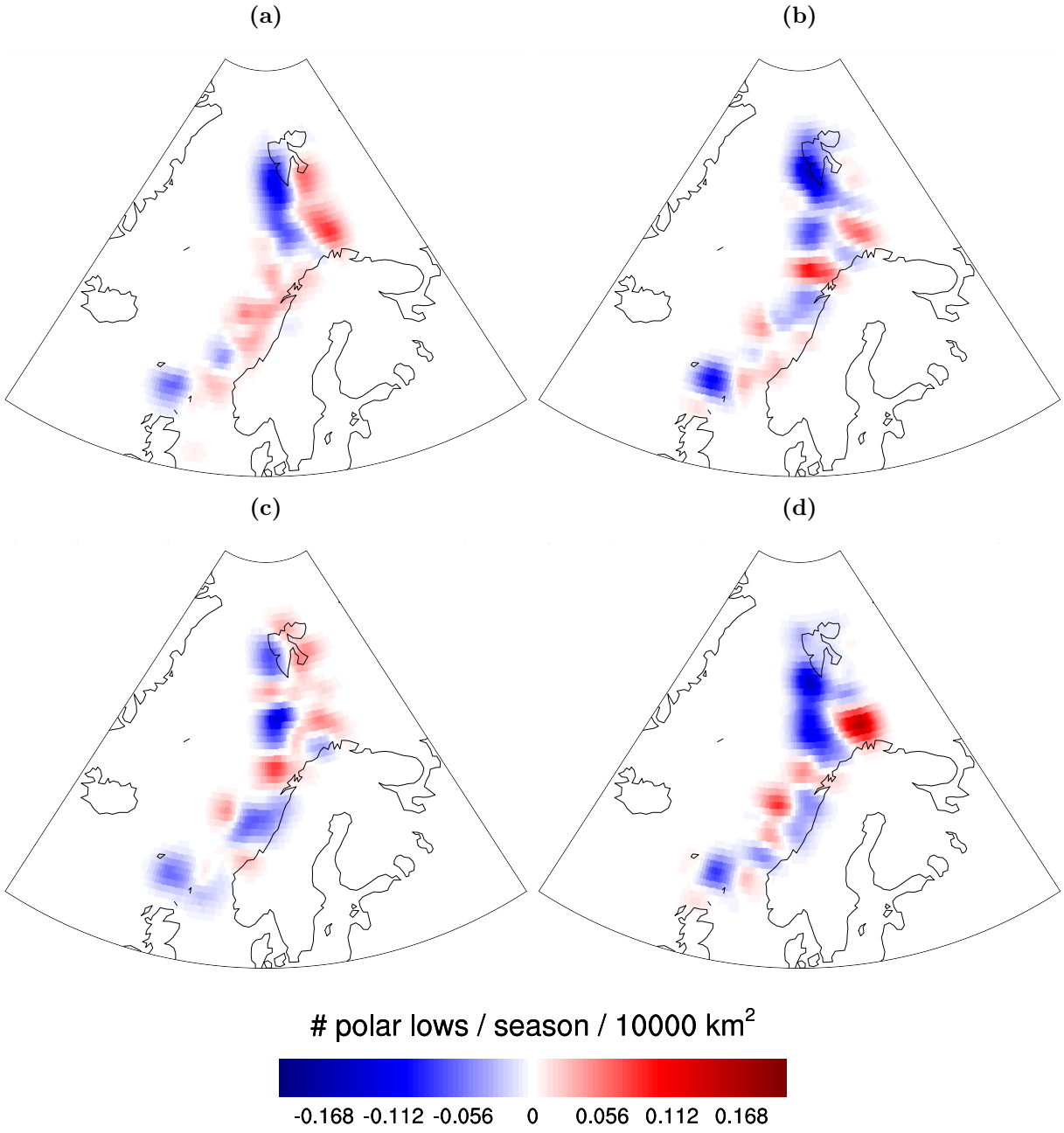

Figure 4.8: Deviation of PLs reaching fisheries from control runs for HiRAM c180 in the climate scenario RCP4.5 for the period and with the boundary conditions (a) 2026-2035 CM3, (b) 2086-2095 CM3, (c) 2026-2035 ESM2M, and (d) 2086-2095 ESM2M (shading, units: number of PLs per extended winter season per 10000 km^2). Blue colors indicate a decrease in track density and red colors indicate an increase in track density.

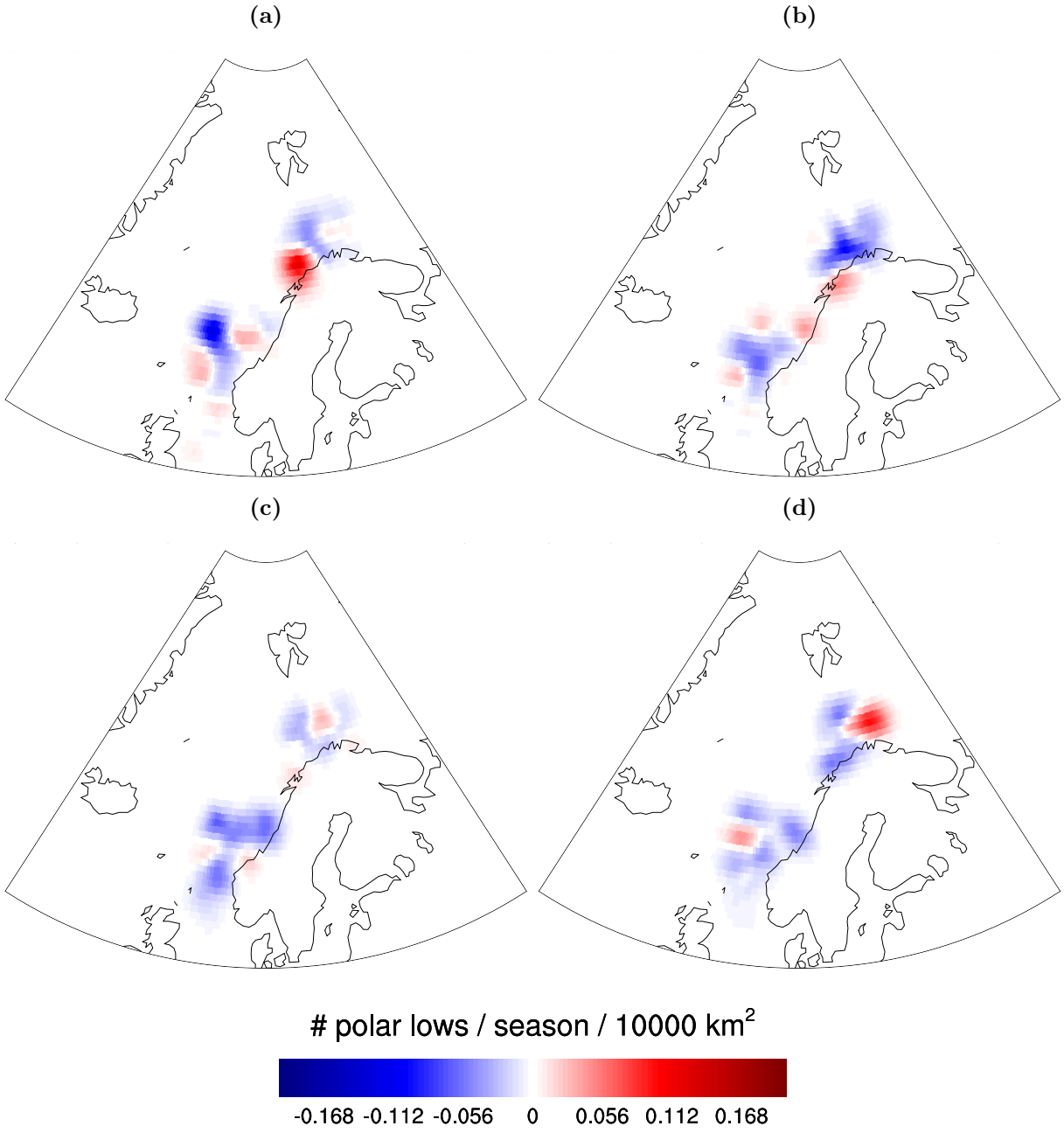

Figure 4.9: Deviation of PLs reaching oil platforms from control runs for HiRAM c180 in the climate scenario RCP4.5 for the period and with the boundary conditions (a) 2026-2035 CM3, (b) 2086-2095 CM3, (c) 2026-2035 ESM2M, and (d) 2086-2095 ESM2M (shading, units: number of PLs per extended winter season per 10000 km^2). Blue colors indicate a decrease in track density and red colors indicate an increase in track density.

Figure 4.10 shows the composites of SST and sea ice for the period 2086-2095, with boundary conditions provided by CM3 and ESM2M, and the control runs as a reference. The differences in sea ice extent between CM3 and ESM2M are large, with almost no sea ice left for CM3, as well as a generally higher SST value for CM3 compared to ESM2M.

Figure 4.11 shows the deviations in track density from the control runs for RCP8.5 for the period 2086-2095 with boundary conditions provided by both CM3 and ESM2M. Both the track density with boundary conditions from CM3 and ESM2M show a decrease for most of the Nordic seas, with the exception of areas southwest of Svalbard, east of Svalbard and along the eastern coast of Greenland. The patterns of track density for CM3 and ESM2M are very similar, even though the SST is larger and the sea ice edge is positioned much further north for CM3 compared to ESM2M (Fig. 4.10).

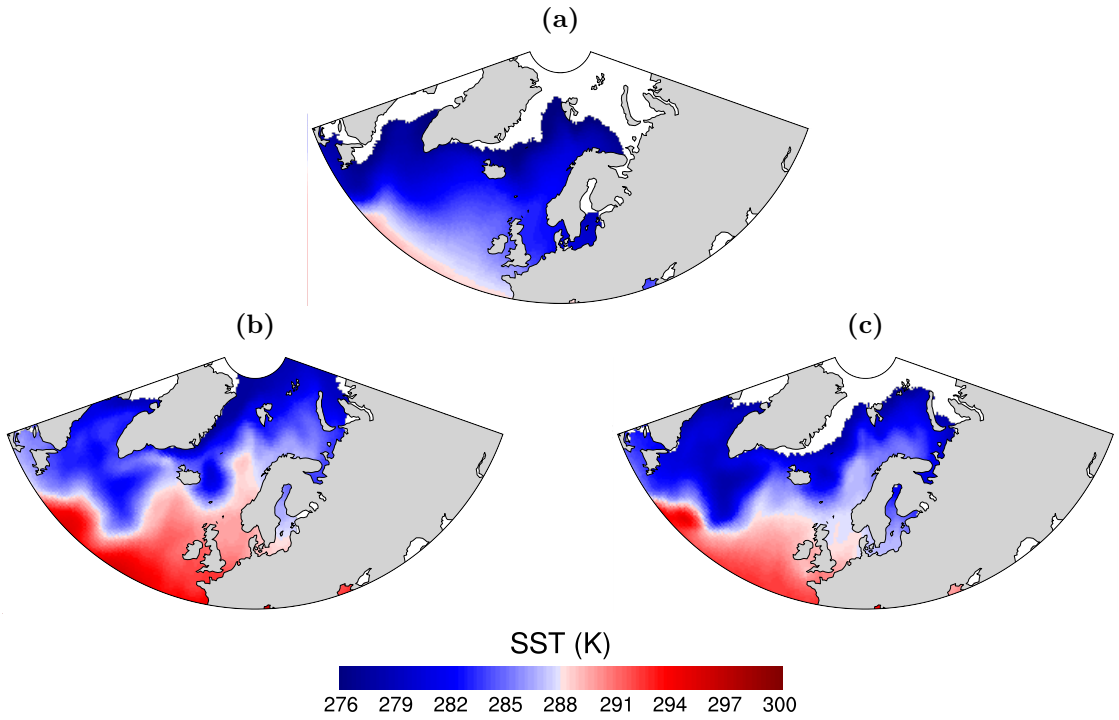

Figure 4.10: Composites of HiRAM c180 SST (shading, units: K) and sea ice (white shading) for (a) control run, and for the climate scenario RCP8.5 for the period and with the boundary conditions (b) 2086-2095 CM3, and (c) 2086-2095 ESM2M.

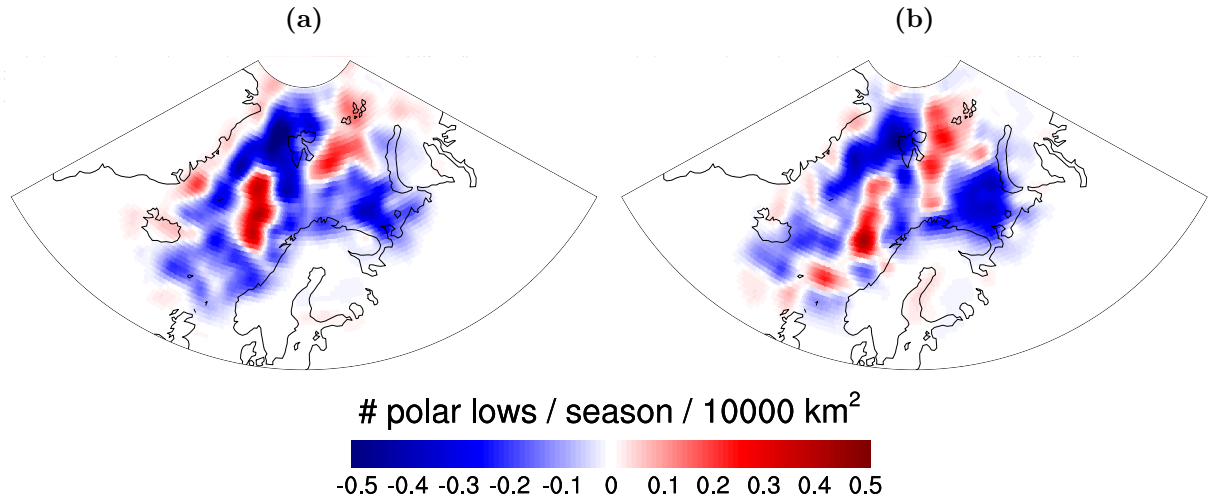

Figure 4.11: Deviation of track density from control runs for HiRAM c180 in the climate scenario RCP8.5 for the period 2086-2095 with boundary conditions provided by (a) CM3 and (b) ESM2M (shading, units: number of PLs per extended winter season per 10000 km^2). Blue colors indicate a decrease in track density and red colors indicate an increase in track density.

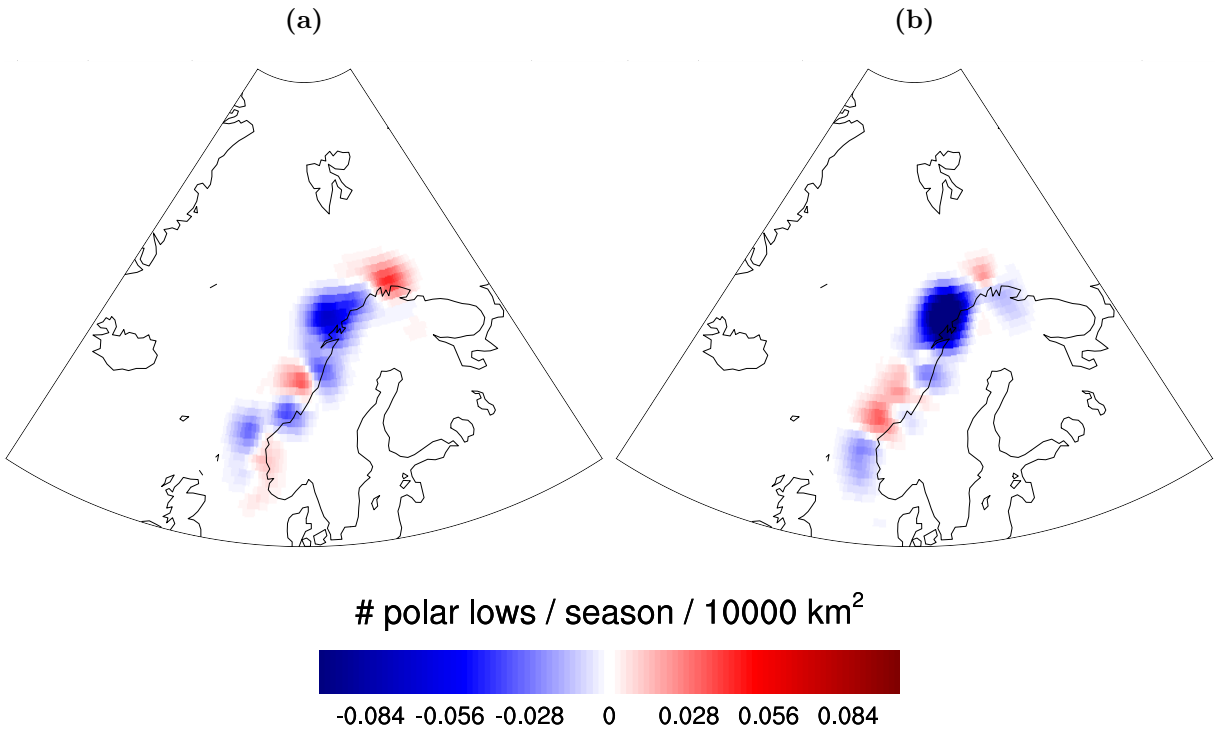

Figure 4.12: Deviation of PLs making landfall in Norway from control runs for HiRAM c180 in the climate scenario RCP8.5 for the period 2086-2095 with boundary conditions provided by (a) CM3 and (b) ESM2M (shading, units: number of PLs per extended winter season per 10000 km^2). Blue colors indicate a decrease in track density and red colors indicate an increase in track density.

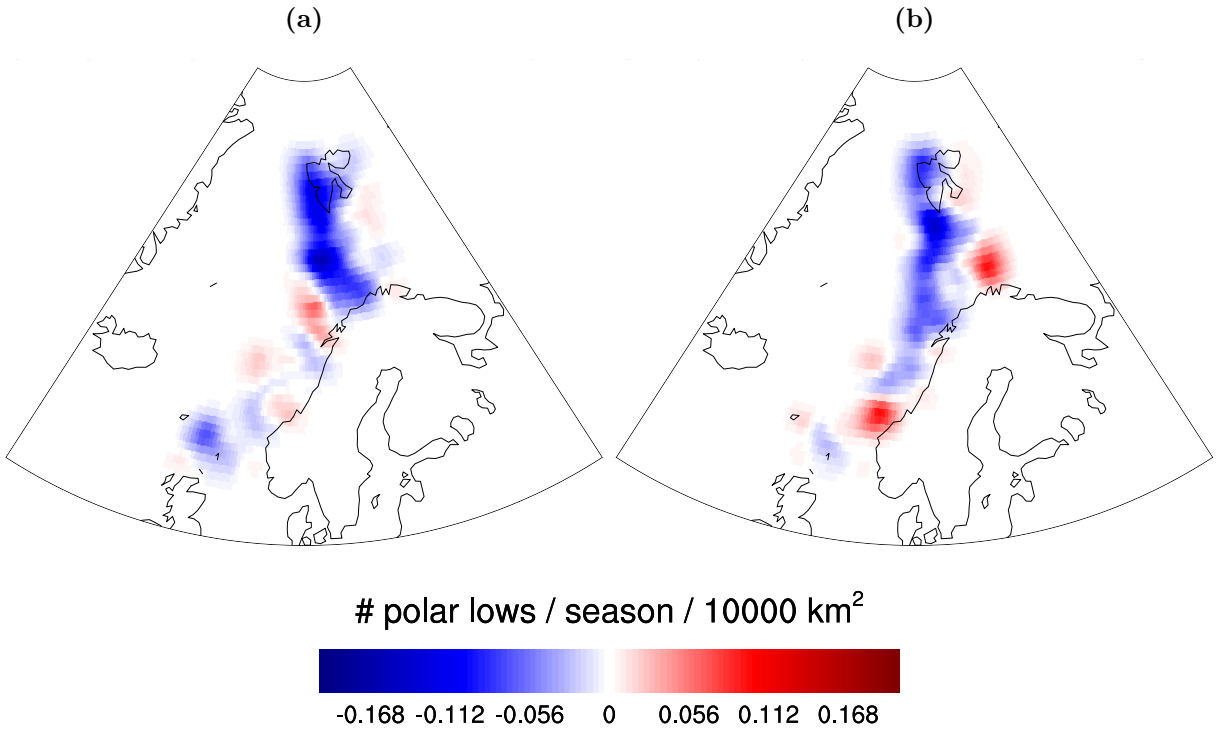

Figure 4.13: Deviation of PLs reaching fisheries from control runs for HiRAM c180 in the climate scenario RCP8.5 for the period 2086-2095 and boundary conditions provided by (a) CM3 and (b) ESM2M (shading, units: number of PLs per extended winter season per 10000 km^2). Blue colors indicate a decrease in track density and red colors indicate an increase in track density.

Figures 4.12, 4.13 and 4.14 show the deviations for density of PLs making landfall in Norway, reaching fisheries and oil platforms, respectively. Both CM3 and ESM2M show a decrease in PLs making landfall in Norway compared to the control runs, with the maximum decrease at the northern coast. This can be explained by a general decrease of track density in the Nordic seas, reducing the number of PLs making landfall in Norway. A general decrease is evident for PLs reaching fisheries and oil platforms.

4.2.2 HiRAM c360

Results for the PLs in the Nordic seas for future climate scenarios were also produced utilizing the high resolution HiRAM c360 model. The SST and sea ice were almost identical as for HiRAM c180, therefore Figs. 4.5 and 4.10 will still be utilized as references of SST and sea ice for RCP4.5 and RCP8.5, respectively.

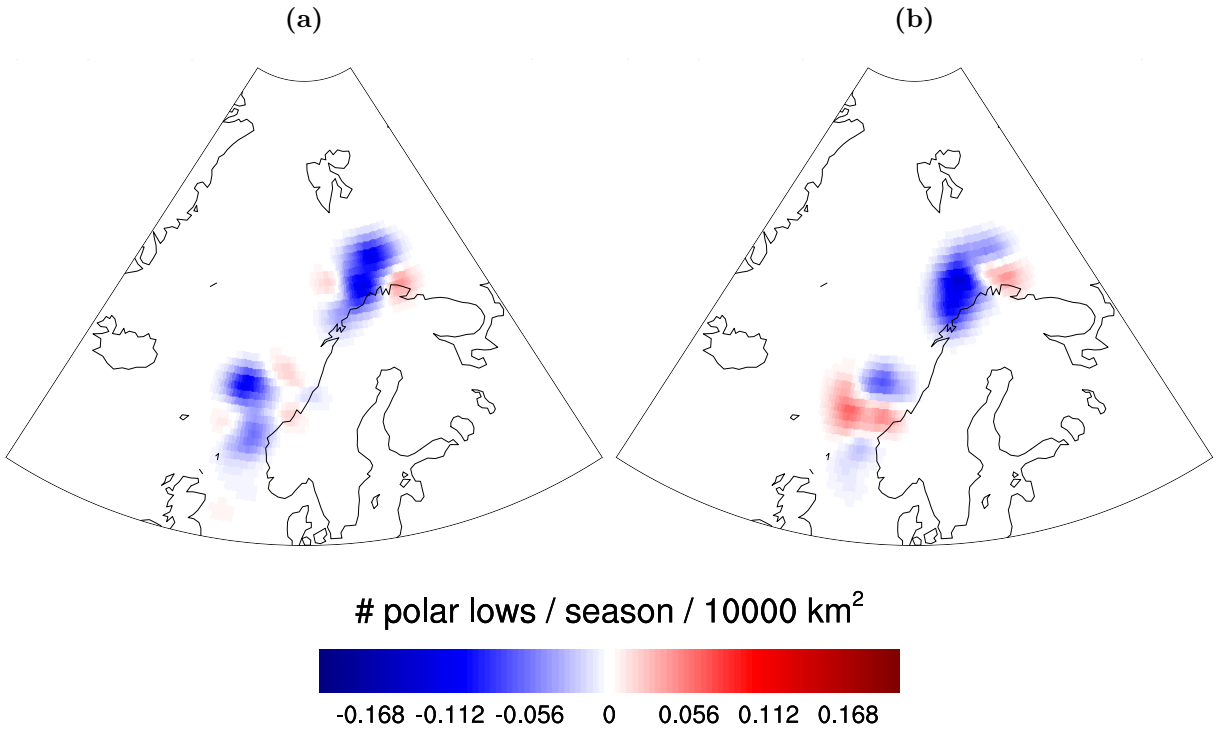

Figure 4.14: Deviation of PLs reaching oil platforms from control runs for HiRAM c180 in the climate scenario RCP8.5 for the period 2086-2095 and boundary conditions provided by (a) CM3 and (b) ESM2M (shading, units: number of PLs per extended winter season per 10000 km^2). Blue colors indicate a decrease in track density and red colors indicate an increase in track density.

RCP 4.5

Table 4.4 shows the numbers of PLs for the period 2026-2035, with boundary conditions provided by CM3 and ESM2M, for the HiRAM c360 model in the RCP4.5 future climate scenario, with the control runs as a reference. It is evident from Table 4.4 that the numbers are very similar as for the c180 model (Table 4.2), implying that the higher resolution model might not be able to pick up anything different than the lower resolution model.

However, when investigating the density distributions, some contrasting behavior can be found. Figure 4.15 shows the track density of PLs in the Nordic seas for the climate scenario RCP4.5 for the period 2026-2035, evidently showing an increase in track density compared to the control runs east of Iceland, both for CM3 and ESM2M. As well, a decrease in track density is found north of Svalbard both for CM3 and ESM2M, in contrast to what was found for HiRAM c180 (Fig. 4.6). Otherwise, the track density patterns in Fig. 4.15 show some of the same behavior as for HiRAM c180 (Fig. 4.6), with an increase in PL activity east of Svalbard and at the eastern coast of Greenland for both CM3 and ESM2M.

Table 4.4: Numbers of PLs per season making landfall in Norway, and reaching the Nordic seas, fisheries and oil platforms for the model HiRAM c360, for the period 2026-2035 with different boundary conditions. Control runs are utilized as a reference.

Area	Boundary conditions	Period	Pls/season
Nordic seas	HiRAM	1979-2009	64.0
	CM3	2026-2035	60.5
	ESM2M	2026-2035	58.8
Norway	HiRAM	1979-2009	9.8
	CM3	2026-2035	10.1
	ESM2M	2026-2035	9.5
Fisheries	HiRAM	1979-2009	31.8
	CM3	2026-2035	31.2
	ESM2M	2026-2035	32.4
Oil platforms	HiRAM	1979-2009	18.4
	CM3	2026-2035	18.4
	ESM2M	2026-2035	19.0

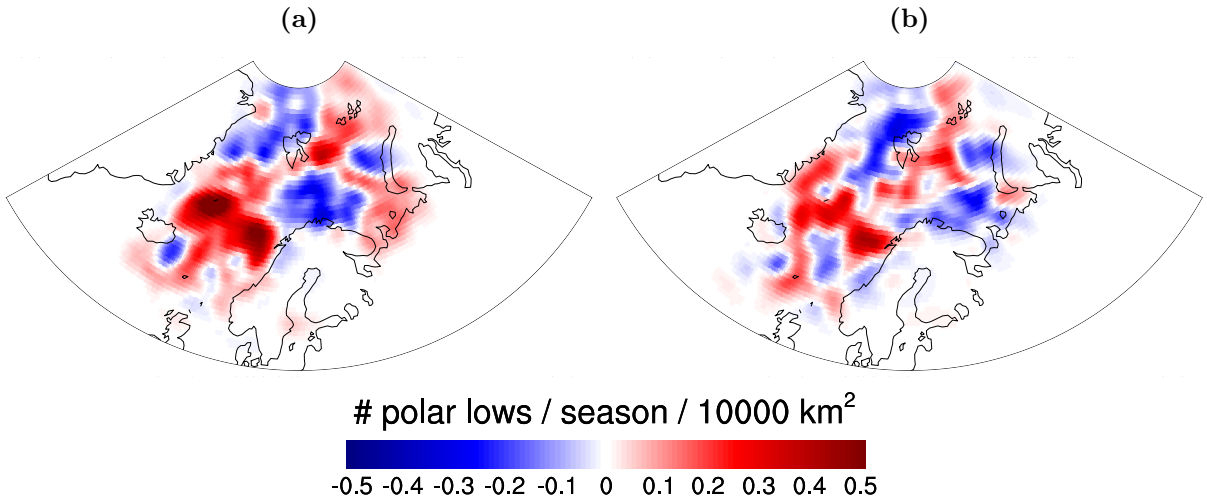

Figure 4.15: Deviation of track density from control runs for HiRAM c360 in the climate scenario RCP4.5 for the period 2026-2035 with boundary conditions provided by (a) CM3 and (b) ESM2M (shading, units: number of PLs per extended winter season per 10000 km^2). Blue colors indicate a decrease in track density and red colors indicate an increase in track density.

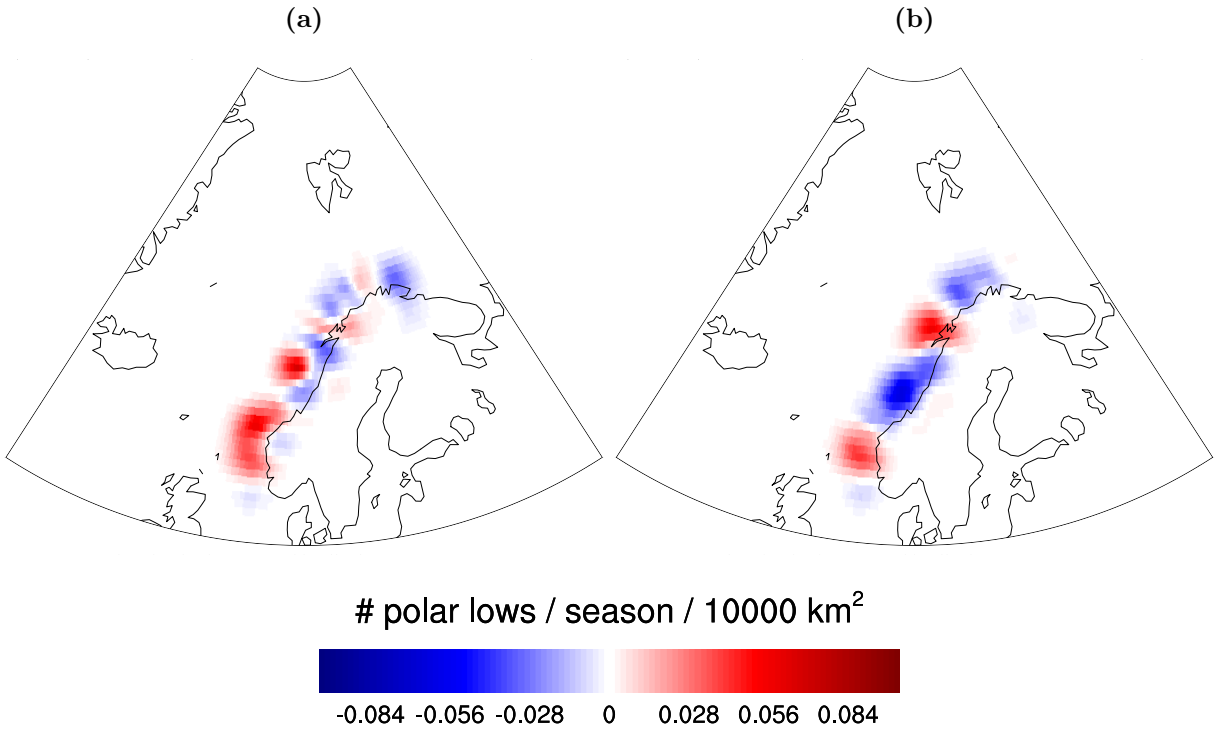

Figure 4.16: Deviation of PLs making landfall in Norway from control runs for HiRAM c360 in the climate scenario RCP4.5 for the period 2026-2035 for the boundary conditions provided by (a) CM3 and (b) ESM2M (shading, units: number of PLs per extended winter season per 10000 km^2). Blue colors indicate a decrease in track density and red colors indicate an increase in track density.

Figure 4.16 shows the deviation from the control runs for PLs making landfall in Norway, both for CM3 and ESM2M for the period 2086-2095. An increase in PLs compared to the control runs is evident at the coast of southern and middle Norway for CM3, reflecting the increase in track density east of Iceland found in Fig. 4.15a. A decrease at the coast of middle Norway is evident for ESM2M, as well as a decrease around Lofoten and a decrease further north, all reflecting the track density found in Fig. 4.15b.

Figures 4.17 and 4.18 show the density of PLs reaching fisheries and oil platforms, respectively. Figure 4.17 shows quite similar results for CM3 and ESM2M, with a decrease in PLs reaching fisheries south of Svalbard and an increase outside the coast of middle Norway, which are similar patterns as for HiRAM c180. Figure 4.18 show similar behavior as for HiRAM c180, except for an increase in PLs reaching the oil platforms outside the western coast of Norway.

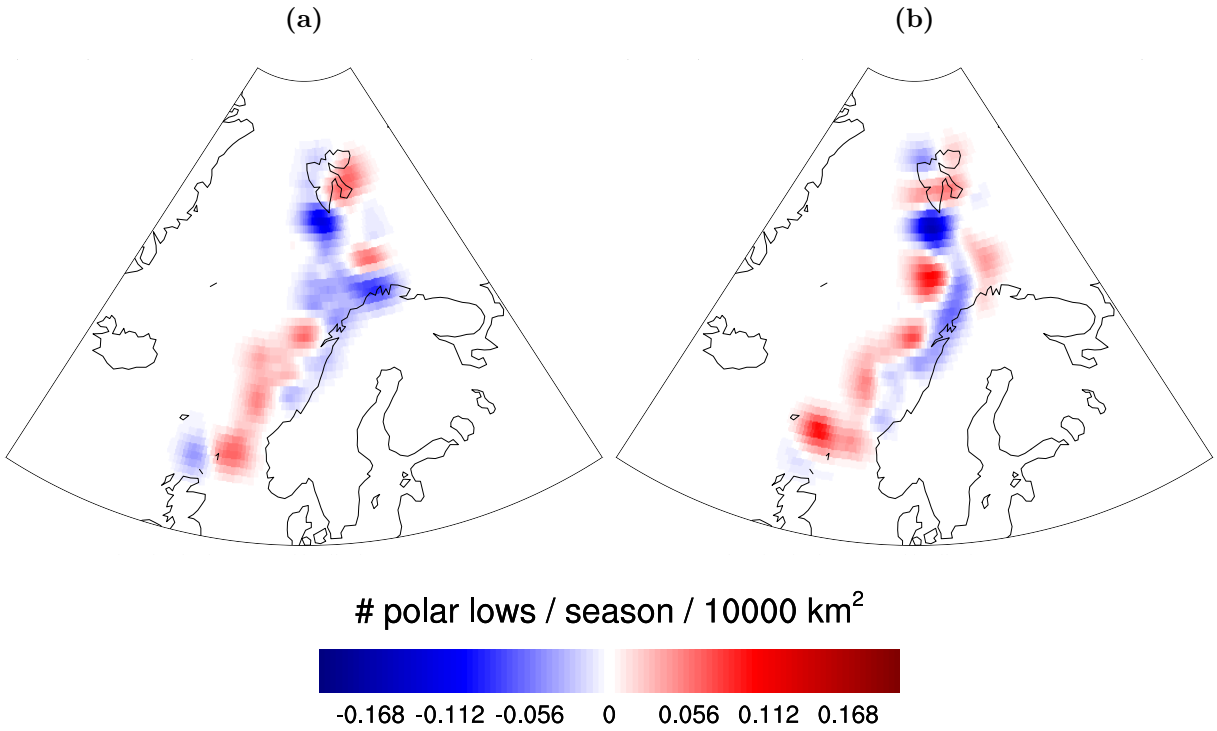

Figure 4.17: Deviation of PLs reaching fisheries from control runs for HiRAM c360 in the climate scenario RCP8.5 for the period and with boundary conditions provided by (a) 2086-2095 CM3 and (b) 2086-2095 ESM2M (shading, units: number of PLs per extended winter season per 10000 km^2). Blue colors indicate a decrease in track density and red colors indicate an increase in track density.

RCP 8.5

Table 4.5 shows the numbers of PLs for the period 2086-2095, with boundary conditions provided by CM3 and ESM2M, for the HiRAM c360 model in the RCP8.5 future climate scenario, with the control runs as a reference. It is again evident that the numbers are almost identical as for HiRAM c180 (Table 4.3).

Figure 4.19 shows the track density in the Nordic seas for the period 2086-2095 with boundary conditions provided by CM3 and ESM2M, for the HiRAM c360 model in the RCP8.5 future climate scenario, with the control runs as a reference. The track density in Fig. 4.19 shows an increase east of Iceland and east of Svalbard and a decrease for most other parts of the Nordic seas both for CM3 and ESM2M, very similar to the results for c180 (Fig. 4.11). The density of PLs making landfall in Norway, reaching fisheries and reaching oil platforms are shown in Figs. 4.20, 4.21 and 4.22, respectively, all showing a general decrease in PLs compared to the control runs, however slightly more pronounced than for HiRAM c180 (Figs. 4.12, 4.13 and 4.14).

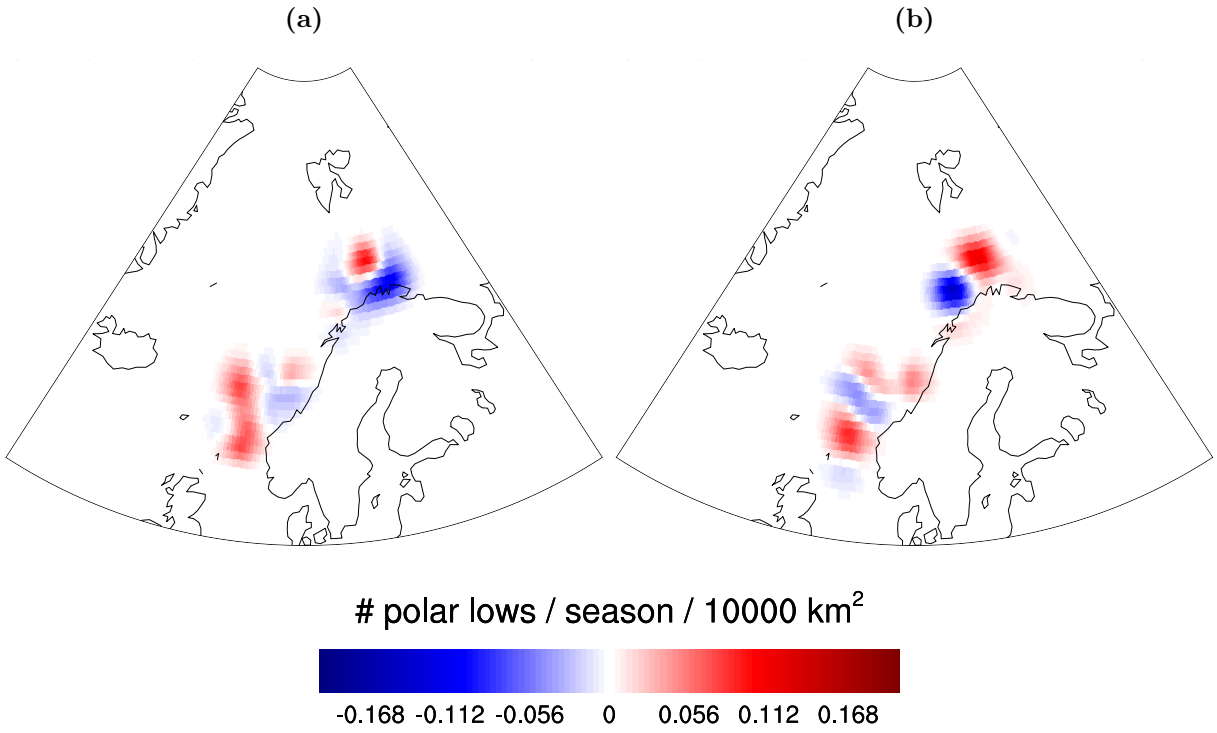

Figure 4.18: Deviation of PLs reaching oil platforms from control runs for HiRAM c360 in the climate scenario RCP8.5 for the period and boundary conditions (a) 2086-2095 CM3 and (b) 2086-2095 ESM2M (shading, units: number of PLs per extended winter season per 10000 km^2). Blue colors indicate a decrease in track density and red colors indicate an increase in track density.

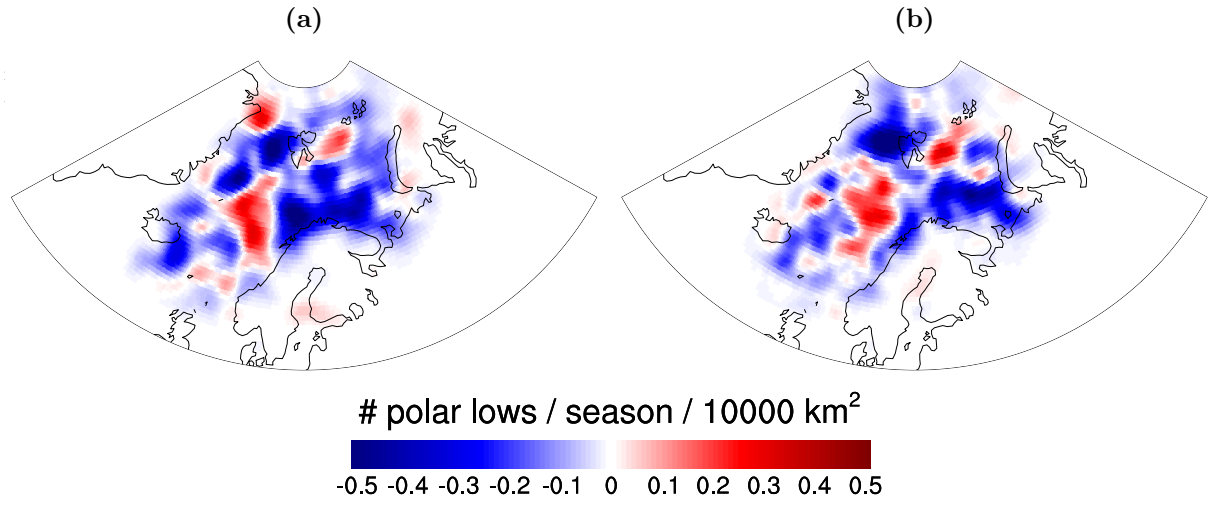

Figure 4.19: Deviation of track density from control runs for HiRAM c360 in the climate scenario RCP8.5 for the period 2086-2095 with boundary conditions provided by (a) CM3 and (b) ESM2M (shading, units: number of PLs per extended winter season per 10000 km^2). Blue colors indicate a decrease in track density and red colors indicate an increase in track density.

Table 4.5: Numbers of PLs per season making landfall in Norway, and reaching the Nordic seas, fisheries and oil platforms for the model HiRAM c360 for the period 2086-2095 for RCP8.5, with different boundary conditions.

Area	Boundary conditions	Period	Pls/season
Nordic seas	HiRAM	1979-2009	64.0
	CM3	2086-2095	50.7
	ESM2M	2086-2095	53.9
Norway	HiRAM	1979-2009	9.8
	CM3	2086-2095	8.1
	ESM2M	2086-2095	8.6
Fisheries	HiRAM	1979-2009	31.8
	CM3	2086-2095	28.1
	ESM2M	2086-2095	29.6
Oil platforms	HiRAM	1979-2009	18.4
	CM3	2086-2095	16.5
	ESM2M	2086-2095	16.9

4.2.3 Comparison to other climatologies

Zahn and von Storch (2008)

Our investigation of PLs for future climates shows a reduction of PLs in the Nordic seas, though only 20% for the most severe global warming scenario, much less than the results found by Zahn and von Storch (2008). The reason for the lower value of reduction of PLs compared to Zahn and von Storch (2008) could be explained by the fact that the the vertical stability in the form of the parameter SST-T500 was not calculated in this thesis, as was done by Zahn and von Storch (2008), leaving out an important factor for less favorable conditions for PL development.

Calculations of the average latitude of genesis for both HiRAM models were made, for both periods, with the the different boundary conditions and RCPs, to compare with the 2° northward shift in genesis density found by Zahn and von Storch (2008), with the results shown in Table 4.6 for HiRAM c180 and in Table 4.7 for HiRAM c360. It is evident from both Tables 4.6 and 4.7 that no northward shift in genesis of PLs can be found, but rather the opposite. A small southward shift of genesis is found for all simulations, with a shift of 0.5° for HiRAM c360 with boundary conditions provided by ESM2M, with

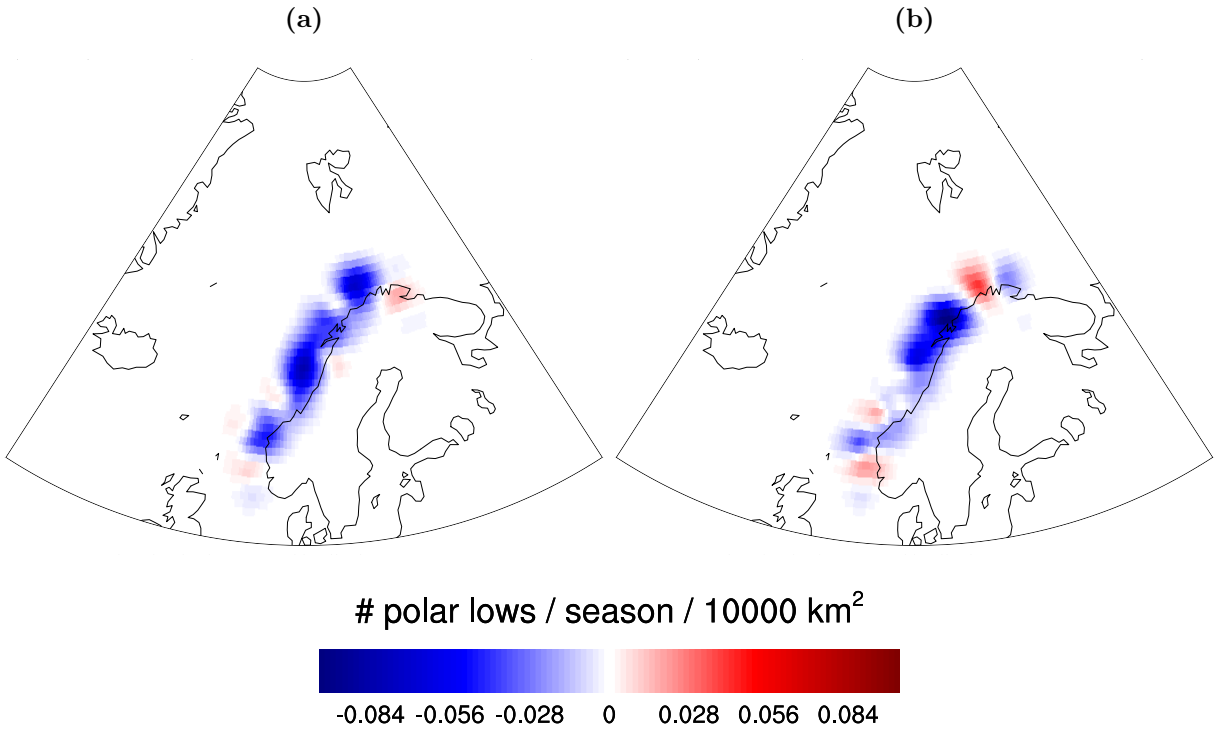

Figure 4.20: Deviation of PLs making landfall in Norway from control runs for HiRAM c360 in the climate scenario RCP8.5 for the period 2086-2095 with boundary conditions provided by (a) CM3 and (b) ESM2M (shading, units: number of PLs per extended winter season per 10000 km^2). Blue colors indicate a decrease in track density and red colors indicate an increase in track density.

Table 4.6: Average latitude of genesis for PLs in the Nordic seas for the model HiRAM c180 in the different periods, for the different RCPs, with different boundary conditions.

Boundary conditions	Period	RCP	*avg* latitude
HiRAM	1979-2009	N/A	71.06
CM3	2026-2035	4.5	70.91
	2086-2095	4.5	70.90
	2086-2095	8.5	70.65
ESM2M	2026-2035	4.5	70.94
	2086-2095	4.5	70.95
	2086-2095	8.5	70.78

RCP8.5 for the period 2086-2095 being the largest southward shift. When investigating the figures of Zahn and von Storch (2008) closely, the northward shift can be linked to the largest decrease in genesis density found around the southwestern tip of Greenland. This is outside the Nordic seas domain utilized in this thesis, and could explain the lacking northward shift.

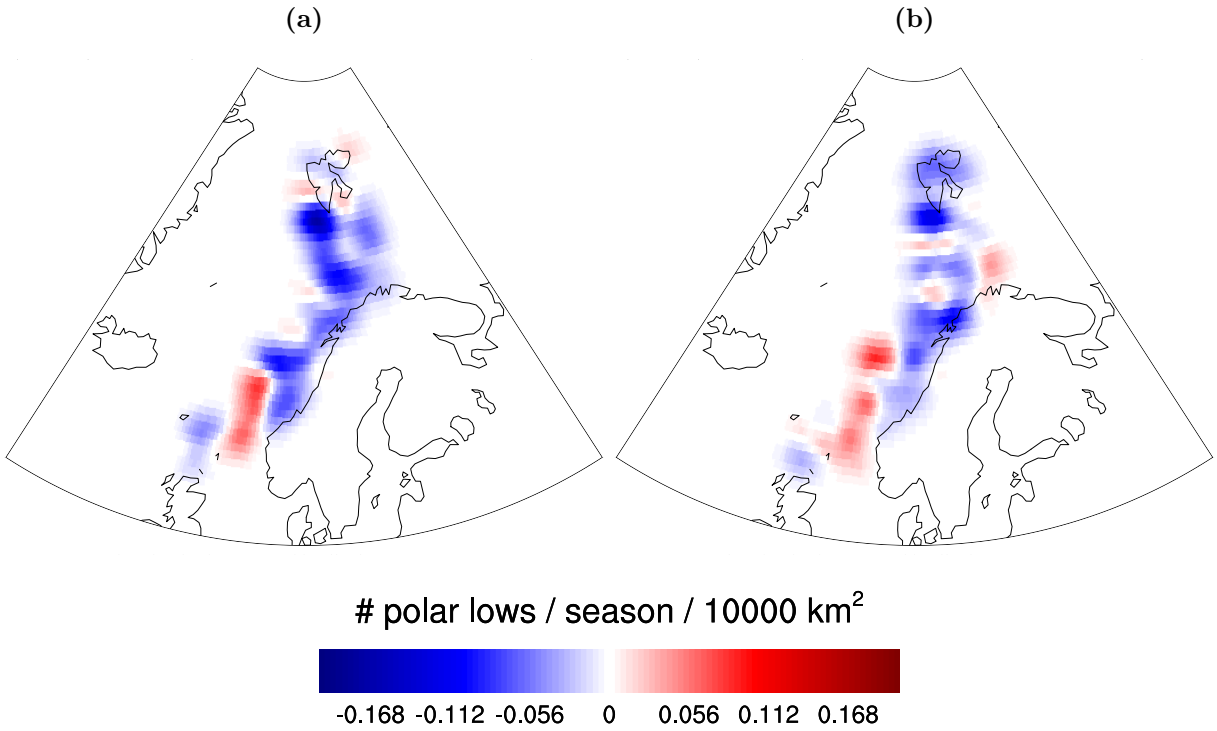

Figure 4.21: Deviation of PLs reaching fisheries from control runs for HiRAM c360 in the climate scenario RCP8.5 for the period 2086-2095 with boundary conditions provided by (a) CM3 and (b) ESM2M (shading, units: number of PLs per extended winter season per 10000 km^2). Blue colors indicate a decrease in track density and red colors indicate an increase in track density.

Table 4.7: Average latitude of genesis for PLs in the Nordic seas for the model HiRAM c360 in the different periods, for the different RCPs, with different boundary conditions.

Boundary conditions	Period	RCP	*avg* latitude
HiRAM	1979-2009	N/A	71.03
CM3	2026-2035	4.5	70.79
	2086-2095	8.5	70.86
ESM2M	2026-2035	4.5	70.82
	2086-2095	8.5	70.53

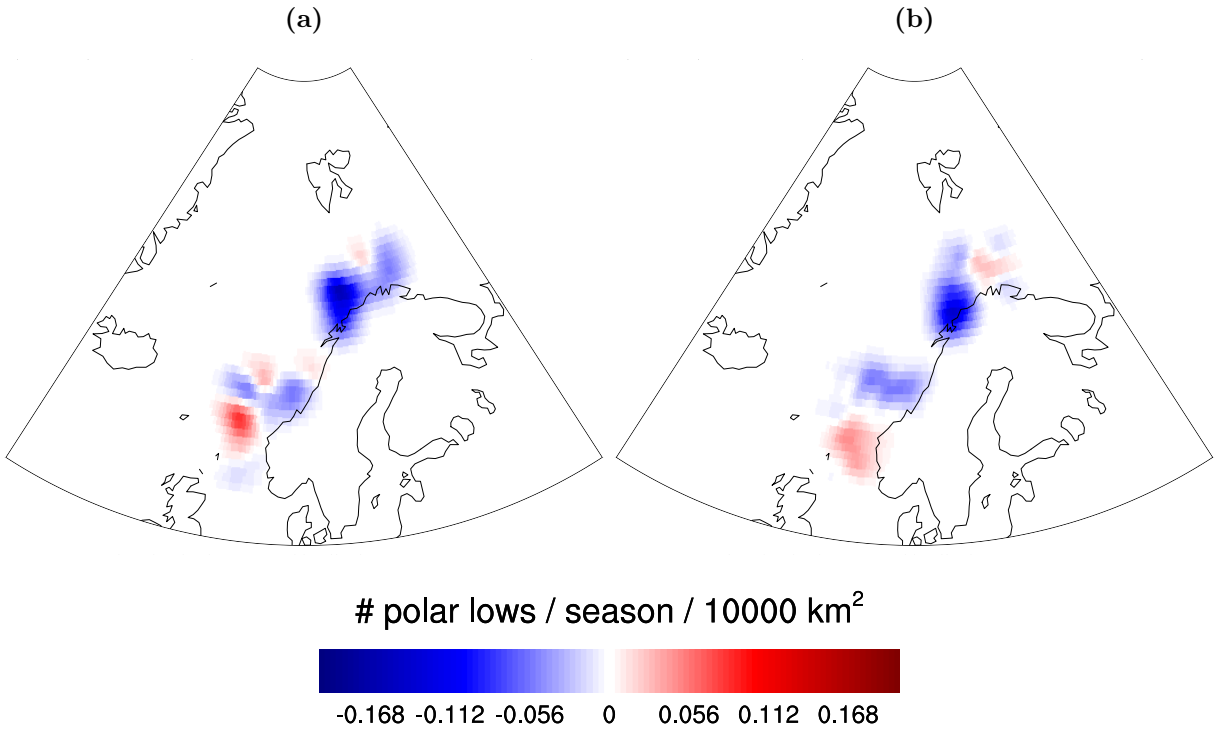

Figure 4.22: Deviation of PLs reaching oil platforms from control runs for HiRAM c360 in the climate scenario RCP8.5 for the period 2086-2095 with boundary conditions provided by (a) CM3 and (b) ESM2M (shading, units: number of PLs per extended winter season per 10000 km^2). Blue colors indicate a decrease in track density and red colors indicate an increase in track density.

Kolstad and Bracegirdle (2008)

Kolstad and Bracegirdle (2008) utilized a marine CAO (MCAO) indicator defined as the change of potential temperature with pressure:

$$\frac{\Delta\theta}{\Delta p} = \frac{\theta_{\mathrm{SKT}} - \theta_{700}}{MSLP - p_{700}} \,, \tag{4.1}$$

where θ is the potential temperature, p is pressure and SKT is the skin temperature of the sea or ice surface. The future changes in the MCAO indicator showed an increase for the areas where the sea ice had just melted, thus shifting the MCAO regions northward as the sea ice edge retreated northward throughout the 21$^{\mathrm{st}}$ century. For this reason, they concluded that also polar lows would have a northward shift, which differs from the results found in this thesis due to no CAO criteria utilized in the selection. The reason for not using a SST-T500 or a CAO criteria in this thesis is that implementing it causes less matches with the STARS database, and the goal was to find a compromise between a correct number of tracks and a high number of matches with the STARS database.

5 Summary and concluding remarks

A climatology of PLs in the Nordic seas for the period 1979-2015 was made, by applying the Melbourne detection and tracking algorithm to ERAI data. The study of the spatial distribution of the resulting PL tracks showed that the land areas most prone to landfall were the western coast of Svalbard, the coast of Norway, northwestern Russia and the island Novaya Zemlya. The most affected areas in Norway were found to be located north of Trondheim, likely linked to the CAOs in northerly flow from Svalbard. Areas designated to fishery were also found to be affected by PLs, with most PL events found south of Svalbard, implying that this could be a dangerous place for sailors to travel in the extended winter season. PLs were found to reach oil platforms, mainly those located to the north. A suggestion for future work on PLs reaching fisheries would be to use more accurate data for fishery activity, e.g. by selecting only the areas where ships and boats travel more than a certain threshold value, based on coordinates from voyage logs. Oil platforms coordinates could also be utilized, to get a better representation of oil platform areas than the map utilized in this thesis.

560 PLs were found to make landfall in Norway in the period 1979-2015, which is a very high number compared to previous climatologies on PLs in the Nordic seas. This suggests that other types of cyclones, such as secondary frontal cyclogenesis, orographic cyclogenesis, or high vorticity centres in fronts not corresponding to a cyclone, might be included in the tracks selected as PLs. A future solution to this problem could be to perform a sensitivity analysis using different input parameters in the detection and tracking algorithm, or use more restrictive conditions in the selection program.

The temporal distribution of PLs making landfall in Norway in the period 1979-2015 showed a rather large annual variability, but no declining or inclining trend. December, January, and February were the most favorable months for PLs making landfall in Norway,

as these are the months when the environment is most suitable for CAOs due to lower atmospheric temperature. No minimum in PL activity was found in February, in contrast to previous climatologies of PLs. A reason for the minimum found in previous climatologies could be due to a lack of implementing weighting of the number of days in each month, as February is the month which has the fewest days.

A sensitivity analysis was performed to understand the effect the environment has on PL distribution. FS conditions were found to be more favorable for PL development in the Nordic seas as well as for PLs making landfall in Norway, compared to RS conditions. This opposes to Terpstra et al. (2016), who found a more equal distribution of PLs developing in FS and RS conditions, again indicating that other types of cyclones than PLs are included in the selected tracks.

Of the two low-frequency atmospheric variability patterns investigated, the SB showed the largest negative correlation value with the number of PLs making landfall in Norway. The connection between SB- and PLs making landfall in Norway was also confirmed by the large fraction of PLs having genesis and making landfall during SB- conditions. The lower geopotential height centered over Scandinavia for SB- conditions induces northerly winds in the Barents and Greenland seas, creating a favorable environment for CAOs and then for PLs to form. A slightly negative correlation value is also found for the NAO and the number of PLs making landfall in Norway. This could be explained by the northerly winds also found in the Barents and Greenland seas for NAO- conditions, however weaker compared to SB- conditions.

A climatology of PLs in the Nordic seas for the future climate scenarios RCP4.5 and RCP8.5 was made, by applying the Melbourne detection and tracking algorithm to data from GFDL models HiRAM c180 and HiRAM c360. The models utilized SST and sea ice from two other models, CM3 and ESM2M, where the former boundary conditions showed warmer SST and a more northward shifted sea ice edge for the future runs. A general decrease in PL activity was found in the Nordic seas for both the 2026-2035 and 2086-2095 periods, compared to the control runs for the period 1979-2009, with a decrease of 20% as the most extreme, occurring for the RCP8.5 climate scenario. However, the decrease was much less than what was found by Zahn and von Storch (2008). Furthermore, no evident northward shift in genesis of PLs was found. This is not too surprising as no SST-T500 or

CAO indicator was utilized in the selection of polar lows, since this was found to reduce the number of matches with the STARS database. Hence, the northward shift of sea ice and larger SST did not affect the PL distribution as much as for Zahn and von Storch (2008) and Kolstad and Bracegirdle (2008).

The GFDL output from HiRAM c360 showed very similar results as the output from the lower resolution HiRAM c180 in the form of track density and number of PLs. It can be concluded that the 4 times higher resolution in HiRAM c360 compared to HiRAM c180 failed to produce better results for the purpose of this thesis. The track density patterns showed varying behavior when different climate forcing and boundary conditions were utilized, but some general similarities in track density could be distinguished. For most runs, an increase in track density east of Svalbard could be found. This can most likely be linked to the melting of sea ice in this region, shifting the CAOs further northward. Correspondingly, a pattern of reduction in track density was often found in the southern Barents Sea, being too far away from the northward shifted CAO region. The latter pattern was most prominent for RCP8.5, when the sea ice edge was positioned furthest to the north. A reduction of track density was also found in the northern part of the Greenland sea, possibly due to a northward shift of the sea ice. An area of increase in track density was found east of Iceland, explained by higher SST, thus inducing more favorable conditions for PLs to form from CAOs from Greenland. The higher track density in this area could explain the reason for less reduction of PLs making landfall in Norway, and reaching fisheries and oil platforms. It is worth to note, however, that the deviations from the control runs were not very large, suggesting no radical change in PL distribution for future climates. Future work could investigate the PL distribution for future climates by utilizing more than just one climate model, to obtain more statistically significant results.

Bibliography

T. J. Bracegirdle and S. L. Gray. An objective climatology of the dynamical forcing of polar lows in the Nordic seas. *Int. J. Climatol.*, 28:1903–1919, 2008.

C. Claud, B. Duchiron, and P. Terray. Associations between large-scale atmospheric circulation and polar low developments over the North Atlantic during winter. *J. Geophys. Res.*, 112, 2007.

D. Dee et al. The ERA-Interim reanalysis: configuration and performance of the data assimilation system. *Q.J.R. Meteorol. Soc*, 137:553–597, 2011.

J. R. Holton and G. J. Hakim. *An introduction to dynamic meteorology*. Academic press, 2012.

E. W. Kolstad. A new climatology of favourable conditions for reverse shear polar lows. *Tellus A*, 58:344–354, 2006.

E. W. Kolstad and T. J. Bracegirdle. Marine cold-air outbreaks in the future: An assessment of IPCC AR4 model results for the Northern Hemisphere. *Clim. Dynam.*, 30: 871–885, 2008.

P. Markowski and Y. Richardson. *Mesoscale Meteorology in Midlatitudes*. Wiley-Blackwell, 2010.

C. Michel. Calculation of the Scandinavian Blocking index. Internal document. 2016.

C. Michel and K. Keay. Mode of use of the Melbourne cyclone detection/tracking algorithm. Internal document. 2014.

M. Montgomery and B. Farrell. Polar low dynamics. *J. Atmos. Sci.*, 49:2484–2505, 1992.

G. Noer, Ø. Sætra, T. Lien, and Y. Gusdal. A climatological study of polar lows in the Nordic Seas. *Q.J.R. Meteorol. Soc*, 137:1762–1772, 2011.

L. Papritz, S. Pfahl, H. Sodemann, and H. Wernli. A Climatology of Cold Air Outbreaks and Their Impact on Air–Sea Heat Fluxes in the High-Latitude South Pacific. *J. Climate*, 28:342–364, 2015.

E. Rasmussen and J. Turner. *Polar Lows: Mesoscale Weather Systems in the Polar Regions*. Cambridge University Press, 2003.

H. Rivals, J.-P. Cammas, and I. Renfrew. Secondary cyclogenesis: The initiation phase of a frontal wave observed over the eastern Atlantic. *Q.J.R. Meteorol. Soc*, 124:243–267, 1998.

I. Simmonds and R. Murray. A numerical scheme for tracking cyclone centres from digital data, part 1. *Aust. Meteorol. Mag.*, 39:155–166, 1991.

A. Terpstra, C. Michel, and T. Spengler. Forward and reverse shear environments during polar low genesis over the North East Atlantic. *Mon. Wea. Rev.*, 144:1341–1354, 2016.

S. Tibaldi and F. Molteni. On the operational predictability of blocking. *Tellus A*, 42: 343–365, 1990.

G. Walker and E. Bliss. World Weather V. *Mem. Roy. Met. Soc.*, 4, 1932.

J. Wallace and P. Hobbs. *Atmospheric Science: An Introductory Survey*. Elsevier Academic Press, 2006.

T. T. Warner. *Numerical Weather and Climate Prediction*. Cambridge University Press, 2011.

K. Wilhelmsen. Climatological study of gale-producing polar lows near Norway. *Tellus A*, 37:451–459, 1985.

W. Yanase and H. Niino. Dependence of Polar Low Development on Baroclinicity and Physical Processes: An Idealized High-Resolution Numerical Experiment. *J. Atmos. Sci.*, 64:3044–3067, 2007.

M. Zahn and H. von Storch. A long-term climatology of North Atlantic polar lows. *Geophys. Res. Lett.*, 35, 2008.